

Nanoceramics: Synthesis, Characterization, and Applications

Guest Editors: Amirkianoosh Kiani, Mohsen Rahmani, Sivakumar Manickam, and Bo Tan





Nanoceramics: Synthesis, Characterization, and Applications

Journal of Nanomaterials

Nanoceramics: Synthesis, Characterization, and Applications

Guest Editors: Amirkianoosh Kiani, Mohsen Rahmani,
Sivakumar Manickam, and Bo Tan



Copyright © 2014 Hindawi Publishing Corporation. All rights reserved.

This is a special issue published in "Journal of Nanomaterials." All articles are open access articles distributed under the Creative Commons Attribution License, which permits unrestricted use, distribution, and reproduction in any medium, provided the original work is properly cited.

Editorial Board

Katerina E. Aifantis, USA
Nageh K. Allam, USA
Margarida Amaral, Portugal
Xuedong Bai, China
Lavinia Balan, France
Enrico Bergamaschi, Italy
Theodorian Borca-Tasciuc, USA
C. Jeffrey Brinker, USA
Christian Brosseau, France
Xuebo Cao, China
Bhanu P. S. Chauhan, USA
Shafiq Chowdhury, USA
Kwang-Leong Choy, UK
Cui ChunXiang, China
Miguel A. Correa-Duarte, Spain
Shadi A. Dayeh, USA
Ali Eftekhari, USA
Claude Estourns, France
Alan Fuchs, USA
Lian Gao, China
Russell E. Gorga, USA
Hongchen Chen Gu, China
Mustafa O. Guler, Turkey
John Z. Guo, USA
Smrati Gupta, Germany
Michael Harris, USA
Zhongkui Hong, China
Michael Z. Hu, USA
David Hui, USA
Y.-K. Jeong, Republic of Korea
Sheng-Rui Jian, Taiwan
Wanqin Jin, China
Rakesh K. Joshi, UK
Zhenhui Kang, China
Fathallah Karimzadeh, Iran
Antonios Kelarakis, UK

Alireza Khataee, Iran
Do Kyung Kim, Korea
Alan K. T. Lau, Hong Kong
Burtrand Lee, USA
Jun Li, Singapore
Benxia Li, China
Xing-Jie Liang, China
Shijun Liao, China
Gong-Ru Lin, Taiwan
Tianxi Liu, China
Jun Liu, USA
Songwei Lu, USA
Daniel Lu, China
Jue Lu, USA
Ed Ma, USA
Gaurav Mago, USA
Santanu K. Maiti, India
Sanjay R. Mathur, Germany
V. Mittal, United Arab Emirates
Weihai Ni, China
Sherine Obare, USA
Atsuto Okamoto, Japan
Abdelwahab Omri, Canada
Edward A. Payzant, USA
Kui-Qing Peng, China
Anukorn Phuruangrat, Thailand
Mahendra Rai, India
Suprakas Sinha Ray, South Africa
Ugur Serincan, Turkey
Huaiyu Shao, Japan
Donglu Shi, USA
Vladimir Sivakov, Germany
Marinella Striccoli, Italy
Bohua Sun, South Africa
Saikat Talapatra, USA
Nairong Tao, China

Titipun Thongtem, Thailand
Somchai Thongtem, Thailand
Alexander Tolmachev, Ukraine
Valeri P. Tolstoy, Russia
Tsung-Yen Tsai, Taiwan
Takuya Tsuzuki, Australia
Raquel Verdejo, Spain
Mat U. Wahit, Malaysia
Zhenbo Wang, China
Ruiping Wang, Canada
Shiren Wang, USA
Cheng Wang, China
Yong Wang, USA
Jinquan Wei, China
Ching-Ping Wong, Hong Kong
Xingcai Wu, China
Guodong Xia, Hong Kong
Ping Xiao, UK
Zhi Li Xiao, USA
Yangchuan Xing, USA
Shuangxi Xing, China
Nanping Xu, China
Doron Yadlovker, Israel
Yingkui Yang, China
Khaled Youssef, USA
Kui Yu, Canada
William W. Yu, USA
Haibo Zeng, China
Tianyou Zhai, China
Bin Zhang, China
Renyun Zhang, Sweden
Yanbao Zhao, China
Lianxi Zheng, Singapore
Chunyi Zhi, Hong Kong

Contents

Nanoceramics: Synthesis, Characterization, and Applications, Amirkianoosh Kiani, Mohsen Rahmani, Sivakumar Manickam, and Bo Tan
Volume 2014, Article ID 528348, 2 pages

Anodic Fabrication of Ti-Nb-Zr-O Nanotube Arrays, Qiang Liu, Dongyan Ding, and Congqin Ning
Volume 2014, Article ID 240346, 7 pages

Tuning Optical Nonlinearity of Laser-Ablation-Synthesized Silicon Nanoparticles via Doping Concentration, Lianwei Chen, Xiao-fang Jiang, Ziming Guo, Hai Zhu, Tsung-Sheng Kao, Qing-hua Xu, Ghim Wei Ho, and Minghui Hong
Volume 2014, Article ID 652829, 7 pages

Behavior of Yb³⁺ and Er³⁺ during Heat Treatment in Oxyfluoride Glass Ceramics, M. H. Imanieh, I. R. Martín, J. Gonzalez-Platas, B. Eftekhari Yekta, V. K. Marghussian, and S. Shakhesi
Volume 2014, Article ID 171045, 10 pages

Effect of Ag-Nanoparticles Doped in Polyvinyl Alcohol on the Structural and Optical Properties of PVA Films, Mahshad Ghanipour and Davoud Dorrnian
Volume 2013, Article ID 897043, 10 pages

Preparation and Oxygen Permeability of BaCo_{0.7}Fe_{0.2}Nb_{0.1}O_{3-δ} Membrane Modified by Ce_{0.8}Y_{0.2}O_{2-δ} Porous Layer on the Air Side, Yuan Qiang, Zhen Qiang, and Li Rong
Volume 2013, Article ID 157474, 6 pages

Editorial

Nanoceramics: Synthesis, Characterization, and Applications

Amirkianoosh Kiani,¹ Mohsen Rahmani,² Sivakumar Manickam,³ and Bo Tan⁴

¹ Department of Mechanical Engineering, University of New Brunswick (UNB), Canada

² Department of Physics (EXSS), Imperial College London, 901 Blackett Lab, Prince Consort Road, London, UK

³ Department of Sciences, Amrita School of Engineering, Amrita Vishwa Vidyapeetham, Amritanagar (PO), Coimbatore, Tamil Nadu, India

⁴ Department of Aerospace Engineering, Ryerson University, Canada

Correspondence should be addressed to Bo Tan; tanbo@ryerson.ca

Received 11 June 2014; Accepted 11 June 2014; Published 26 June 2014

Copyright © 2014 Amirkianoosh Kiani et al. This is an open access article distributed under the Creative Commons Attribution License, which permits unrestricted use, distribution, and reproduction in any medium, provided the original work is properly cited.

Over the past decade, nanoceramics have received significant attention as candidate materials due to their capability to demonstrate improved and unique properties in comparison with conventional bulk ceramic materials. Nanoceramics exhibit unique processing, mechanical, and surface characteristics such as superplasticity, machinability, strength, toughness, and bioactivity due to the fine grain size, abundant grain boundaries, and controllable crystallinity.

This issue compiles five exciting manuscripts, which address recent trends and development in nanoceramics.

The optical properties of nanoceramics are addressed in three manuscripts. Optical nonlinear performance of silicon nanoparticles at different doping concentrations has been investigated by L. Chen et al. Their results show silicon nanoparticles generated by femtosecond laser ablation exhibit better saturable absorption performance at higher doping concentrations. Their results reveal the possibility to tune the optical nonlinearity of silicon nanoparticles by changing the doping concentration.

In recent times, there are great interests in luminescent materials for efficient frequency conversion from infrared to visible radiation; oxyfluoride glass ceramics are ambivalent materials which can exhibit optical properties of fluoride single-crystals when they are doped with rare-earth ions. M. H. Imanieh et al.'s manuscript focuses on improvement of Er^{3+} emissions in two series of oxyfluoride glass ceramics ($\text{SiO}_2/\text{Al}_2\text{O}_3$ and $\text{SiO}_2/\text{Al}_2\text{O}$) containing CaF_2 nanocrystals doped with a fixed amount of Er^{3+} and Yb^{3+} through the

heat treatment at different temperatures. They showed in their study that increasing the temperature of the heat treatment leads to a rise in the red and green emissions in the upconversion luminescence of the treated samples. Also, increasing the heat treatment temperature leads to the incorporation of Er^{3+} ions into CaF_2 crystals and can increase the Yb^{3+} concentration. Increased Yb^{3+} concentration improves the energy transfer and back transfer process between Er^{3+} and Yb^{3+} ions and as a result upconversion intensity can be increased.

Polymers have attracted a lot of attention as excellent host materials for encapsulation of metal nanoparticles like silver, gold, copper, and so forth. Many reports in the literature show attempts for synthesis of metal-polymer nanocomposites based on polymers, with the possibility of variation in their optical, mechanical, and electrical properties for the application in photovoltaic and biomedical devices fabrication. M. Ghanipour et al. investigated the effect of silver nanoparticles doped in PVA on the structural and optical properties of composite films. Their results show that by embedding silver nanoparticles inside the polymer, a number of Bragg's planes in the structure of polymer and its crystallinity are increased noticeably. Ag-O bonds are formed in the films and the bandgap energy, refractive index, and dielectric constant of samples are decreased by increasing the concentrations of silver nanoparticles.

Two of the manuscripts deal with fabrication methods for high performance nanoceramics and nanomaterials; Q. Liu et

al. reported the new method for fabrication of highly ordered Ti-Nb-Zr-O nanotube arrays through pulse anodic oxidation of Ti-Nb-Zr alloy in monosodium phosphate containing 0.5 wt% HF electrolytes. The effect of anodization parameters and Zr content on the microstructure and composition of Ti-Nb-Zr-O nanotubes have been studied using experimental analysis and it has been found that length of the Ti-Nb-Zr-O nanotubes increased with increase of Zr contents.

Y. Qiang et al. investigated the materials and chemical properties of BCFN dense ceramic membrane with submicron-CYDC porous layer by the partial oxidation of coke oven gas (COG) in hydrogen production. The results of their study show that this structure exhibits higher stability and no chemical reaction at high temperature environment. Also, the influences of YDC modification on the surface kinetics and oxygen permeation rates of BCFN membranes have been analyzed.

By compiling these papers, we hope to enrich our readers and researchers with respect to synthesis, characterization, and applications of nanoceramics.

Acknowledgments

Finally, we would like to express our gratitude to the many reviewers for their hard works. We would also like to thank the authors for their contributions to the special issue. This special issue could not have been completed without their dedication and support.

Amirkianoosh Kiani
Mohsen Rahmani
Sivakumar Manickam
Bo Tan

Research Article

Anodic Fabrication of Ti-Nb-Zr-O Nanotube Arrays

Qiang Liu,¹ Dongyan Ding,¹ and Congqin Ning²

¹ Institute of Microelectronic Materials and Technology, School of Materials Science and Engineering, Shanghai Jiao Tong University, Shanghai 200240, China

² State Key Laboratory of High Performance Ceramics and Superfine Microstructure, Shanghai Institute of Ceramics, Chinese Academy of Sciences, Shanghai 200050, China

Correspondence should be addressed to Dongyan Ding; dying@sjtu.edu.cn

Received 14 December 2013; Revised 1 March 2014; Accepted 1 March 2014; Published 27 March 2014

Academic Editor: Amirianoosh Kiani

Copyright © 2014 Qiang Liu et al. This is an open access article distributed under the Creative Commons Attribution License, which permits unrestricted use, distribution, and reproduction in any medium, provided the original work is properly cited.

Highly ordered Ti-Nb-Zr-O nanotube arrays were fabricated through pulse anodic oxidation of Ti-Nb-Zr alloy in 1 M NaH₂PO₄ containing 0.5 wt% HF electrolytes. The effect of anodization parameters and Zr content on the microstructure and composition of Ti-Nb-Zr-O nanotubes was investigated using a scanning electron microscope equipped with energy dispersive X-ray analysis. It was found that length of the Ti-Nb-Zr-O nanotubes increased with increase of Zr contents. The diameter and the length of Ti-Nb-Zr-O nanotubes could be controlled by pulse voltage. XRD analysis of Ti-Nb-Zr-O samples annealed at 500°C in air indicated that the (101) diffraction peaks shifted from 25.78° to 25.05° for annealed Ti-Nb-Zr-O samples with different Zr contents because of larger lattice parameter of Ti-Nb-Zr-O compared to that of undoped TiO₂.

1. Introduction

Nanostructures of different metals or semiconductors have received much attention due to the wide application of these materials in photocatalysts, solar energy conversion, gas sensing, and biomedical applications [1–4]. TiO₂ nanotubes have been widely investigated due to their excellent biomedical application and photocatalytic effect since 1972 [5]. However, TiO₂ can be only excited by UV light which only occupies 5% of the solar spectrum because of its wide band gap (3.2 eV). Therefore, many approaches were used to extend the spectral response of the titanium dioxide to the visible light region and impurity doping is one of the typical and effective approaches. Many metal elements (Fe, Mo, Cr, Nb, etc.) and nonmetal elements (B, C, N, S, and F) have been used to dope TiO₂ to broaden its application fields [6–8]. Zr and Nb doping could affect the optical absorption ability of TiO₂ oxide. Hirano et al. reported that the onset of absorption of TiO₂ shifted to longer wavelengths by Zr and Nb doping [9, 10].

One-dimensional nanostructures have advantages over films and powder because the former can provide large surface-to-volume ratio and unidirectional electrical channel. Several research groups have reported the anodic

formation of oxide nanostructures on the surfaces of titanium alloys to achieve good photocatalysts, solar energy conversion, gas sensing, and biomedical applications. Numerous methods have been reported for fabricating TiO₂ nanotubes including template-assisted process [11], hydrothermal reaction [12], seed growth [13], and anodization methods [14].

Anodic oxidation technique is relatively a simple method to fabricate one-dimensional nanotubes in comparison with other methods. Allam et al. reported the fabrication of Ti-Pd mixed oxynitride nanotube arrays through anodization of Ti-Pd alloy [15]. Berger et al. reported on the fabrication of Ti-Al-O nanotubes through anodization of Ti-Al alloys [16]. Nb- and Zr-doped TiO₂ nanotubes were also investigated recently. Liu et al. fabricated Ti-Nb-O nanotubes on Ti₃₅Nb alloy and found that Nb-doped TiO₂ nanostructures had excellent hydrogen sensing capability [17]. Allam et al. fabricated Ti-Nb-Zr-O nanotubes through anodization of Ti₃₅Nb₅Zr alloy for enhanced hydrogen generation by water photoelectrolysis [18]. Li et al. found that the Nb- and Zr-doped TiO₂ nanostructures showed good biological properties [19].

To date, rare work has been reported on the effect of Zr content on the formation of Ti-Nb-Zr-O nanotubes. In

the present work, we fabricated highly ordered Ti-Nb-Zr-O nanotube arrays on Ti-Nb-Zr alloy substrate with different Zr contents by pulse anodic oxidation. The effect of Zr content and anodization parameters on the microstructures of Ti-Nb-Zr-O oxides was investigated.

2. Experiment Section

2.1. Synthesis of Ti-Nb-Zr-O Nanotubes. Prior to anodization, all of the Ti-Nb-Zr alloy samples (Ti35Nb5Zr, Ti35Nb10Zr, Ti35Nb15Zr) were ground and polished with number 2000 SiC emery papers and then ultrasonically cleaned with absolute alcohol. Finally, they were rinsed with deionized water and dried in N₂ stream. Electrochemical anodization was carried out with a pulse voltage stabilizer. Anodic samples were fabricated with pulse voltages of 20 V, 30 V, and 40 V with a constant frequency of 4000 Hz and duty cycle of 20% for 90 minutes in electrolytes of 1M NaH₂PO₄ containing 0.5 wt% HF. The pulse frequency varied from 2000 Hz to 4000 Hz. The effects of anodization voltage and pulse frequency on the microstructures and composition of Ti-Nb-Zr-O samples with different Zr contents were investigated.

2.2. Microstructural Characterization. The structure morphology and composition of Ti-Nb-Zr-O samples were investigated using a scanning electron microscope (SEM; FEI SIRION 200, USA) equipped with energy dispersive X-ray analysis (EDXA; OXFORD INCA, USA). The as-anodized Ti-Nb-Zr-O samples grown on different Ti-Nb-Zr alloy substrates were annealed at 500°C in air. Phase structures of the as-annealed Ti-Nb-Zr-O samples were characterized with X-ray diffraction (XRD, D/max 2550 V). For reference, undoped TiO₂ nanotubes were also fabricated through anodization of pure Ti substrate.

3. Results and Discussion

Figure 1 shows top and cross-section views of Ti-Nb-Zr-O nanotubes grown on Ti35Nb5Zr alloy substrate at different voltages. The oxide sample prepared at 20 V showed a web-like structure rather than a nanotubular array morphology. When the anodization voltage increased to 30 V, the nanotube arrays could form. The average diameter and length of the nanotubes were 170 nm and 4.75 μm, respectively. When the anodization voltage increased to 40 V, the average diameter and length of the nanotubes were 220 nm and 4.8 μm, respectively. The slight increase in length from about 4.75 μm to 4.8 μm was attributed to a competition between an electrochemical oxide formation and chemical dissolution of oxide by fluoride ions. The formation rate of the nanotube bottom and the dissolution rate of the nanotube top at an anodization voltage of 30 V were almost equivalent. Therefore, the length of the nanotubes almost remained unchanged when the anodization voltage increased to 40 V.

Figure 2 shows top and cross-section views of Ti-Nb-Zr-O nanotubes grown on Ti35Nb10Zr alloy substrate at different voltages. When the anodization voltage was 20 V, the as-grown Ti-Nb-Zr-O nanotube arrays had a clear nanotubular

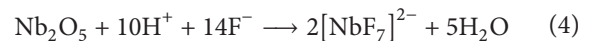
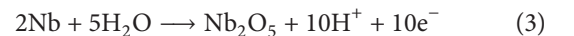
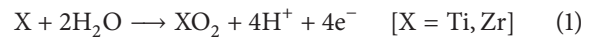
TABLE 1: Summary of average length and diameter of the nanotubes grown at different anodization voltages.

Samples	Anodization voltage	Average length (μm)	Average diameter (nm)
Ti35Nb5Zr	20 V	—	—
	30 V	4.75	170
	40 V	4.80	220
Ti35Nb10Zr	20 V	2.26	98
	30 V	5.23	150
	40 V	6.12	206
Ti35Nb15Zr	20 V	3.25	103
	30 V	5.84	153
	40 V	8.13	210

morphology. When the anodization voltage increased to 30 V, the average diameter and length were 150 nm and 5.25 μm, respectively. At 40 V, Ti-Nb-Zr-O nanotube arrays grown on the Ti35Nb10Zr alloy substrate had an average diameter of 206 nm and average length of 6.12 μm. The diameter was slightly smaller than that of the nanotubes grown on Ti35Nb5Zr alloy substrate.

Figure 3 shows top and cross-section views of Ti-Nb-Zr-O nanotubes grown on Ti35Nb15Zr alloy substrate at different voltages. The average length of the Ti-Nb-Zr-O nanotubes was 8.13 μm when the anodic voltage was 40 V. Summary of the nanotube length and diameter of the three kinds of nanotubes is shown in Table 1.

During the anodization process, many factors such as oxidation electrolyte, anodization voltage, and time could affect the formation of Ti-Nb-Zr-O nanotubes. There is a competition between the electrochemical oxide formation and chemical dissolution of oxide by fluoride ions. The nanotube growth could reach a steady state in which the formation rate at the bottom and dissolution rate at the top are equal [20]. The growth of Ti-Nb-Zr-O nanotubes remarkably depended on local electric field and solution diffusion rate and took place preferentially at some locations on the Ti-Nb-Zr alloy substrate. The anodic formation mechanism of the Ti-Nb-Zr-O nanotubes can be represented as follows [21, 22]:



At first, oxidized metal species react with O²⁻ ions (from H₂O) to form an oxide layer growth on the metal surface. In contrast, due to the presence of F⁻ ions, dissolution and breakdown of oxide layer occur along random path through this layer and form disordered wormlike structure. The oxide layer will be finally removed by chemical dissolution and water-soluble [XF₆]²⁻ or [NbF₇]²⁻ formed, making the underneath highly ordered tube structure observable from

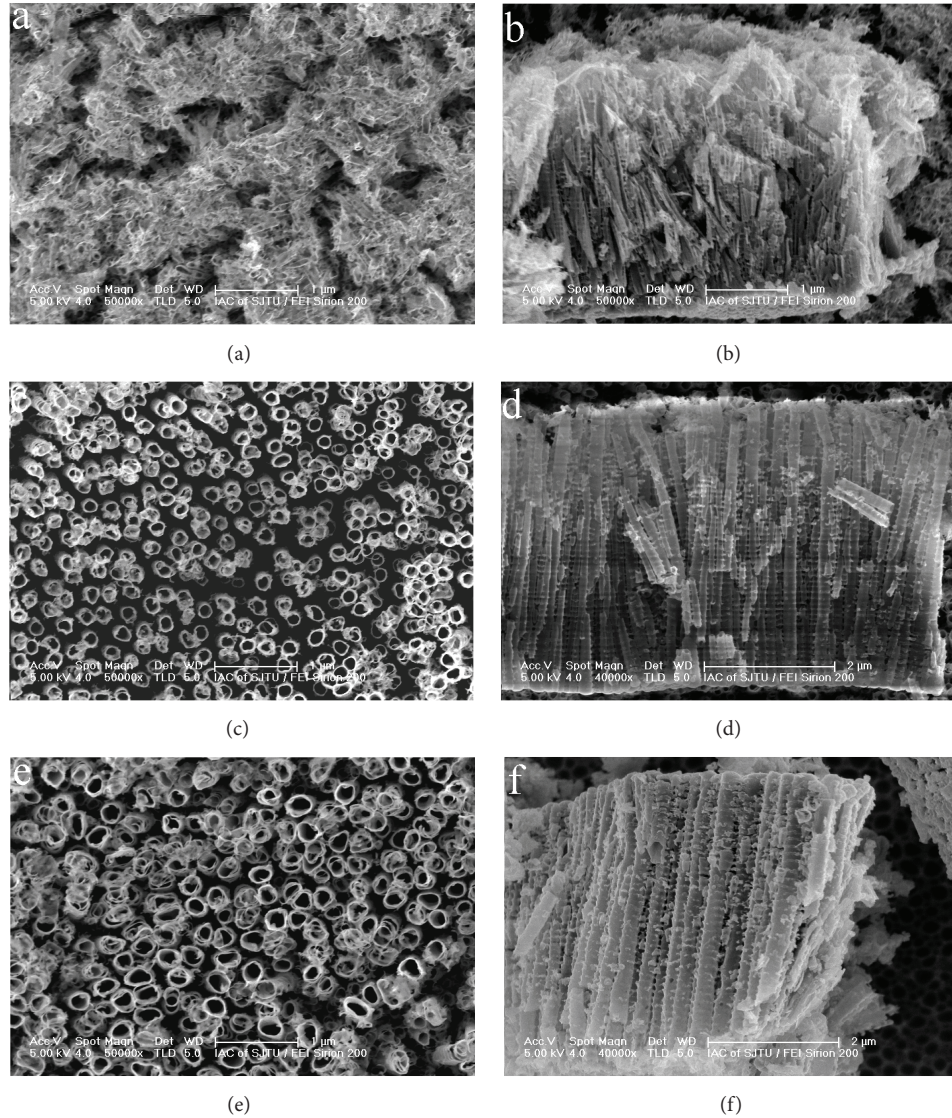


FIGURE 1: Top and cross-section views of Ti-Nb-Zr-O nanotubes grown on Ti35Nb5Zr alloy substrate at different voltages with a constant frequency of 4000 Hz and duty cycle of 20% for 90 minutes, (a)-(b) 20 V, (c)-(d) 30 V, and (e)-(f) 40 V.

TABLE 2: EDS analysis of the Ti-Nb-Zr-O nanotubes grown on different Ti-Nb-Zr alloy substrates at 40 V with a constant frequency of 4000 Hz and duty cycle of 20% for 90 minutes.

Samples	Ti (wt%)/(at%)	O (wt%)/(at%)	Nb (wt%)/(at%)	Zr (wt%)/(at%)
Ti35Nb5Zr	28.94/16.05	46.27/76.84	21.54/6.16	3.25/0.95
Ti35Nb10Zr	28.25/16.13	44.30/75.75	21.00/6.19	6.45/1.94
Ti35Nb15Zr	26.25/15.58	42.92/74.66	21.89/6.70	9.85/3.07

the top. Meanwhile, oxidized metal species could react with O^{2-} ions to form a new oxide layer. When the formation rate of the nanotube bottom and the dissolution rate of the nanotube top are equivalent, the length of nanotube remains unchanged. For the Ti-Nb-Zr alloy an increase in anodization voltage could increase the nanotube length since the driving force for ionic transport through the barrier layer at the pore bottom could be enhanced, which will result in faster

migration of cations and/or anions and thus movement of the Ti-Nb-Zr/Ti-Nb-Zr-O interface into the Ti-Nb-Zr alloy.

Our experimental results revealed that Zr content in the Ti-Nb-Zr alloy played an important role in formation of Ti-Nb-Zr-O nanotubes because of different electrochemical properties of Ti and Zr elements. The solubility of the fluoride complex for $[ZrF_6]^{2-}$ is larger than that for $[TiF_6]^{2-}$. This could result in a larger anodic current for the Ti-Nb-Zr alloy

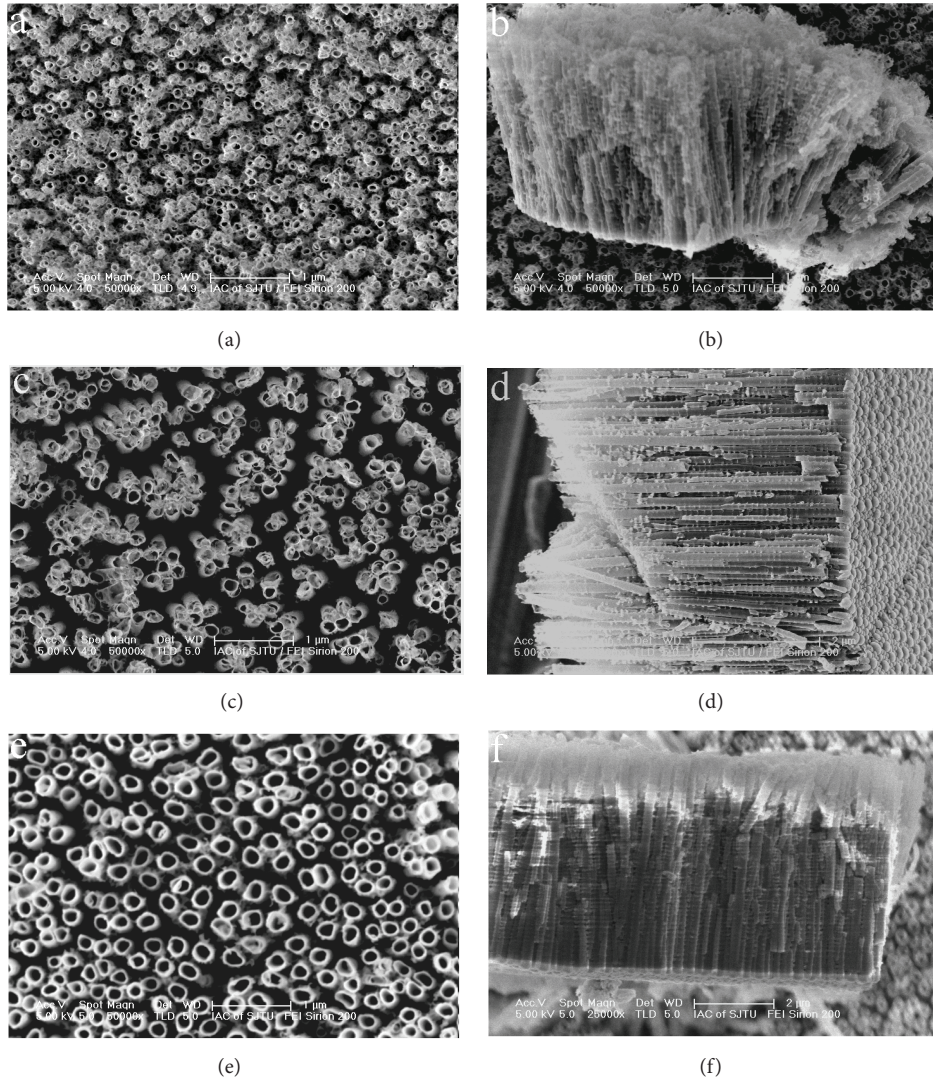


FIGURE 2: Top and cross-section views of Ti-Nb-Zr-O nanotubes grown on Ti35Nb10Zr alloy substrate at different voltages with a constant frequency of 4000 Hz and duty cycle of 20% for 90 minutes, (a)-(b) 20 V, (c)-(d) 30 V, and (e)-(f) 40 V.

with higher Zr content than that with lower Zr content at the same potential [21, 23]. The dissolution rate of the as-formed oxide layers by fluoride ion should be another factor in determining the length of the Ti-Nb-Zr-O nanotubes [24]. As shown above, the formation of Ti-Nb-Zr-O nanotubes with a high Zr content was easier than that with a low Zr content.

EDS analyses of the as-anodized Ti-Nb-Zr-O samples with different Zr contents were carried out to investigate the composition of the Ti-Nb-Zr-O samples. As shown in Table 2, each sample was mainly composed of Ti, Nb, Zr, and O elements. With the increase of Zr content of original alloys, contents of the Ti and Zr elements in the Ti-Nb-Zr-O oxide layer also changed correspondingly. The contents of Nb and Zr elements in the Ti-Nb-Zr-O samples were smaller than those of the original alloys. This phenomenon may be explained by considering the difference in the dissolution rate for different oxide systems since previous reports have

shown that the nanotube formation on different pure metals had different chemical dissolution rates in the dilute HF electrolytes [25].

The effect of pulse frequency on the formation of Ti-Nb-Zr-O nanotubes was also investigated. Figure 4 shows SEM images of the Ti-Nb-Zr-O samples fabricated at 40 V with a constant frequency of 2000 Hz and duty cycle of 20% for 90 minutes on different Ti-Nb-Zr alloy substrates. As shown in Figure 4(a), the top surface of the oxide layer had a lot of irregular nanoporous structures and high aligned nanotube arrays did not form due to a low electrical field. However, the nanotube structure grown on Ti35Nb10Zr alloy substrate became denser and more vertically oriented at the same condition. Furthermore, the nanotubes grown on Ti35Nb15Zr alloy substrate presented a much more regular, well-aligned nanotube array architecture. This proved that the Ti35Nb15Zr system was easier for nanotube growth than the Ti35Nb5Zr system did.

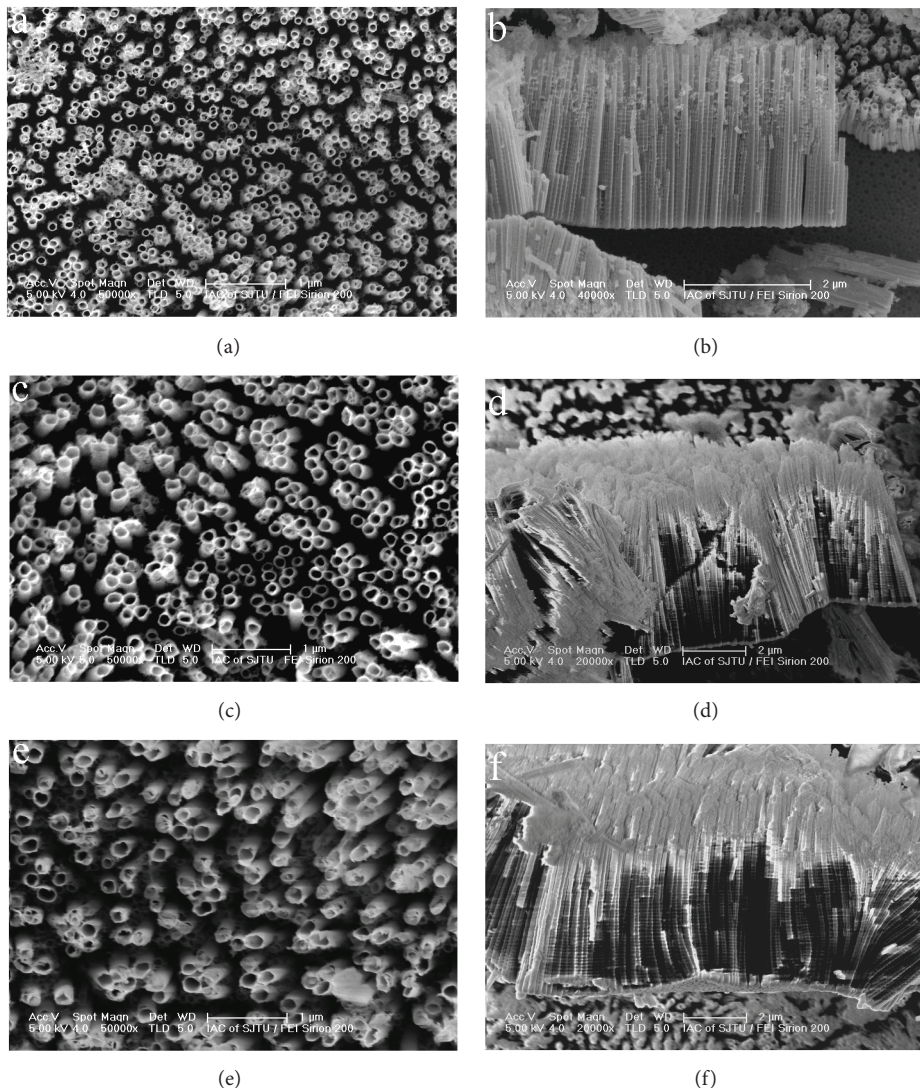


FIGURE 3: Top and cross-section views of Ti-Nb-Zr-O nanotubes grown on Ti35Nb15Zr alloy substrate at different voltages with a constant frequency of 4000 Hz and duty cycle of 20% for 90 minutes, (a)-(b) 20 V, (c)-(d) 30 V, and (e)-(f) 40 V.

XRD analyses were conducted to characterize the crystal structure of the as-annealed Ti-Nb-Zr-O oxides with different Zr contents. As shown in Figure 5, diffraction peaks corresponding to the anatase TiO_2 phase in the as-annealed Ti-Nb-Zr-O samples could be found. The (101) diffraction peak of undoped TiO_2 appeared at 2θ value of 25.78° . However, after Nb- and Zr-doping the (101) diffraction peaks of the Ti-Nb-Zr-O samples gradually shifted from 25.78° to 25.05° with increase of the Zr content. This performance should be mainly attributed to the change of TiO_2 lattice parameter because of the larger radius of Zr^{4+} (0.72 \AA) compared to that of Ti^{4+} (0.61 \AA) [26].

4. Conclusions

In summary, anodic Ti-Nb-Zr-O nanotube arrays were grown on Ti-Nb-Zr alloy substrates in 1M NaH_2PO_4

containing 0.5 wt% HF electrolytes. The average length of the Ti-Nb-Zr-O nanotubes increased with increase of the Zr content. The anodic current for the Ti-Nb-Zr alloy with higher Zr content was larger than that with lower Zr content at the same anodization voltage. XRD analysis indicated that the Ti-Nb-Zr-O oxides annealed at 500°C were anatase phase. The diffraction peaks shifted to lower 2θ values with increase of the Zr content because of the larger radius of Zr^{4+} compared to that of Ti^{4+} . The formation of Ti-Nb-Zr-O nanotubes for the system with a higher Zr content was relatively easier.

Conflict of Interests

The authors declare that there is no conflict of interests regarding the publication of this paper.

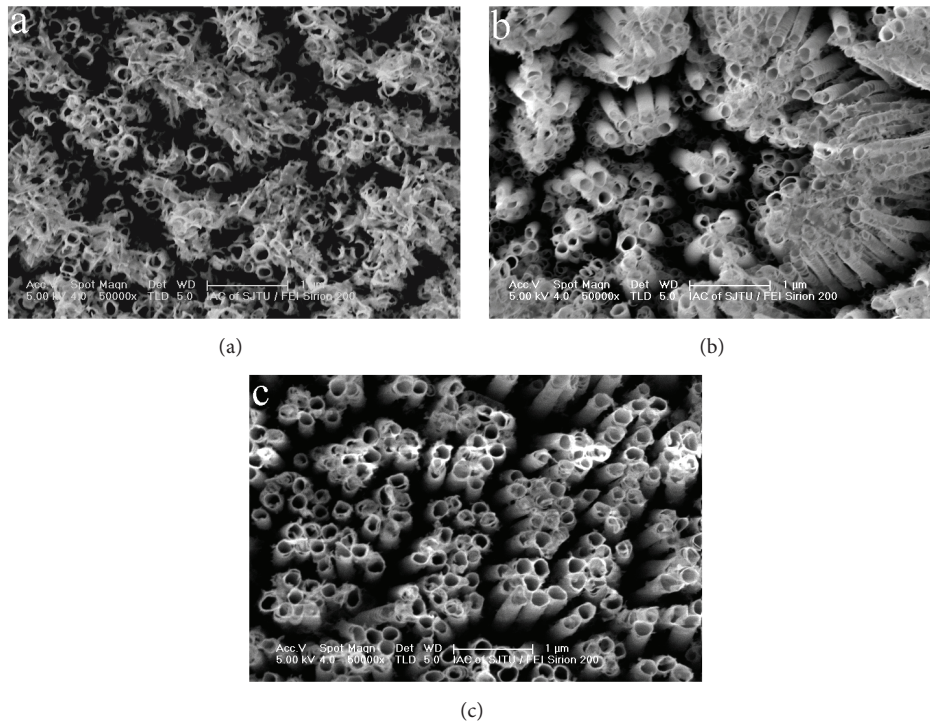


FIGURE 4: SEM images of Ti-Nb-Zr-O nanotubes grown on different Ti-Nb-Zr alloy substrates at 40 V with a constant frequency of 2000 Hz and duty cycle of 20% for 90 minutes, (a) Ti₃₅Nb₅Zr, (b) Ti₃₅Nb₁₀Zr, and (c) Ti₃₅Nb₁₅Zr.

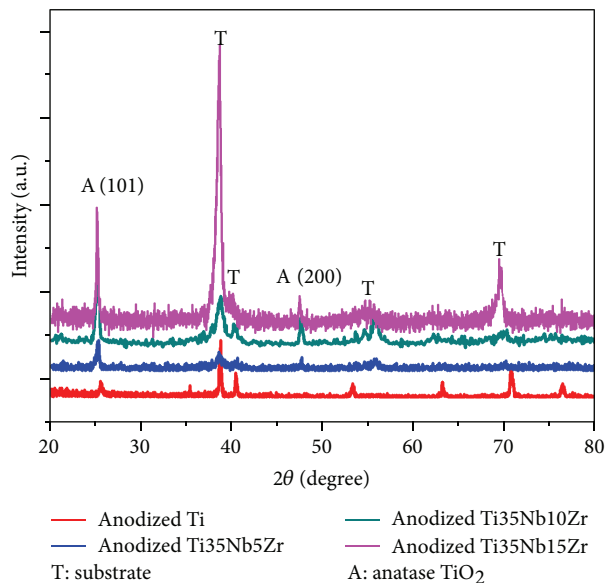


FIGURE 5: XRD patterns of Ti-Nb-Zr-O nanotubes grown on different Ti-Nb-Zr alloy substrates at 40 V with a constant frequency of 4000 Hz and duty cycle of 20% for 90 minutes.

Acknowledgments

This work was supported by Shanghai Pujiang Program (no. 07pj14047). The authors thank the contribution from SEM Lab at Instrumental Analysis Center of SJTU.

References

- [1] H. Kato, K. Asakura, and A. Kudo, "Highly efficient water splitting into H₂ and O₂ over lanthanum-doped NaTaO₃ photocatalysts with high crystallinity and surface nanostructure," *Journal of the American Chemical Society*, vol. 125, no. 10, pp. 3082–3089, 2003.
- [2] E. Rossinyol, J. Arbiol, F. Peiró et al., "Nanostructured metal oxides synthesized by hard template method for gas sensing applications," *Sensors and Actuators B: Chemical*, vol. 109, no. 1, pp. 57–63, 2005.
- [3] X. Fang, Y. Bando, U. K. Gautam, C. Ye, and D. Golberg, "Inorganic semiconductor nanostructures and their field-emission applications," *Journal of Materials Chemistry*, vol. 18, no. 5, pp. 509–522, 2008.
- [4] H. Rensmo, K. Keis, H. Lindström et al., "High light-to-energy conversion efficiencies for solar cells based on nanostructured ZnO electrodes," *Journal of Physical Chemistry B*, vol. 101, no. 14, pp. 2598–2601, 1997.
- [5] A. Fujishima and K. Honda, "Electrochemical photolysis of water at a semiconductor electrode," *Nature*, vol. 238, no. 5358, pp. 37–38, 1972.
- [6] S. In, A. Orlov, R. Berg et al., "Effective visible light-activated B-doped and B,N-codoped TiO₂ photocatalysts," *Journal of the American Chemical Society*, vol. 129, no. 45, pp. 13790–13791, 2007.
- [7] F. N. Sayed, O. D. Jayakumar, R. Sasikala et al., "Photochemical hydrogen generation using nitrogen-doped TiO₂-Pd nanoparticles: facile synthesis and effect of Ti³⁺ incorporation," *The Journal of Physical Chemistry C*, vol. 116, pp. 12462–12467, 2012.
- [8] K. Nagaveni, M. S. Hegde, and G. Madras, "Structure and photocatalytic activity of Ti_{1-x}M_xO_{2δ} (M= W, V, Ce, Zr, Fe, and

- Cu) synthesized by solution combustion method,” *Journal of Physical Chemistry B*, vol. 108, no. 52, pp. 20204–20212, 2004.
- [9] M. Hirano and K. Matsushima, “Photoactive and adsorptive niobium-doped anatase (TiO_2) nanoparticles: influence of hydrothermal conditions on their morphology, structure, and properties,” *Journal of the American Ceramic Society*, vol. 89, no. 1, pp. 110–117, 2006.
- [10] S.-M. Chang and R.-A. Doong, “Characterization of Zr-doped TiO_2 nanocrystals prepared by a nonhydrolytic sol-gel method at high temperatures,” *Journal of Physical Chemistry B*, vol. 110, no. 42, pp. 20808–20814, 2006.
- [11] H. Zhang, P. Liu, X. Liu et al., “Fabrication of highly ordered TiO_2 nanorod/nanotube adjacent arrays for photoelectrochemical applications,” *Langmuir*, vol. 26, no. 13, pp. 11226–11232, 2010.
- [12] T. Kasuga, M. Hiramatsu, A. Hoson, T. Sekino, and K. Niihara, “Formation of titanium oxide nanotube,” *Langmuir*, vol. 14, no. 12, pp. 3160–3163, 1998.
- [13] B. Liu and E. S. Aydil, “Growth of oriented single-crystalline rutile TiO_2 nanorods on transparent conducting substrates for dye-sensitized solar cells,” *Journal of the American Chemical Society*, vol. 131, no. 11, pp. 3985–3990, 2009.
- [14] C. Ruan, M. Paulose, O. K. Varghese, G. K. Mor, and C. A. Grimes, “Fabrication of highly ordered TiO_2 nanotube arrays using an organic electrolyte,” *Journal of Physical Chemistry B*, vol. 109, no. 33, pp. 15754–15759, 2005.
- [15] N. K. Allam, A. J. Poncheri, and M. A. El-Sayed, “Vertically oriented Ti-Pd mixed oxynitride nanotube arrays for enhanced photoelectrochemical water splitting,” *ACS Nano*, vol. 5, no. 6, pp. 5056–5066, 2011.
- [16] F. M. Bayoumi and B. G. Ateya, “Formation of self-organized titania nano-tubes by dealloying and anodic oxidation,” *Electrochemistry Communications*, vol. 8, no. 1, pp. 38–44, 2006.
- [17] H. Liu, D. Ding, C. Ning, and Z. Li, “Wide-range hydrogen sensing with Nb-doped TiO_2 nanotubes,” *Nanotechnology*, vol. 23, no. 1, Article ID 015502, 2012.
- [18] N. K. Allam, F. Alangir, and M. A. El-Sayed, “Enhanced photoassisted water electrolysis using vertically oriented anodically fabricated Ti-Nb-Zr-O mixed oxide nanotube arrays,” *ACS Nano*, vol. 4, no. 10, pp. 5819–5826, 2010.
- [19] Z. H. Li, C. Q. Ning, D. Y. Ding, H. G. Liu, and L. Huang, “Biological properties of Ti-Nb-Zr-O nanostructures grown on $\text{Ti}_{35}\text{Nb}_5\text{Zr}$ alloy,” *Journal of Nanomaterials*, vol. 2012, Article ID 834042, 7 pages, 2012.
- [20] A. Ghicov and P. Schmuki, “Self-ordering electrochemistry: a review on growth and functionality of TiO_2 nanotubes and other self-aligned MO_x structures,” *Chemical Communications*, no. 20, pp. 2791–2808, 2009.
- [21] K. Yasuda and P. Schmuki, “Control of morphology and composition of self-organized zirconium titanate nanotubes formed in $(\text{NH}_4)_2\text{SO}_4/\text{NH}_4\text{F}$ electrolytes,” *Electrochimica Acta*, vol. 52, no. 12, pp. 4053–4061, 2007.
- [22] G. Z. Li, H. P. Tang, W. Y. Zhang, G. Li, L. L. Yu, and Y. N. Li, “Fabrication of multilayer Nb_2O_5 nanoporous film by anodization of niobium foils,” *Rare Metals*, 2013.
- [23] H. Habazaki, M. Uozumi, H. Konno et al., “Influences of structure and composition on growth of anodic oxide films on Ti-Zr alloys,” *Electrochimica Acta*, vol. 48, no. 20-22, pp. 3257–3266, 2003.
- [24] H. Tsuchiya, J. M. MacAk, A. Ghicov, L. Taveira, and P. Schmuki, “Self-organized porous TiO_2 and ZrO_2 produced by anodization,” *Corrosion Science*, vol. 47, no. 12, pp. 3324–3335, 2005.
- [25] X. J. Feng, J. M. Macak, S. P. Albu, and P. Schmuki, “Electrochemical formation of self-organized anodic nanotube coating on Ti-28Zr-8Nb biomedical alloy surface,” *Acta Biomaterialia*, vol. 4, no. 2, pp. 318–323, 2008.
- [26] X. Lü, X. Mou, J. Wu et al., “Improved-performance dye-sensitized solar cells using Nb-doped TiO_2 electrodes: efficient electron injection and transfer,” *Advanced Functional Materials*, vol. 20, no. 3, pp. 509–515, 2010.

Research Article

Tuning Optical Nonlinearity of Laser-Ablation-Synthesized Silicon Nanoparticles via Doping Concentration

Lianwei Chen,¹ Xiao-fang Jiang,² Ziming Guo,¹ Hai Zhu,² Tsung-Sheng Kao,³ Qing-hua Xu,² Ghim Wei Ho,¹ and Minghui Hong³

¹ Engineering Science Program, National University of Singapore, 4 Engineering Drive 3, Singapore 117576

² Department of Chemistry, National University of Singapore, 3 Science Drive 3, Singapore 117543

³ Department of Electrical and Computer Engineering, National University of Singapore, 4 Engineering Drive 3, Singapore 117576

Correspondence should be addressed to Minghui Hong; elehmh@nus.edu.sg

Received 13 November 2013; Accepted 24 January 2014; Published 3 March 2014

Academic Editor: Mohsen Rahmani

Copyright © 2014 Lianwei Chen et al. This is an open access article distributed under the Creative Commons Attribution License, which permits unrestricted use, distribution, and reproduction in any medium, provided the original work is properly cited.

Silicon nanoparticles at different doping concentrations are investigated for tuning their optical nonlinear performance. The silicon nanoparticles are synthesized from doped silicon wafers by pulsed laser ablation. Their dispersions in water are studied for both nonlinear absorption and nonlinear refraction properties. It is found that the optical nonlinear performance can be modified by the doping concentration. Nanoparticles at a higher doping concentration exhibit better saturable absorption performance for femtosecond laser pulse, which is ascribed to the free carrier absorption mechanism.

1. Introduction

The optical nonlinear properties of nanomaterials have been extensively studied for the applications in high power laser devices. Among all these materials, silicon materials have triggered particularly high research interests because of their potential to be integrated with microelectronics [1, 2]. One of the primary arguments in favor of silicon optical materials is the possibility to build chip-scale photonic devices, which motivates intensive investigations on optical nonlinear properties of silicon materials in nanoscale [3–6].

In addition to its compatibility with the industry, silicon nanomaterials have many other advantages. Traditional materials like gold and silver are not cost efficient. Comparing to them, silicon has a rich source of supply and low processing cost. Different from most of organic optical nonlinear materials, silicon is promising for the biomedical applications due to its minimum toxicity. Synthesis methods have been reported to produce pure silicon materials with little chemical precursors [7, 8]. Meanwhile, the flourishing silicon industry and mature processing technique make it possible to precisely fabricate silicon nanoscale structures with modified intrinsic properties. Therefore, silicon emerges as a good candidate

to be a cheap and environmental friendly optical nonlinear material.

In the past decades, various silicon nanostructures were studied for their unique optical properties, such as porous silicon materials, silicon nanofibers, silicon nanoclusters, and nanoparticles [3, 9–14]. In these studies, silicon morphology was reported to be an important factor affecting the optical nonlinearity. Meanwhile, researchers also studied the silicon in different surrounding matrices, which was crucial for the optical nonlinear performance [14]. Other key factors include the density of free carriers. Since free carrier absorption is a nonlinear process, better optical nonlinearity is expected for silicon material with a large number of free carriers [12]. However, insufficient experiment data on the effect of the free carrier concentration have been reported. In this paper, a set of experiments are designed and presented to provide a better understanding on how the optical nonlinearity is affected by the density of free carriers.

The change of free carrier density is achieved by the tuning of the doping concentration in silicon. The dispersions of the silicon nanoparticles in water are synthesized and studied for the optical nonlinearity. These Si nanoparticles are produced by pulsed laser ablation in deionized (DI) water

TABLE 1: Surface resistivity and doping concentration of silicon wafers.

Number	Surface resistivity ($\Omega\cdot\text{cm}$)	Doping concentration (cm^{-3})
P1	0.01	$8.1E18$
P2	1.50	$1.0E16$
P3	4.90	$2.8E15$
P4	10.50	$1.3E15$
P5	16.50	$8.3E14$
N1	0.80	$8.4E16$
N2	0.10	$8.2E16$
N3	4.50	$1.0E15$
N4	8.00	$5.6E14$
N5	19.0	$2.3E14$

to form a stable dispersion. Nonlinear optical properties are characterized by the open and close aperture Z -scan methods. It is found that the increase of doping concentration enhances the optical nonlinear response, which opens a new way to tune the optical nonlinearity. Different from the modification of the morphology and environment, it is more flexible to tune the optical nonlinearity by simply varying the doping concentration.

2. Synthesis of Nanoparticle Dispersion

One-side polished silicon wafers were bought from the LiJingKeJi Ltd. N-type samples were doped with phosphorus and P-type samples were doped with boron. For each sample, the average sheet resistivity was recorded. The doping concentrations were calculated from the sheet resistance [15]. All these data are summarized in Table 1.

Pulsed laser ablation was applied to synthesize the silicon nanoparticles [16, 17]. In each experiment, a clean silicon wafer in the dimension of $1\text{ cm} \times 1\text{ cm}$ was positioned at the center of a 25 mL glass beaker, with the unpolished side facing towards the incident laser beam. The beaker was then put into a sample holder on the processing stage. The diagram of the experimental setup is shown in Figure 1(a), which was discussed in the previous work [18, 19]. The Nd:YAG fiber laser at the wavelength of 1064 nm (IDI Laser Service) was used for the laser ablation. The pulse duration (full width at half maximum) was 1.5 ns. The repetition rate was 60 kHz and the focal length used was 10 cm.

The laser beam was programmed to scan over a $1\text{ cm} \times 1\text{ cm}$ area for 900 times. A rectangular scanning pattern was chosen and the scanning speed was set at 1 mm/s. The laser fluence for the synthesis of silicon nanoparticles was kept at $0.8\text{ J}/\text{cm}^2$ at the focal point throughout the process. The entire process took about 6 minutes. After the laser ablation was completed, the color of the solvent changed into light brown, which resulted from the dispersion of the silicon nanoparticles inside the water.

Same parameters for the laser ablation were applied to synthesize silicon nanoparticles at different doping concentrations. The dispersions were collected and sonicated for 30

minutes to ensure the silicon nanoparticles are being well-dispersed in water. All the silicon nanoparticles' dispersions were placed at rest for one day to test the stability and no aggregations were observed. To calculate the nanoparticles' concentration, 30 cycles of the laser ablation were repeated on one silicon wafer and the average weight change per cycle was calculated. The mass loss of the silicon wafer in each cycle equals the total mass of the silicon nanoparticles synthesized and the nanoparticles' concentration can be estimated to be 5 mM.

3. Results and Discussion

3.1. Silicon Nanoparticles' Morphology and Size Distribution. SEM images were taken to characterize the morphology and size distribution of the silicon nanoparticles synthesized by the laser ablation. The dispersion was dropped onto an undoped silicon substrate and then observed under a high resolution Jeol JSM7001F SEM. The image of the silicon nanoparticles' morphology is shown in Figure 1(b). It is clear that most silicon nanoparticles are in sphere shape. The sizes of 100 nanoparticles were measured and the size distribution is shown in Figure 1(c). It can be seen that the size distribution ranges broadly from 0 to 400 nm, while the distribution peak locates at 100–200 nm. It is found in our experiment that, regardless of the doping concentration, the size distribution is similar to different samples. A schematic diagram of the laser ablation mechanism for the silicon nanoparticles' synthesis is shown in Figure 1(d). In the synthesis process, a rapid transfer of the energy from photons to the lattice causes the silicon materials to evaporate, which results in the generation of expanding plasma. This plasma is made of energetic species including atoms, molecules, ions, clusters, and dopants. During the expanding process, the plasma is confined by the surrounding water molecules under high pressure. The energetic species in the plasma collide with the surrounding water molecules and the kinetic energy is reduced. This strong hyperthermal reaction between the ablated energetic species and the surrounding water molecules promotes the nucleation and aggregation to form the nanoparticles. The silicon doping concentrations in our experiments are from 2.3×10^{14} to $8.1 \times 10^{18}\text{ cm}^{-3}$. The number of dopants is much smaller compared to that of silicon atoms. Therefore, the generation of energetic species is similar to silicon materials at different doping concentrations. In the same conditions, the plasma expansion and nucleation process are identical. As a result, silicon nanoparticles synthesized exhibit similar morphology and size distribution at different doping concentrations.

3.2. Absorption Spectrum of Silicon Nanoparticles. The absorption spectra of the silicon nanoparticles' dispersions were characterized by a Shimadzu UV-3600 UV-VIS-NIR spectrophotometer. The dispersions were heated on a hot plate to increase the nanoparticles' concentration in order to enhance the absorption features of silicon nanoparticles. The concentrated dispersions were sonicated for 10 minutes and transferred into a quartz cell with 1 cm light path length

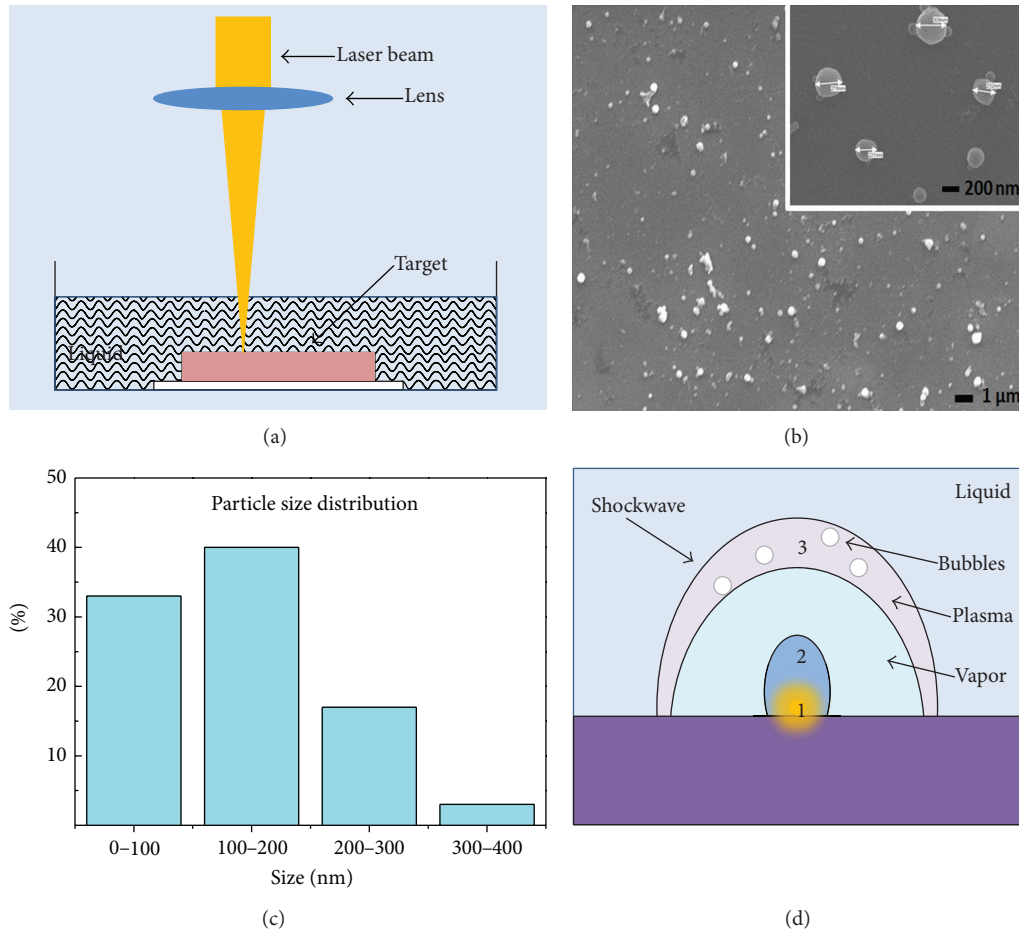


FIGURE 1: (a) Diagram of the laser ablation for silicon nanoparticles' synthesis. (b) SEM images of the silicon nanoparticles; inset: zoom-in image. (c) Particle size distribution of the silicon nanoparticles. (d) Laser plasma plume formation induced by laser ablation at different stages of (1) initial, (2) expansion, and (3) saturation.

for characterization. The absorption spectra from 350 to 1200 nm are shown in Figure 2. Inset of Figure 2 is the optical image of the silicon nanoparticles' dispersions to show their colors. The absorption spectra are similar to both P-type and N-type silicon nanoparticles' dispersions. The absorption increases at a short wavelength and reaches its peak at around 420 nm, which is in good agreement with the previous reported results [14, 20]. This absorption peak corresponds to the energy level of singularities in the electron density function [20].

3.3. Silicon Nanoparticles' Nonlinear Absorption and Nonlinear Refraction Properties. To characterize the nonlinear optical response, both open and close aperture Z-scan experiments were conducted. The Z-scan measurement was performed by using a regenerative Ti:Sapphire amplifier (Libra, Coherent), which gave output laser pulses with a central wavelength of 800 nm, pulse duration of around 100 fs, and repetition rate of 1 kHz. In our previous research, the same setup was applied to study the optical nonlinearity of graphene oxide [21].

The sample was sonicated for 30 minutes before the experiment to avoid aggregation. After sonication, the dispersion was transferred into a quartz cuvette with 1 mm optical path length, which was then placed at the starting location of the stage ($Z = -8$ mm). The Z-scan range was set from -8 to 8 mm. The aperture was adjusted to be fully open for the open aperture Z-scan measurement and 30% transmittance of the initial beam for the close aperture Z-scan experiment. Three cycles were repeated to reduce the experimental error and the average was calculated to plot the Z-scan curves.

The nonlinear absorption of the P-type silicon nanoparticles was examined by open aperture Z-scan method at the wavelength of 800 nm. The incident laser fluence is 40 mJ/cm^2 at the focal point. Results are shown in Figure 3(a). As a comparison, the transmittance curve of water was also plotted. It can be seen that the water does not show any change in the transmittance at different Z positions, which indicates that it does not have any observable nonlinear effect under our experiment conditions. Meanwhile, all the P-type silicon nanoparticles show clear features of the saturable absorption. Comparing the curves for samples at different doping concentrations, it can be found that the peak transmittance

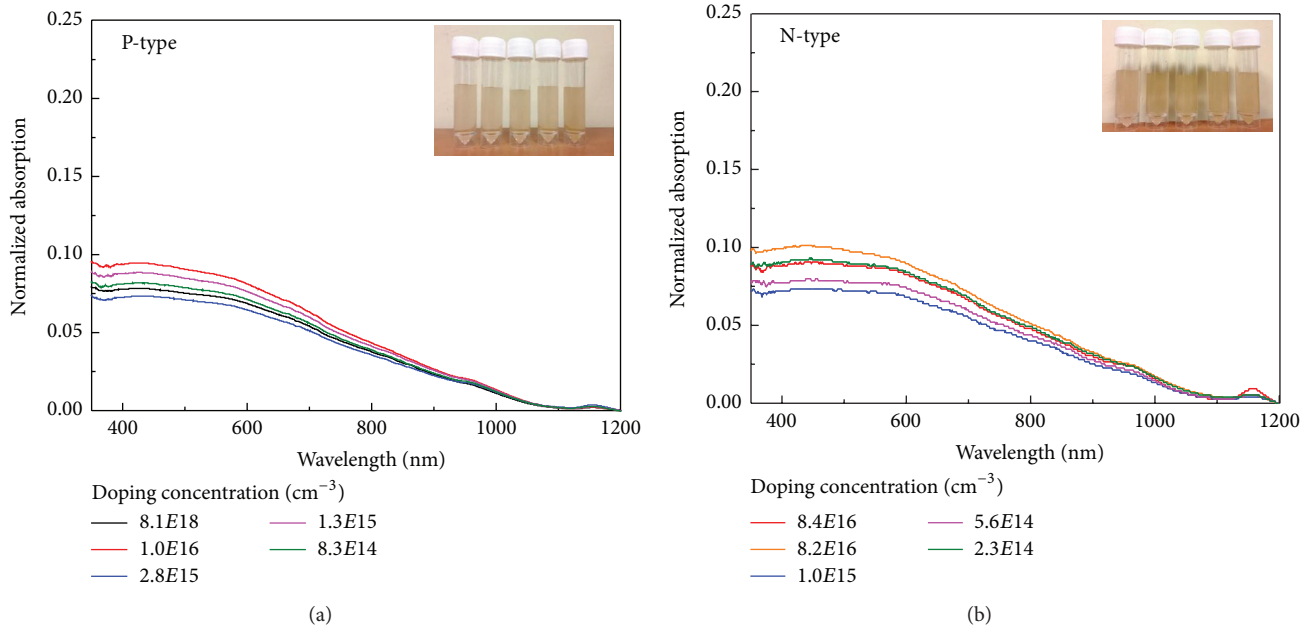


FIGURE 2: Absorption spectra for (a) P-type and (b) N-type silicon nanoparticles dispersions; inset: optical image of the dispersions.

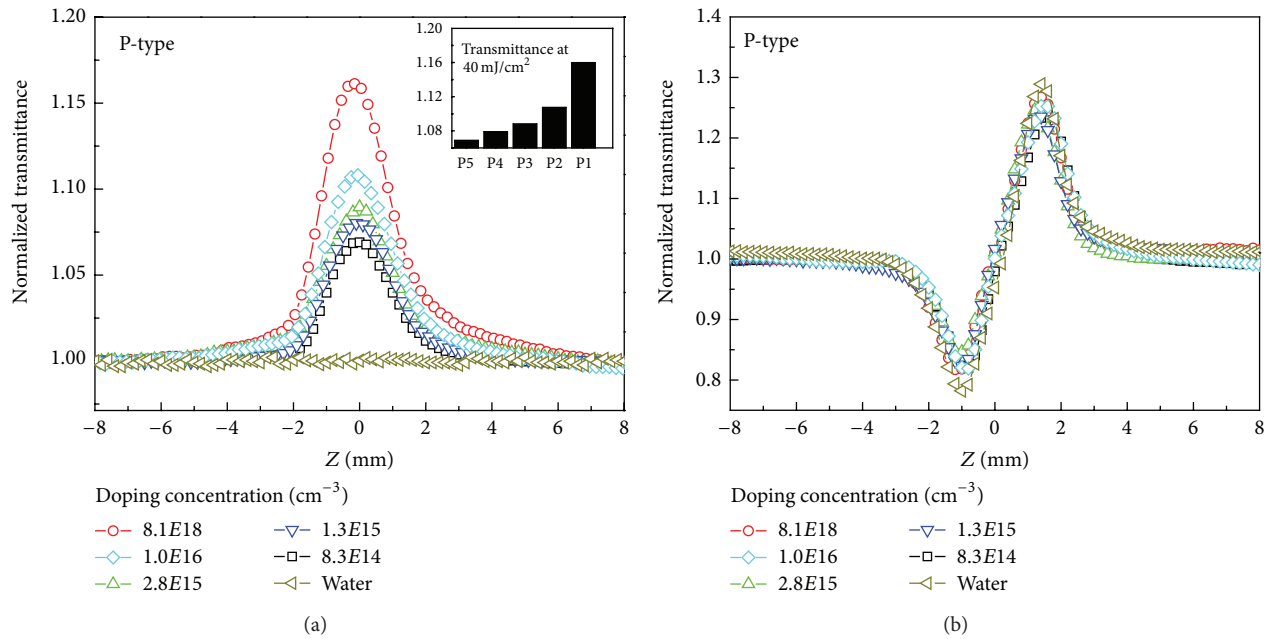


FIGURE 3: (a) Open aperture Z-scan curves for P-type silicon nanoparticle dispersions; inset: peak transmittance at different doping concentrations. (b) Close aperture Z-scan curves for P-type silicon nanoparticles' dispersions.

increases as the doping concentration increases, which indicates that the saturated nonlinear absorption is enhanced by the dopants. Among all the samples, the sample at the doping concentration of $8.1 \times 10^{18} \text{ cm}^{-3}$ presented a significant enhancement of the nonlinear absorption. Comparing to the silicon nanoparticles at the doping concentration of $8.3 \times 10^{14} \text{ cm}^{-3}$, the peak transmission was enhanced by 10%.

These different optical nonlinear responses related to the doping concentration can be explained by the mechanism of free carrier absorption [12]. Once generated, the free carriers can be promoted to a higher energy level by the absorption of photons. The probability for one free carrier to jump into a certain level is defined as the cross section. The saturated absorption is caused by the different cross

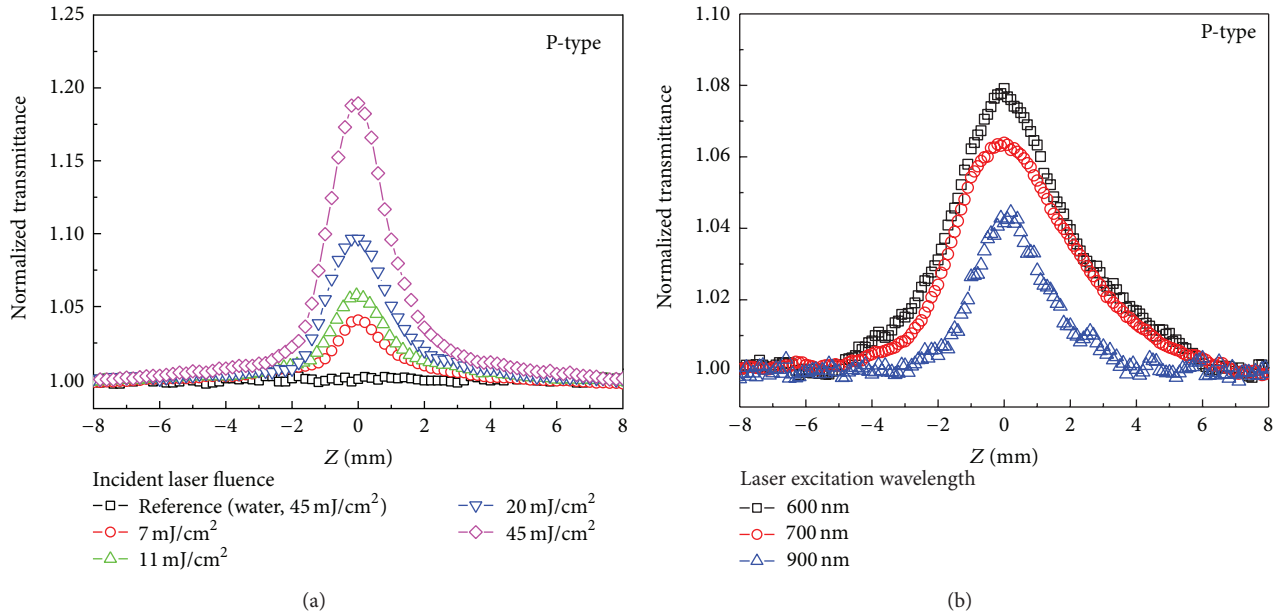


FIGURE 4: (a) Open aperture Z-scan curves at different incident laser fluences at the focal point. (b) Open aperture Z-scan curves at the laser excitation wavelengths of 600, 700, and 900 nm.

sections of the excitation levels. When the cross section for a higher excitation level is small, free carriers are not likely to jump up to the higher level and fail to absorb the laser energy, which causes the absorption to be “saturated” and the transmission to increase. The free carrier absorption is clearly an accumulative process, which relies on the buildup of the free carrier population. The nonlinear effect is in positive correlation with the density of the free carriers. When more free carriers fail to jump up to a higher level, the absorption becomes saturated more readily; thus, the increase of the free carriers can enhance the optical nonlinearity. A heavily doped sample has a larger number of free carriers, which is consistent with our observation that the sample with the highest doping concentration shows the most significant enhancement of the saturable absorption [12].

Close aperture Z-scan was conducted to verify whether the doping concentration influences the optical nonlinear refraction of the silicon nanoparticles. The transmittance curves are summarized in Figure 3(b). Experimental conditions were the same as those in the open aperture Z-scan measurement except that the aperture was set to 30% transmittance of the initial beam. The transmittance of water was also plotted as a reference, which exhibits the features of the self-focusing. The curves for the silicon nanoparticles’ dispersions and water are very similar. The reason can be explained as follows. The refractive index variation at different laser intensities is responsible for the nonlinear optical effect. Since the concentration of the silicon nanoparticles is low in water, refractive index variation is mainly affected by water. As a consequence, little enhancement of nonlinear refraction can be observed.

To build up a comprehensive understanding of the optical nonlinear response, the open aperture Z-scan measurements

with different excitation fluences and wavelengths were performed. The results on the P-type silicon nanoparticles with the doping concentration of $8.1 \times 10^{18} \text{ cm}^{-3}$ were chosen to be presented for illustration purpose. The results for laser fluence dependence at the excitation wavelength of 800 nm are shown in Figure 4(a). It is clear that the peak transmittance increases with the incident laser fluence. This observation can be ascribed to more free carriers generated at the higher laser fluence. Furthermore, comparing to other samples, a less intensive laser excitation is required to reach an identical peak transmittance. At the incident laser fluence of 11 mJ/cm^2 , the peak transmittance is 1.06 (Note: the transmittance is normalized to the linear transmittance at the initial Z-scan position, where there is no nonlinear absorption. 1.06 means the peak transmittance is 106% of the linear transmittance at the initial Z-scan position). For sample at the doping concentration of $8.3 \times 10^{14} \text{ cm}^{-3}$, the incident laser fluence needs to be increased to 40 mJ/cm^2 to have a comparable peak transmittance around 1.06, which is shown in Figure 3(a). As the identical peak transmittance means the same level of nonlinear absorption, it can be concluded that, in order to achieve an identical level of saturated nonlinear absorption, samples at high doping concentrations need a less intense laser than the samples at low doping concentrations. For the highly doped samples, its high free carrier density enables electrons to be more readily excited by laser pulses, which explains why they need lower laser fluence to achieve the same nonlinear response.

The broadband performance was also characterized at the laser excitation wavelength of 600, 700, and 900 nm using an optical parametric amplifier (Topas C). The incident laser fluence was set at 11 mJ/cm^2 at all these wavelengths.

The transmittance curves of the open aperture Z-scan measurement are shown in Figure 4(b). It can be seen that silicon nanoparticles exhibit optical nonlinear responses at all these excitation laser wavelengths and the optical nonlinear response is the strongest at the wavelength of 600 nm. This can be explained by the higher absorptions of silicon nanoparticles at a short wavelength, as shown in Figure 2. A larger absorption results in a larger amount of energy transferred to the silicon nanoparticles upon excitation. As a consequence, more free carriers are generated and excited. As these free carriers are hindered to jump up to a higher level due to the small cross section, the absorption becomes more saturated, which explains the enhancement of the optical nonlinearity.

The optical nonlinear response of N-type silicon samples was also characterized using the same Z-scan setups in our experiments. It was discovered that the increase of the doping concentration can enhance the nonlinear absorption, which can be explained similarly using the free carrier absorption mechanism. However, at same doping concentration, P-type silicon nanoparticles show stronger saturable absorption behavior than N-type silicon nanoparticles, which indicates that P-type silicon nanoparticles have better nonlinear response. This difference is due to their different cross sections of the excitation levels in two cases. The free carriers for P-type and N-type silicon materials are holes and electrons, respectively. Holes and electrons have different effective masses and momentum relaxing time, which influence the cross sections of the excitation levels [22].

4. Conclusions

Silicon nanoparticles' dispersions were synthesized by the pulsed laser ablation and their optical nonlinear responses were investigated. Under the same synthesis conditions, these silicon nanoparticles have similar morphology and size distribution. It is shown that the increase of the doping concentration leads to a stronger nonlinear absorption, while the nonlinear refraction is not changed much. This enhancement can be explained by the free carrier absorption mechanism. The characterization at different wavelengths proves that the silicon nanoparticles have a broadband nonlinear response and the optical nonlinearity is stronger at a shorter wavelength. This research reveals the possibility to tune the optical nonlinearity of silicon nanoparticles via doping concentration.

Conflict of Interests

The authors declare that there is no conflict of interests regarding the publication of this paper.

Acknowledgment

The authors are grateful for financial support from the Temasek Defence Systems Institute (TDSI) under Project no. TDSI/II-013/1A.

References

- [1] B. Jalali and S. Fathpour, "Silicon photonics," *Journal of Lightwave Technology*, vol. 24, no. 12, pp. 4600–4615, 2006.
- [2] M. Lipson, "Guiding, modulating, and emitting light on Silicon—challenges and opportunities," *Journal of Lightwave Technology*, vol. 23, no. 12, pp. 4222–4238, 2005.
- [3] R. Dekker, N. Usechak, M. Först, and A. Driessen, "Ultrafast nonlinear all-optical processes in silicon-on-insulator waveguides," *Journal of Physics D*, vol. 40, no. 14, pp. R249–R271, 2007.
- [4] L. A. Golovan and V. Y. Timoshenko, "Nonlinear-optical properties of porous silicon nano-structures," *Journal of Nanoelectronics and Optoelectronics*, vol. 8, pp. 223–239, 2013.
- [5] J. Leuthold, C. Koos, and W. Freude, "Nonlinear silicon photonics," *Nature Photonics*, vol. 4, no. 8, pp. 535–544, 2010.
- [6] Q. Lin, O. J. Painter, and G. P. Agrawal, "Nonlinear optical phenomena in silicon waveguides: modeling and applications," *Optics Express*, vol. 15, no. 25, pp. 16604–16644, 2007.
- [7] R. Intartaglia, K. Bagga, M. Scotto, A. Diaspro, and F. Brandi, "Luminescent silicon nano-particles prepared by ultra short pulsed laser ablation in liquid for imaging applications," *Optical Materials Express*, vol. 2, pp. 510–518, 2012.
- [8] N. G. Semaltianos, S. Logothetidis, W. Perrie et al., "Silicon nanoparticles generated by femtosecond laser ablation in a liquid environment," *Journal of Nanoparticle Research*, vol. 12, pp. 573–580, 2010.
- [9] P. Cheng, H. Zhu, Y. Bai, Y. Zhang, T. He, and Y. Mo, "Third-order nonlinear optical response of silicon nanostructures dispersed in organic solvent under 1064 nm and 532 nm laser excitations," *Optics Communications*, vol. 270, no. 2, pp. 391–395, 2007.
- [10] V. Klimov, D. McBranch, and V. Karavanskii, "Strong optical nonlinearities in porous silicon: femtosecond nonlinear transmission study," *Physical Review B*, vol. 52, no. 24, pp. R16989–R16992, 1995.
- [11] S. B. Korovin, V. I. Pustovoi, and A. N. Orlov, "High nonlinear susceptibility of the silicon based nanostructures," in *Proceedings of the International Conference on Advanced Laser Technologies (ALT '99)*, V. I. Pustovoy and V. I. Konov, Eds., pp. 472–478, 2000.
- [12] L. W. Tutt and T. F. Boggess, "A review of optical limiting mechanisms and devices using organics, fullerenes, semiconductors and other materials," *Progress in Quantum Electronics*, vol. 17, no. 4, pp. 299–338, 1993.
- [13] S. Vijayalakshmi, F. Shen, and H. Grebel, "Artificial dielectrics: nonlinear optical properties of silicon nanoclusters at $\lambda = 532$ nm," *Applied Physics Letters*, vol. 71, no. 23, pp. 3332–3334, 1997.
- [14] E. Koudoumas, O. Kokkinaki, M. Konstantaki et al., "Nonlinear optical response of silicon nanocrystals," *Optical Materials*, vol. 30, no. 2, pp. 260–263, 2007.
- [15] G. Masetti, M. Severi, and S. Solmi, "Modeling of carrier mobility against carrier concentration in arsenic-, phosphorus-, and boron-doped silicon," *IEEE Transactions on Electron Devices*, vol. 30, no. 7, pp. 764–769, 1983.
- [16] T. C. Chong, M. H. Hong, and L. P. Shi, "Laser precision engineering: from microfabrication to nanoprocessing," *Laser and Photonics Reviews*, vol. 4, no. 1, pp. 123–143, 2010.
- [17] M. H. Hong, "Laser-material interaction and its applications in surface micro/nano-processing," in *Proceedings of the International Symposium on High Power Laser Ablation*, C. R. Phipps,

Ed., pp. 293–302, American Institute of Physics, Melville, NY, USA, 2010.

- [18] G. X. Chen, M. H. Hong, T. C. Chong, H. I. Elim, G. H. Ma, and W. Ji, “Preparation of carbon nanoparticles with strong optical limiting properties by laser ablation in water,” *Journal of Applied Physics*, vol. 95, no. 3, pp. 1455–1459, 2004.
- [19] G. X. Chen, M. H. Hong, T. S. Ong et al., “Carbon nanoparticles based nonlinear optical liquid,” *Carbon*, vol. 42, no. 12-13, pp. 2735–2737, 2004.
- [20] S. B. Korovin, A. N. Orlov, A. M. Prokhorov et al., “Nonlinear absorption in silicon nanocrystals,” *Quantum Electronics*, vol. 31, no. 9, pp. 817–820, 2001.
- [21] X.-F. Jiang, L. Polavarapu, S. T. Neo, T. Venkatesan, and Q.-H. Xu, “Graphene oxides as tunable broadband nonlinear optical materials for femtosecond laser pulses,” *Journal of Physical Chemistry Letters*, vol. 3, no. 6, pp. 785–790, 2012.
- [22] C. M. Wolfe, N. Holonyak, and G. E. Stillman, *Physical Properties of Semiconductors*, Prentice Hall, Upper Saddle River, NJ, USA, 1989.

Research Article

Behavior of Yb³⁺ and Er³⁺ during Heat Treatment in Oxyfluoride Glass Ceramics

M. H. Imanieh,^{1,2} I. R. Martín,^{3,4} J. Gonzalez-Platas,^{5,6} B. Eftekhari Yekta,² V. K. Marghussian,² and S. Shakhesi⁷

¹ Department of Chemical and Environmental Engineering, University of Toledo, Toledo, OH 43606, USA

² Ceramic Division, Department of Materials, Iran University of Science and Technology, Narmak, Tehran 1684613114, Iran

³ Departamento de Física Fundamental y Experimental, Electrónica y Sistemas, Universidad de La Laguna, Avenida Astrofísico Francisco Sánchez, La Laguna, 38206 Tenerife, Spain

⁴ MALTA Consolider Team, La Laguna, 38206 Tenerife, Spain

⁵ Departamento de Física Fundamental II, Tenerife, Spain

⁶ Servicio Integrado de Difracción de Rayos X, Tenerife, Spain

⁷ Nanotechnology Department, Engineering Research Institute, Tehran 1465774111, Iran

Correspondence should be addressed to M. H. Imanieh; mahammad.imanieh@utoledo.edu

Received 7 September 2013; Revised 2 December 2013; Accepted 6 December 2013; Published 2 January 2014

Academic Editor: Mohsen Rahmani

Copyright © 2014 M. H. Imanieh et al. This is an open access article distributed under the Creative Commons Attribution License, which permits unrestricted use, distribution, and reproduction in any medium, provided the original work is properly cited.

The effects of alumina content and heat treatment on upconversion properties of codoped (ErF₃-YbF₃) oxyfluoride glass ceramics were investigated. Results showed that alumina content had an effect on phase separation and viscosity of the glass. Due to the high viscosity of low alumina content glass, the phase separated areas were smaller in these specimens. Increasing the heat treatment temperature led to the incorporation of Er³⁺ ions into CaF₂ crystals and also increased the Yb³⁺ concentration in them. This increase improved the energy transfer and back transfer process between Er³⁺ and Yb³⁺ ions and as result upconversion intensity was increased.

1. Introduction

At present, there is great interest in luminescent materials for efficient frequency conversion from infrared to visible radiation, mainly because a visible source pumped by a near infrared laser is useful for high-capacity data storage optical devices [1]. This process can be obtained by upconversion mechanisms, where several infrared photons can be absorbed by the material doped with rare earth ions (RE) in order to populate more energetic levels. Therefore, both the fluorescence lifetime and the stimulated emission cross-section of the RE excited level should be maximized, whereas the nonradiative decay mechanisms should be minimized [2].

Oxyfluoride glass ceramics are ambivalent materials. Despite the fact that they are mainly oxide glasses, they can exhibit optical properties of fluoride single crystals when they are doped with rare earth ions. They are often called nanocomposite materials. Their weird character is obtained by a

classical melting and quenching preparation in air followed by an adapted thermal treatment during which fluoride phases are crystallized. The size, size distribution, and volume concentration of fluoride crystallites are crucial for photonic applications. For example, to be a promising optical functional material, the size of the crystallites should be smaller than at least half of the wavelength of the light used while the size distribution should be narrow and the crystallites should possess a homogeneous spatial distribution. In this way, according to the scattering theory developed by Rayleigh [3], complete transparency of a light transmitting material can be attained [4]. A refractive index difference between the amorphous and crystalline phases of less than 0.1 is also required. However, according to Beall and Pinckney [5], based on Hopper's model, crystal sizes of 30 nm and differences in refractive index of 0.3 may be acceptable, provided that the crystal spacing is not larger than six times the average crystal size. Transparent Glass Ceramic (TGC) can also be

TABLE 1: Composition (mol%), fluorine content (Wt%), and characteristic temperatures (T_g , T_m , and crystallization temperatures of CaF_2 and $\text{Ca}_2\text{Al}_3\text{O}_6\text{F}$ in $^\circ\text{C}$) of the precursor glass samples.

Sample code	SiO_2	Al_2O_3	CaF_2	ErF_3	YbF_3	Fluorine content	T_g/T_m	CaF_2	$\text{Ca}_2\text{Al}_3\text{O}_6\text{F}$
SA1.8	45	25	35	—	—	11.5 ± 0.01	583/969	720	867
SA2.18	48	22	35	—	—	11.00 ± 0.01	570/984	705	861
SA1.8EY	45	25	35	0.5	2	12.4 ± 0.01	500, 605/1009	675	871
SA2.18EY	48	22	35	0.5	2	12.2 ± 0.01	461/1018	660	865

obtained with even larger crystal sizes if optical isotropy is achieved within the glass ceramic [6]. Consequently, the selection of the oxide glass composition and the fluoride phase composition is the key factor in obtaining the desired glass ceramic materials [7–9]. The Er^{3+} ions are specially interesting due to their emission at $1.5 \mu\text{m}$ and the green upconversion obtained under near infrared excitation [10–12]. In order to improve these emissions, the sensitization of this nanocomposite with Yb^{3+} ions may be a good choice because of the efficient energy transfer process from Yb^{3+} to Er^{3+} ions [10, 11].

Recently upconversion luminescence properties of $\text{Er}^{3+}/\text{Yb}^{3+}$ codoped glass ceramics containing CaF_2 nanocrystals were investigated by Chen et al. [11] and Kishi et al. [13]. In these researches the authors analyzed the infrared and the upconversion fluorescence produced by Er^{3+} and Yb^{3+} ions. In addition, Perez-Rodriguez et al. [14] studied the upconversion emission properties of Er^{3+} - Yb^{3+} codoped glass and glass ceramic samples with different Si/Al ratios were analyzed by covering their surfaces with silica microspheres ($3.8 \mu\text{m}$ diameter). However, it is necessary to analyze the effect of base glass composition on optical properties and crystallization mechanism of oxyfluoride glass ceramics in order to improve their optical properties.

In this paper, two series $\text{SiO}_2/\text{Al}_2\text{O}_3 = 2.18$ and $\text{SiO}_2/\text{Al}_2\text{O}_3 = 1.8$ of oxyfluoride glass ceramics containing CaF_2 nanocrystals doped with a fixed amount of Er^{3+} and Yb^{3+} (0.5 mol% ErF_3 and 2 mol% YbF_3) heat treated at four different temperatures (630, 660, 675, and 690°C) for 48 h were studied in order to improve Er^{3+} emissions. Based on emission spectra and luminescence lifetimes, the behavior of Er^{3+} and Yb^{3+} ions during heat treatment was evaluated.

2. Experimental

Reagent-Grade Chemicals. (opti pure), SiO_2 (Alfa-aesar-89709), Al_2O_3 (Alfa-aesar42571), CaF_2 (MERCCK 102840 precipitated pure), ErF_3 (Alfa-aesar 13653), and YbF_3 (Across 31616) were used as raw materials. The batch compositions were mixed in Agate mortar for 10 min in a glove box with the humidity of less than 10%.

The glass samples were prepared by melting the mixtures of the above mentioned materials in covered platinum crucibles at 1450°C in an electric kiln for 90 min. Four different batches were used in this study and they are coded in Table 1.

In order to measure fluorine loss in as-made glass, one gram (1.0000) sample of the glass is fused with 3 grams of sodium hydroxide in platinum crucible at 900°C for 60 min.

The fused cake is leached with hot water, filtered, and washed several times with hot water. The above solution is stirred for 3 hours at 80°C temperature. During this time the pH of the solution decreases to 7 by using sulfuric acid with concentration of 1 M. Using ion chromatography the fluorine concentrations of the solutions are calculated and the fluorine loss of the glass is measured subsequently (Table 1).

The prepared glass was annealed at 480°C (close to the glass transition temperatures) for 3 h. The resulting samples were cut and polished to form $30 \text{ mm} \times 30 \text{ mm} \times 2 \text{ mm}$ rectangular slices. Crystallization temperatures of glass were determined by differential thermal analysis (DTA; Polymer Laboratories 1640, Amherst, MA).

Glass frit with relatively coarse particle sizes (0.30–0.4 mm) and a heating rate of 10 K/min were used in each DTA run. This particle size was chosen in order to minimize the contribution of the surface area to the nucleation process and to obtain DTA results that were closer to the bulk glass. The reference material in these experiments was $\alpha\text{-Al}_2\text{O}_3$ powder.

The heat treatment of glass was carried out in an electric kiln at four different temperatures (630, 660, 675, and 690°C) for 48 h according to DTA results, at a heating rate of 10 K/min. The crystalline phases which were precipitated during the heat treatment were identified utilizing Philips X'Pert Pro diffractometer equipped with a primary monochromator, $\text{Cu K}\alpha$ radiation, and a X'Celerator detector. The XRD patterns were collected with a step of 0.016° in the 2θ angular range of 10° to 90° and acquisition time of 2 h. The microstructure of the heat treated samples was obtained by FESEM (Hitachi S4160) microscope. Samples were imaged after polishing (up to $1 \mu\text{m}$ diamond paste) and etching in a 0.5 volume percent HF solution for 5 min. Moreover, transmission electron microscopy observations were carried out by using TEM, Phillips CM 200, equipped with the EDAX DX4 EDX detector.

A passively tunable Ti:Sapphire laser source (Spectra-Physics 3900S) pumped by a Millennia spectra-physic laser (model 15SJSPPG) was used as an excitation source for upconversion luminescence. The upconverted light was recorded by a spectrometer (Ocean Optics HR4000) equipped with optical fiber with $200 \mu\text{m}$ diameter. In all the measurements the spectral resolution was about 0.5 nm.

The luminescence decay curves of the $^4\text{I}_{11/2}$ and $^4\text{S}_{3/2}$ levels were measured by exciting the sample with an optical parametric oscillator OPO (EKSPLA/NT342/3UVE) and were recorded and averaged using a digital storage oscilloscope (Tektronix 2430A).

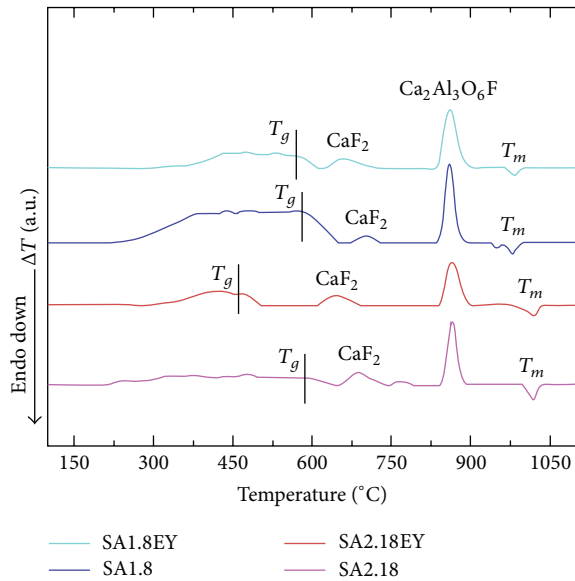


FIGURE 1: DTA thermographs of SA2.18, SA2.18EY, SA1.8, and SA1.8EY glass.

3. Results and Discussion

3.1. DTA Analysis. Figure 1 shows the DTA thermographs of the oxyfluoride glass specimens with the compositions shown in Table 1. The thermal event that arises at the lowest temperature is the glass transition temperature (T_g). As shown, it was followed by two exothermic effects showing the crystallizations of various phases. According to X-ray diffraction results, the first and the second exothermic peaks belong to crystallization of CaF_2 and $\text{Ca}_2\text{Al}_3\text{O}_6\text{F}$, respectively. As it can be seen, there is also an endothermic peak in the glass (T_m). XRD results showed that this peak was related to dissolution of fluorine in the residual glass phase. These characteristic temperatures of the glass, that is, T_g , crystallization temperatures, and T_m , have been summarized in Table 1.

According to Chen et al. [7, 15] and Bao et al. [8], Er^{3+} ion could play a significant role in the crystallization of CaF_2 in the oxyfluoride glass. In SA1.8EY, this temperature is reduced from 720°C to 675°C and in SA2.18EY from 705°C to 660°C with the incorporation of these ions.

Although influence of Yb^{3+} in the crystallization of CaF_2 in the oxyfluoride glass is not clear, there are some reports showing that the YbF_3 promotes the crystallization of the fluoride phases such as LaF_3 [16] or PbF_3 [17]. Further works in single doped samples with Yb^{3+} indicate that this ion does not act as nucleating agent for CaF_2 in $\text{SiO}_2\text{-Al}_2\text{O}_3\text{-CaF}_2$ system [18].

According to Hill et al. [19], in oxyfluoride glass, the fluorine was bonded to the aluminum ions which were present in the glass composition. As a result of this, there was less fluorine loss due to lower silicon tetrafluoride (SiF_4) formation [20]. It seems that a similar situation could happen in glass under study. As it can be seen from Table 1, increasing the alumina content resulted in the decrease of the fluorine loss during the melting. Owing to higher concentration of

the fluorine bond in the SA1.8 doped glass the dissolution of fluorine (T_m) takes place in a lower temperature than the other ratio (see Table 1).

3.2. Microstructural Evaluation. The SEM images (Figures 2(a) and 2(b)) of samples SA2.18EY and SA1.8EY after heat treatment at 590°C for 10 minutes with ramp rate of 10 K/min revealed that large separation areas (droplets) were formed in the SA1.8EY samples in comparison to the SA2.18EY samples. Phase separation in oxyfluoride glass ceramic is a common phenomenon [4, 21]. It is very likely that the described samples are phase separated; because rare earth ions are known to introduce phase separation droplets into the glass already in minor concentrations [18, 21].

According to DTA results, the crystallization of CaF_2 in the glass with higher alumina content and lower viscosity took place at higher temperatures than the other ones. Low viscosity promotes the occurrence of phase separation in glass, and, as a result of this, large separation areas (droplets) were formed in the SA1.8EY samples in comparison with the SA2.18EY samples. As the separated areas are smaller in the SA2.18EY specimens, the concentration of CaF_2 will be increased locally and the crystallization temperature of CaF_2 would be decreased more than the samples of the other ratio. Similar behavior was suggested in $\text{SiO}_2\text{-Al}_2\text{O}_3\text{-Na}_2\text{O-LaF}_3$ system by Bhattacharyya et al. [4].

A bright field and dark field transmission electron microscopy images of the glass ceramics SA1.8EY heat-treated at 675°C for 48 hours are shown in Figures 3(a) and 3(b), respectively. One can see in the bright field image the two phases of the glass ceramic: the black spots correspond to the crystallites in diffraction conditions and the white background corresponds to the glassy matrix. Lots of spherical CaF_2 crystallites sized about 20–60 nm are distributed separately among the glassy matrix. Their corresponding electron diffraction pattern is shown in the inset of Figure 3(a). The average size calculated by analyzing many TEM images is 35 ± 10 nm.

3.3. X-Ray Diffraction Analysis. Figures 4(a) and 4(b) show XRD patterns of SA1.8EY and SA2.18EY samples which were heat treated at 630, 660, 675, and 690°C for 48 h.

Several diffraction peaks corresponding to CaF_2 (ICCD no. 00-002-1302) crystals are clearly observed in the mentioned samples, indicating the crystallization of CaF_2 crystals in the precursor glass. The diameters of the crystals in the samples were evaluated by the Scherrer formula, and they are given in Figure 5. Due to the smaller size of precipitated CaF_2 crystals in the SA2.18EY samples than SA1.8EY, these samples maintained excellent transparency.

According to XRD patterns, the volume fraction of the crystal phase can be approximately estimated by the ratio of the integrated area of the peaks with respect to the total XRD patterns. All calculated data is plotted in Figure 5, and as seen the crystal size was risen with an increase in heat treatment temperature from 630 to 690°C (from 8.5 nm to 22 nm in SA2.18EY and from 20 nm to 34 nm SA1.8EY sample). As Chen et al. mentioned, the crystallization of CaF_2 in oxyfluoride glass ceramic is a diffusion-controlled process

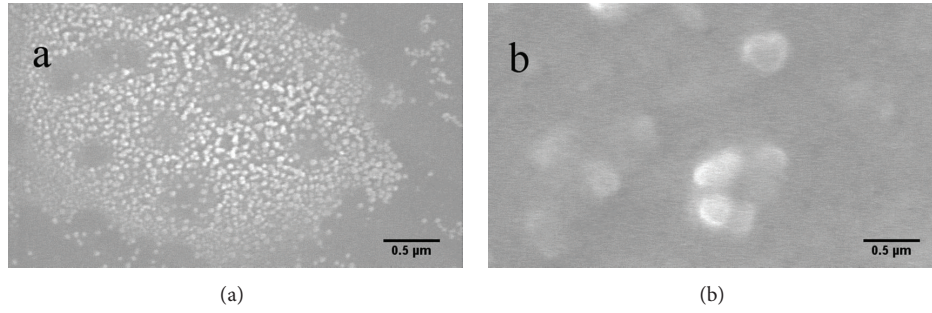


FIGURE 2: SEM images of samples (a) SA2.18 EY and (b) SA1.8 EY after heat treatment at 590°C for 10 min.

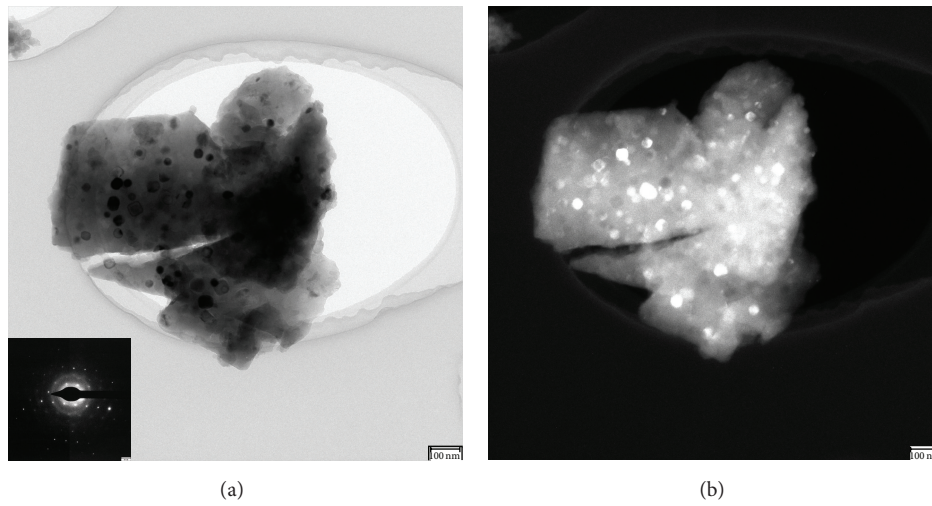


FIGURE 3: TEM images of (a) bright field and (b) dark field of the SA1.8EY sample heat treated at 675°C for 48 hours. The inset in (a) shows the corresponding electron diffraction pattern.

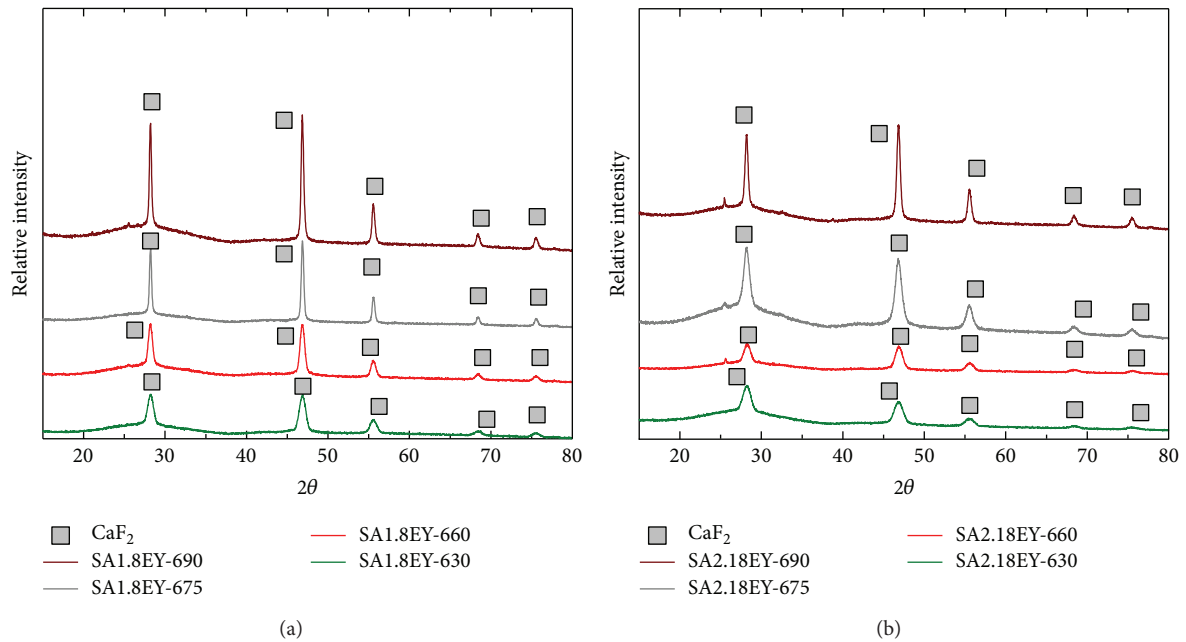


FIGURE 4: XRD patterns of (a) SA1.8EY and (b) SA2.18EY samples which were heat treated at 630, 660, 675, and 690°C for 48 hours.

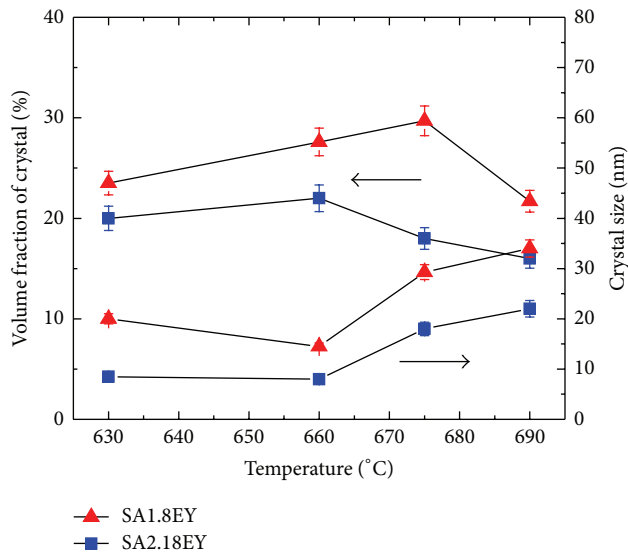


FIGURE 5: Crystal size and volume fraction of CaF_2 crystallites in SA1.8EY and SA2.18EY samples heat treated at different temperatures.

[7]. According to this mechanism, the local composition changes during crystallization, and the crystal growth rate depends exponentially on the heating temperature.

The volume concentration of crystalline CaF_2 in each ratio reaches a maximum and decreases afterward. This maximum is 22% for SA2.18EY at 660°C and 30% for SA1.8EY at 675°C. These two temperatures correspond to the maximum of CaF_2 crystallization temperature due to DTA results for each sample. At this temperature, the nucleation and growth of nucleus have the same rate as other temperatures. As a result, more nuclei were formed at the maximum of the crystallization peak, and volume concentration of CaF_2 was increased at this temperature as well. Russel [22] suggested a mechanism for the crystallization of CaF_2 in aluminosilicate glass, in which the interface is enriched in glass formers, increasing the viscosity near the crystals. Thus, a diffusional barrier around each crystal is formed, which hinders further crystal growth [22].

Although Russell did not mention the occurrence of phase separation in their glass, as mentioned before, our samples were phase separated. However, Russell studied different glass compositions located in the $\text{Na}_2\text{O}-\text{K}_2\text{O}-\text{CaO}-\text{CaF}_2-\text{Al}_2\text{O}_3-\text{SiO}_2$ system, and it is possible that their glass did not undergo phase separation.

Therefore, there are two parameters which could control the crystal size and size distribution, namely, the phase separated droplet size and the diffusional barrier around each crystal in phase separated droplet. These parameters are both controlled by the viscosity of glass.

Upon subsequent heat treatment, while the CaF_2 nanocrystals are formed within these phase separated droplets, SiO_2 , also contained in the phase separated droplets, is relocated to the periphery of the droplets, hence inhibiting further crystal growth [4, 22].

In SA2.18EY with lower alumina content, the viscosity of the glass is higher than the other one (SA1.8EY); hence the phase separated droplets are smaller. Additionally, due to the existence of higher viscosity, the diffusional barrier formed faster, and further nucleation became more and more difficult. Therefore, the size and concentration of crystalline CaF_2 are smaller than the other ratio.

3.4. Direct Excitation and Upconversion. Figure 6 shows the upconversion luminescence of samples which were heat treated at 630, 660, 675, and 690°C for 48 h and excited by 975 nm. The emission bands of the Er^{3+} ions can be assigned to the $^2\text{H}_{11/2} \rightarrow ^4\text{I}_{15/2}$ (520 nm), $^4\text{S}_{3/2} \rightarrow ^4\text{I}_{15/2}$ (545 nm), and $^4\text{F}_{9/2} \rightarrow ^4\text{I}_{15/2}$ (660 nm) transitions, respectively. As can be observed, in general the upconversion luminescence emission intensity increased with rising heat treatment temperature. Moreover, in these heat treated samples, the upconversion emission shows bands with well resolved structure, confirming again the incorporation of Er^{3+} ions into the nanocrystals. It is well known that the upconversion luminescence of rare earth ions is affected by multiphonon relaxation.

According to the Miyakawa and Dexter theory [23], the multiphonon decay rate depends exponentially on the energy gap to the next lower level and on the energy of the maximum lattice vibration of the surrounding host lattice [23]. The approximate frequency of the highest energy lattice vibration in silicate oxide glass is 1100 cm^{-1} , and this value decreases to 280 cm^{-1} for a CaF_2 crystal. As mentioned before, increasing the heat treatment time and temperature leads to incorporation of Er^{3+} ions into CaF_2 crystalline phase. Therefore, the upconversion intensity is increased significantly due to the decrease of the multiphonon relaxation with the increase of heat treatment time and temperature. For this reason, the upconversion emission obtained from the glass ceramic samples is much higher than the precursor glass (see Figure 6).

Moreover, comparing the results shown in Figure 6, it can be seen that the intensity of upconversion is higher in the SA2.18 than SA1.8 samples. This is due to the smaller crystal size of CaF_2 in this ratio. It seems that in the SA2.18EY matrix the distance between Er^{3+} and Yb^{3+} ions is shorter, and as result there is more energy transfer between them. Having more energy transfer processes between Er^{3+} and Yb^{3+} ions resulted in increasing the upconversion luminescence.

As Er^{3+} ions act as nucleate agents for CaF_2 crystals [7], during the heat treatment Er^{3+} ions are incorporated in the CaF_2 crystals at the beginning of the formation of the CaF_2 crystals. On the other hand, Yb^{3+} ions remain in the glass phase. As mentioned before, the crystal size was risen with increasing the heat treatment temperature. As a result, there are more Yb^{3+} ions near the surface of the crystals. According to phase diagram of the $\text{CaF}_2-\text{YbF}_3$ system [11], CaF_2 and YbF_3 yield a solid solution in the range of about 0–35 mol% YbF_3 content [11]. Therefore, the Yb^{3+} ions are considered to be incorporated into the CaF_2 to form $(\text{Ca}_{1-x}\text{Yb}_x)\text{F}_{2+x}$ solid-solution crystals during the heat treatment of the samples.

In Figure 7, the relative intensity of the green and red emission in upconversion (Figure 7) can be seen. In order to

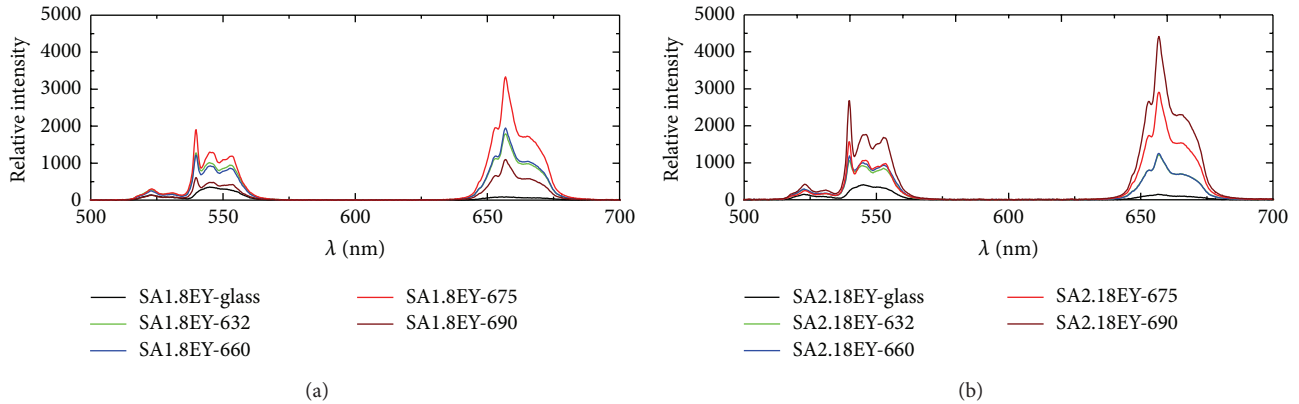


FIGURE 6: Upconversion luminescence in SA1.8EY and A2.18EY samples that obtained exciting at 975 nm which were heat treated at 630, 660, 675, and 690°C for 48 h.

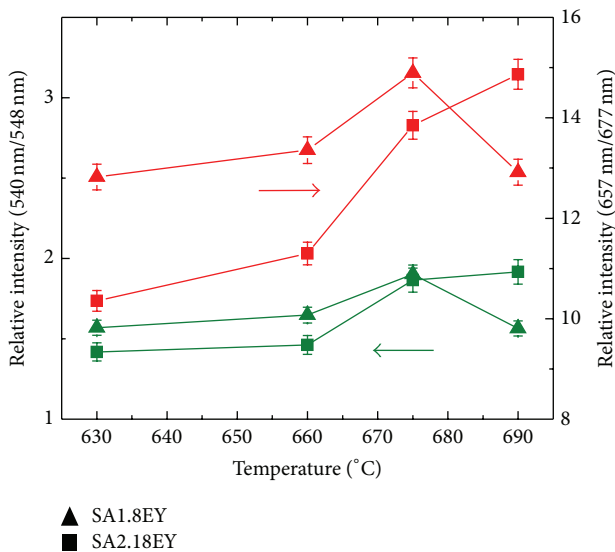


FIGURE 7: Relative intensity of the green (green symbols) and red (red symbols) upconversion bands that obtained exciting at 975 nm.

calculate this relative intensity, the wavelengths with highest (540 nm and 657 nm) and lowest (548 nm and 677 nm) intensity with respect to the glass intensity are chosen. These ratios will predominantly proportion the intensity of the emission coming from ions inside the nanocrystals with respect to the ions inside the glassy phase.

According to the results shown in Figure 7, increasing the temperature of the heat treatment leads to a rise in the red and green emissions in the upconversion luminescence of the samples in SA2.18EY ratio. On the other hand, in SA1.8EY ratio there is an increase in the relative red and green emissions until 675°C and the decrease after the heat treatment temperature reaches 690°C.

3.5. Fluorescence Decay Analysis. The fluorescence decays of Er^{3+} ions in the samples around 842 nm, which correspond to the $^4\text{S}_{3/2} \rightarrow ^4\text{I}_{13/2}$ transition, are shown in Figure 8.

These decays were obtained under pulse excitation of the $^4\text{S}_{3/2}$ level at 550 nm. In this figure, it can be seen that the lifetime of the Er^{3+} ions increases slightly with the heat treatment temperature in the SA1.8EY ratio. Probably, after crystallization of CaF_2 in the glass, the majority of Er^{3+} ions are incorporated in the CaF_2 crystals. As it was mentioned before, the multiphonon decay rate decreases in the ions inside the CaF_2 nanocrystals. As a result, the ions inside the nano-crystal have a longer lifetime. Further temperature increases to 690°C leading a rise in the Er^{3+} concentration in the CaF_2 crystals and thus improving the energy transfer between Er^{3+} ions. This then leads to most of the excited energy states going to the ground state by means of transfer to traps or cross-relaxation process, leading to the concentration quenching. Similar behavior was reported by Yan et al. in $\text{SrAl}_{12}\text{O}_{19}$ nanophosphors [24]. Therefore, the lifetime at 690°C is shorter than the other samples (Figure 8), and it could also explain the decreasing of the relative green and red emission intensity obtained in the Figure 7.

On the other hand, in SA2.18EY the lifetime of the Er^{3+} ions increased slightly with the heat treatment temperature. Due to high viscosity of the glass in this ratio, the ions have less mobility than the other ratio and as a result the greater part of the Er^{3+} ions remain in the glass phase. Raising the heat treatment temperature (675 and 690°C) leads to increasing the crystal size and the ion diffusion rate; therefore there is more possibility to have Er^{3+} ions inside or on the surface of the CaF_2 crystals. Considering this effect, there are more Er^{3+} ions in the fluoride phase and as a result the lifetime will be increased (see Figure 8). With respect to the other ratio (SA1.8), the concentration of the Er^{3+} ions is lower and these ions can be regarded as isolated and only a few of them with traps nearby can transfer their energy to the traps or undergo the cross-relaxation process, leading to an insignificant concentration quenching. In this case the green and red emission intensity will be increased (see Figure 7).

In order to identify the Yb^{3+} position (glass or crystal phase), the infrared fluorescence decays of the samples around 975 nm were also measured. These decays were obtained under pulse excitation of the $^2\text{F}_{5/2}$ level of Yb^{3+} ions

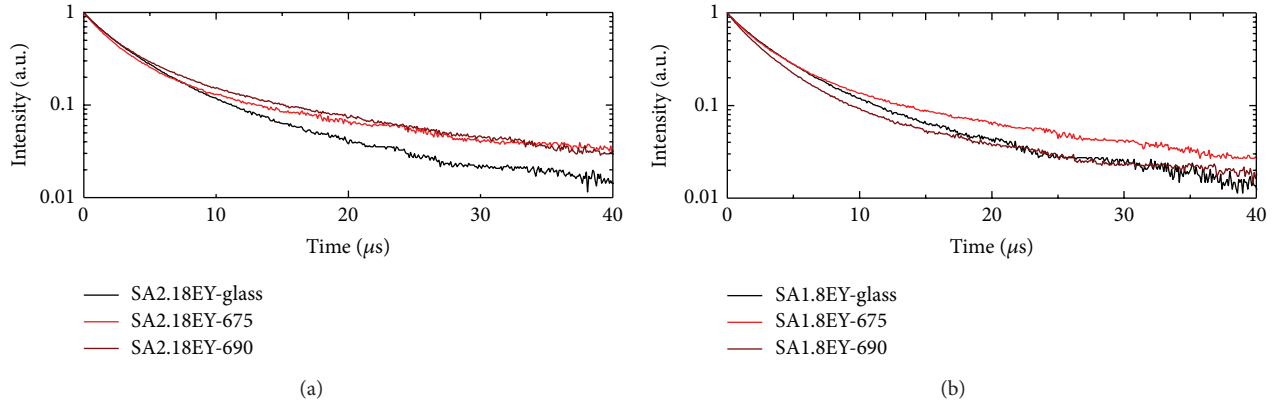


FIGURE 8: Fluorescence decays of Er^{3+} around 842 nm (corresponding to the ${}^4\text{S}_{3/2} \rightarrow {}^4\text{I}_{11/2}$ emission) obtained in SA1.8EY and SA2.18EY glass and in these samples heat treated at 675 and 690°C for 48 h and excited at 550 nm.

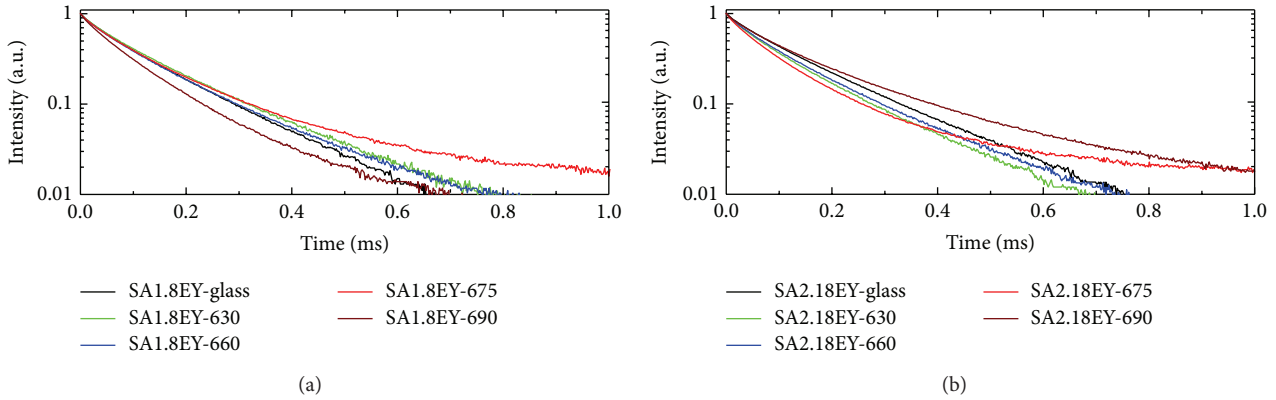


FIGURE 9: Infrared fluorescence decays of the glass around 975 nm in both ratios (SA1.8EY and SA2.18EY) samples which were heat treated at 630, 660, 675, and 690°C for 48 h and excited at 940 nm.

at 940 nm. At 975 nm the Er^{3+} ions have an excited level ${}^4\text{I}_{11/2}$ which coincides with the ${}^2\text{F}_{5/2}$ level of Yb^{3+} ions. Therefore, if transfer and back transfer processes between these ions are important it should be reflected in the experimental decays curves. As an example, in fluorindate glass these processes were analyzed on basis of the fluorescence transfer function model [10]. As it can be seen from Figure 9, the decay curves of the glass in both ratios indicate that the Yb^{3+} lifetimes are similar.

Comparing the decay curves of the glass and the samples which are heat treated at 630, 660, and 675°C in SA1.8EY and SA2.18EY ratio, it can be concluded that in the glass with higher alumina content (SA1.8EY) and low viscosity the Yb^{3+} ions start to be incorporated into fluoride phase while the heat treatment temperature is rising. Due to transfer and back transfer between Er^{3+} and Yb^{3+} ions inside the low energy phonon fluoride phase the decay time is increased in these samples (Figure 9).

On the other hand, in the glass with lower alumina content (SA2.18EY) and high viscosity, it seems that the majority of Yb^{3+} ions remain inside the glass phase. This can be explained by the diminution of their lifetimes, probably after

crystallization of CaF_2 in the glass; as the fluorine content of the glass was reduced, the lifetime of the ions inside the glass would be decreased due to the increase of energy phonon of the glass. As mentioned before rising the temperature to 675°C leads to increasing the size of the nanocrystals and as a result some Yb^{3+} ions are incorporated on the surface of the CaF_2 crystals in SA2.18EY. In this case there will be two groups of Yb^{3+} ions inside the sample, one located on the surface of the nanocrystals and the other one inside the glassy phase. The decay curve of SA2.18EY treated at 675°C which is shown in Figure 9 confirms this result. This curve consists of a short and a long component. The short component is due to the Yb^{3+} ions inside the glass while the long component is related to Yb^{3+} ions on the surface of the CaF_2 nanocrystals. Furthermore in SA1.8EY at 690°C there is a decrease in the lifetime which could be explained on a basis of the concentration quenching. As mentioned before the Er^{3+} concentration in the CaF_2 nanocrystals in this sample is high. Moreover, high concentrations of Yb^{3+} ions were expected in this ratio. As a result, transfer and back transfer among these ions could be very efficient until the energy is transferred to traps. According to this transfer, a decrease

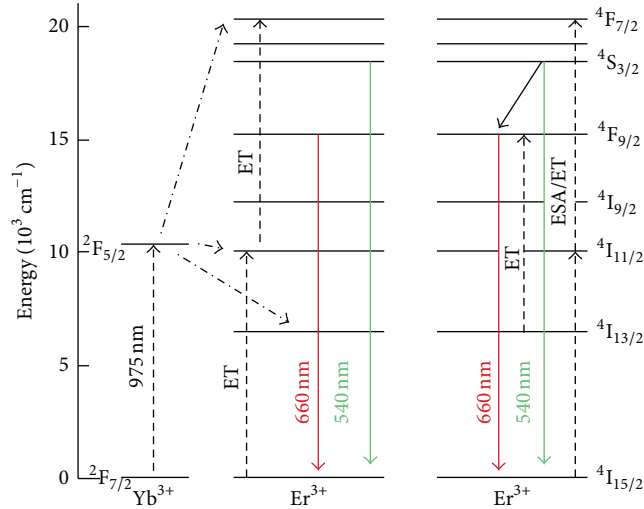


FIGURE 10: Energy-level diagram of Yb^{3+} and Er^{3+} ions and possible upconversion mechanisms.

in the lifetime is predictable for the SA1.8EY sample at this temperature (as shown in Figure 9).

All processes explained before give to place that the upconversion intensity of the SA2.18EY sample which is heat treated at 690°C for 48 hr should have the highest intensity among the others.

In Figure 10, different upconversion mechanisms to populate the $^4\text{S}_{3/2}$ and the $^4\text{F}_{9/2}$ emitting levels of Er^{3+} ions under excitation at 975 nm are shown. As it can be seen, the green emitting level ($^4\text{S}_{3/2}$) could be populated under excited state absorption (ESA) or energy transfer processes (ET) from the $^4\text{I}_{11/2}$ level. Moreover, the $^4\text{F}_{9/2}$ level could be populated from relaxation of the $^4\text{S}_{3/2}$ level or from an additional upconversion mechanism from the $^4\text{I}_{13/2}$ level. Additionally, Yb^{3+} ions in the composition introduce an additional possible mechanism to populate the $^4\text{F}_{9/2}$ level of the Er^{3+} ions. This will take place by an extra upconversion processes [25].

With the increase of Yb^{3+} doping content, the electron population of Er^{3+} ions in $^4\text{I}_{13/2}$ level is largely increased due to energy transfer from Yb^{3+} to Er^{3+} [7]. Besides, the excited Yb^{3+} ions can produce successive transfer processes in order to excite the Er^{3+} ions to the higher levels (as it is shown in Figure 10). As a result, the enhancement of the red emission will be achieved (as shown in Figure 6).

In Figure 11 the temporal evolution of the red emission under pulsed excitation at 975 nm is shown. In the glass samples the Er^{3+} and Yb^{3+} ions are placed far from each other in random positions of the glass matrix. As result, energy transfer processes between them are negligible. As it can be seen from Figure 11, the emission intensity coming from the ions inside the glass reaches the maximum, immediately after the pump laser. This is related to ESA mechanism which takes place in isolated Er^{3+} ions in the glass matrix in both ratios. As pointed out before, increasing the heat treatment temperature rises the Er^{3+} and Yb^{3+} concentration in the CaF_2

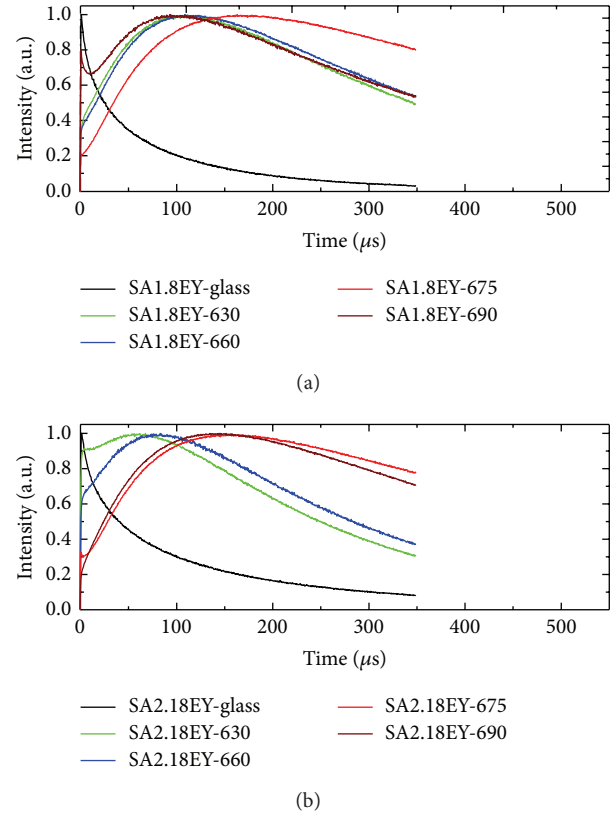


FIGURE 11: Temporal evolution of the upconversion emission at 660 nm with obtained exciting at 975 nm for SA1.8EY and SA2.18EY samples heat treated at 630, 660, 675, and 690°C for 48 h.

nanocrystals. Decreasing the distance between Er^{3+} ions in the CaF_2 nanocrystals lets additional ET mechanism to excite the $^4\text{F}_{9/2}$ level. In this case, the ESA is less important than ET mechanism, which is characterized by a rise in time (as it can be seen in some curves in Figure 11). Comparing the temporal curves of the glass heat treated at 630, 660, and 675°C in the two ratios, it can be concluded that in the SA1.8EY the ET mechanism is activated faster than the SA2.18EY. This is due to higher mobility of ions in this ratio, while in the other ratio the mobility of ions is lower and as a result there is an important difference in ion concentration inside the nanocrystals at different temperatures.

At 675 and 690°C the possibility of having Yb^{3+} ions in the CaF_2 nanocrystals increased. Therefore the ET mechanism will be more important in these temperatures as well.

In SA1.8EY, due to low viscosity of the glass, the ions have higher mobility than the other ratio and as a result the greater part of the Er^{3+} ions are incorporated into nanocrystals. Thus, at 690°C the concentration of both Yb^{3+} and Er^{3+} ions increased. Therefore, as it was obtained previously the quenching processes of the Er^{3+} ions in the nanocrystals produce an important reduction of the emission coming from these ions. As a result, the emission coming from ions excited by ESA mechanism will predominate again to populate the $^4\text{F}_{9/2}$ level.

4. Conclusions

The effects of alumina content and heat treatment on upconversion properties of codoped Er^{3+} and Yb^{3+} ions in oxyfluoride glass ceramics were investigated. Results showed that alumina content had a significant effect on phase separation and viscosity of the glass. Due to the high viscosity of low alumina content glass, the phase separated areas were smaller in these specimens. Although the crystallization of CaF_2 took place at lower temperature in this case, it will be frozen faster as well. Due to high viscosity of the glass in this ratio (SA2.18EY) ions have less mobility than the other ratio (SA1.8EY) and as a result the greater part of the Er^{3+} ions remain in the glass phase during the heat treatment process. Also Yb^{3+} ions start to be incorporated into CaF_2 nanocrystals at higher temperature in low alumina content glass (SA2.18EY). These conclusions have been obtained in basis of the analysis of the decay curves for the emission of Er^{3+} at 842 nm and the Yb^{3+} and Er^{3+} at 975 nm.

Conflict of Interests

The authors declare that there is no conflict of interests regarding the publication of this paper.

Acknowledgments

The authors thank Ministerio de Economía y Competitividad of Spain (MINECO) within The National Program of Materials (MAT2010-21270-C04-02/-03/-04), the Consolidar-Ingenio 2010 Program (MALTA CSD2007-0045, <http://www.malta-consolider.com>), the EU-FEDER for their financial support, and ACIISI of Gobierno de Canarias for the project ID20100152 and FPI. The authors also thank the Governments of Spain and India for the award of a Project within the Indo-Spanish Joint Programme of Cooperation in Science and Technology (PRI-PIBIN-2011-1153/DST-INT-Spain-P-38-11).

References

- [1] M. A. Hernández-Rodríguez, M. H. Imanieh, L. L. Martín, and I. R. Martín, "Experimental enhancement of the photocurrent in a solar cell using upconversion process in fluoroindate glasses exciting at 1480 nm," *Solar Energy Materials and Solar Cells*, vol. 116, pp. 171–175, 2013.
- [2] A. Tressaud, *Synthesis, Characterization & Properties of Nanostructured Solids*, vol. 1, John Wiley & Sons, Paris, France, 2010.
- [3] L. Rayleigh, "The incidence of light upon a transparent sphere of dimensions comparable with the wave-length," *Proceedings of the Royal Society of London Series A*, vol. 84, no. 567, pp. 25–46, 1910.
- [4] S. Bhattacharyya, T. Höche, N. Hemono, M. J. Pascual, and P. A. van Aken, "Nano-crystallization in $\text{LaF}_3\text{-Na}_2\text{O-Al}_2\text{O}_3\text{-SiO}_2$ glass," *Journal of Crystal Growth*, vol. 311, no. 18, pp. 4350–4355, 2009.
- [5] G. H. Beall and L. R. Pinckney, "Nanophase glass-ceramics," *Journal of the American Ceramic Society*, vol. 82, no. 1, pp. 5–16, 1999.
- [6] M. C. Gonçalves, L. F. Santos, and R. M. Almeida, "Rare-earth-doped transparent glass ceramics," *Comptes Rendus Chimie*, vol. 5, no. 12, pp. 845–854, 2002.
- [7] D. Chen, Y. Wang, Y. Yu et al., "Influences of Er^{3+} content on structure and upconversion emission of oxyfluoride glass ceramics containing CaF_2 nanocrystals," *Materials Chemistry and Physics*, vol. 95, no. 2-3, pp. 264–269, 2006.
- [8] F. Bao, Y. Wang, and Z. Hu, "Influence of Er^{3+} doping on microstructure of oxyfluoride glass-ceramics," *Materials Research Bulletin*, vol. 40, no. 10, pp. 1645–1653, 2005.
- [9] M. H. Imanieh et al., "Crystallization of nano calcium fluoride in $\text{CaF}_2\text{-Al}_2\text{O}_3\text{-SiO}_2$ system," *Solid State Sciences*, vol. 17, pp. 76–82, 2013.
- [10] I. R. Martín, V. D. Rodríguez, V. Lavín, and U. R. Rodríguez-Mendoza, "Transfer and back transfer processes in $\text{Yb}^{3+}\text{-Er}^{3+}$ codoped fluorindate glasses," *Journal of Applied Physics*, vol. 86, no. 2, pp. 935–939, 1999.
- [11] D. Chen, Y. Wang, E. Ma, Y. Yu, and F. Liu, "Partition, luminescence and energy transfer of $\text{Er}^{3+}/\text{Yb}^{3+}$ ions in oxyfluoride glass ceramic containing CaF_2 nano-crystals," *Optical Materials*, vol. 29, no. 12, pp. 1693–1699, 2007.
- [12] M. H. Imanieh et al., "Effect of alumina content and heat treatment on microstructure and upconversion emission of Er^{3+} ions in oxyfluoride glass-ceramics," *Journal of Rare Earths*, vol. 30, no. 12, pp. 1228–1234, 2012.
- [13] Y. Kishi, S. Tanabe, S. Tochino, and G. Pezzotti, "Fabrication and efficient infrared-to-visible upconversion in transparent glass ceramics of Er-Yb Co-doped CaF_2 nano-crystals," *Journal of the American Ceramic Society*, vol. 88, no. 12, pp. 3423–3426, 2005.
- [14] C. Perez-Rodríguez, M. H. Imanieh, L. L. Martín, S. Rios, I. R. Martín, and B. E. Yekta, "Study of the focusing effect of silica microspheres on the upconversion of $\text{Er}^{3+}\text{-Yb}^{3+}$ codoped glass ceramics," *Journal of Alloys and Compounds*, vol. 576, pp. 363–368, 2013.
- [15] D. Chen, Y. Wang, Y. Yu, and E. Ma, "Improvement of Er^{3+} emissions in oxyfluoride glass ceramic nano-composite by thermal treatment," *Journal of Solid State Chemistry*, vol. 179, no. 5, pp. 1445–1452, 2006.
- [16] D. Chen, Y. Wang, Y. Yu, and E. Ma, "Influence of Yb^{3+} content on microstructure and fluorescence of oxyfluoride glass ceramics containing LaF_3 nano-crystals," *Materials Chemistry and Physics*, vol. 101, no. 2-3, pp. 464–469, 2007.
- [17] G. Dantelle, M. Mortier, D. Vivien, and G. Patriarche, "Nucleation efficiency of erbium and ytterbium fluorides in transparent oxyfluoride glass-ceramics," *Journal of Materials Research*, vol. 20, no. 2, pp. 472–481, 2005.
- [18] M. H. Imanieh et al., "Improved cooperative emission in ytterbium-doped oxyfluoride glass-ceramics containing CaF_2 nanocrystals," *Journal of the American Ceramic Society*, vol. 95, no. 12, pp. 3827–3833, 2012.
- [19] R. Hill, D. Wood, and M. Thomas, "Trimethylsilylation analysis of the silicate structure of fluoro-alumino-silicate glasses and the structural role of fluorine," *Journal of Materials Science*, vol. 34, no. 8, pp. 1767–1774, 1999.
- [20] L. Lin, G. Ren, M. Chen, Y. Liu, and Q. Yang, "Study of fluorine losses and spectroscopic properties of Er^{3+} doped oxyfluoride silicate glasses and glass ceramics," *Optical Materials*, vol. 31, no. 10, pp. 1439–1442, 2009.
- [21] N. Hémono, G. Pierre, F. Muñoz, A. de Pablos-Martín, M. J. Pascual, and A. Durán, "Processing of transparent glass-ceramics by nanocrystallisation of LaF_3 ," *Journal of the European Ceramic Society*, vol. 29, no. 14, pp. 2915–2920, 2009.

- [22] C. Russel, "Nanocrystallization of CaF_2 from $\text{Na}_2\text{O}/\text{K}_2\text{O}/\text{CaO}/\text{CaF}_2/\text{Al}_2\text{O}_3/\text{SiO}_2$ glasses," *Chemistry of Materials*, vol. 17, no. 23, pp. 5843–5847, 2005.
- [23] T. Miyakawa and D. L. Dexter, "Phonon sidebands, multiphonon relaxation of excited states, and phonon-assisted energy transfer between ions in solids," *Physical Review B*, vol. 1, no. 7, pp. 2961–2969, 1970.
- [24] W. Yan, Y. Chen, and M. Yin, "Quenching mechanism of Er^{3+} emissions in Er^{3+} - and $\text{Er}^{3+}/\text{Yb}^{3+}$ -doped $\text{SrAl}_{12}\text{O}_{19}$ nanophosphors," *Journal of Rare Earths*, vol. 29, no. 3, pp. 202–206, 2011.
- [25] J. del-Castillo, A. C. Yanes, J. Méndez-Ramos, V. K. Tikhomirov, and V. D. Rodríguez, "Structure and up-conversion luminescence in sol-gel derived Er^{3+} - Yb^{3+} co-doped $\text{SiO}_2:\text{PbF}_2$ nanoglass-ceramics," *Optical Materials*, vol. 32, no. 1, pp. 104–107, 2009.

Research Article

Effect of Ag-Nanoparticles Doped in Polyvinyl Alcohol on the Structural and Optical Properties of PVA Films

Mahshad Ghanipour and Davoud Dorrnian

Laser Laboratory, Plasma Physics Research Center, Science and Research Branch, Islamic Azad University, Tehran, Iran

Correspondence should be addressed to Davoud Dorrnian; d.dorrnian@gmail.com

Received 30 September 2013; Revised 6 December 2013; Accepted 9 December 2013

Academic Editor: Amirianoosh Kiani

Copyright © 2013 M. Ghanipour and D. Dorrnian. This is an open access article distributed under the Creative Commons Attribution License, which permits unrestricted use, distribution, and reproduction in any medium, provided the original work is properly cited.

The effect of silver nanoparticles doped in PVA on the structural and optical properties of composite films is studied experimentally. Samples are PVA films of 0.14 mm thickness doped with different sizes and concentrations of silver nanoparticles. Structural properties are studied using X-ray diffraction and FTIR spectrum. Using the reflectance and transmittance of samples, the effect of doped nanoparticles and their concentration on optical parameters of PVA films include absorption coefficient, optical bandgap energy, complex refractive index, complex dielectric function, complex optical conductivity, and relaxation time is extracted and discussed. The dispersion of the refractive index of films in terms of the single oscillator Wemple-DiDomenico (WD) model is investigated and the dispersion parameters are calculated. Results show that by doping silver nanoparticles in PVA, number of Bragg's planes in the structure of polymer and its crystallinity are increased noticeably. Ag-O bonds are formed in the films and the bandgap energy of samples is decreased. Calculations based on WD model confirm that by doping nanoparticles, the anion strength of PVA as a dielectric medium is decreased.

1. Introduction

Metal nanoparticles combined polymers attracted great consideration because of the widened application goal offered by these hybrid materials [1–6]. It is well established that polymers, as dielectric materials, are excellent host matrices for encapsulation of metal nanoparticles like silver, gold, copper, and so forth, as they act both as reducing as well as capping agents and also provide environmental and chemical stability [7–9]. At the same time, these embedded nanoparticles inside the polymer matrix will also affect the properties of the host itself [1, 6, 10–13]. Particularly, polymer-metal hybrid such as polymer-Ag-nanoparticles composites is promising functional materials in several fields such as optical, electrical, thermal, mechanical, and antimicrobial properties [1, 14–18]. Many reports in the literature show attempts for synthesis of metal nanoparticles based polymer nanocomposites, with the possibility of variation in their optical and electrical properties for their application in high performance capacitors, conductive inks, and other electronic components [2, 19, 20]. For their application in

optoelectronic, electrical, and optical devices, biomedical science, sensors, and so forth, main key points are selection of polymer-metal nanoparticles combination, controlling the particles size, their concentration, and distribution within the polymer matrix [2, 21–23]. Special worthy has been reached to optical properties of the nanoparticles doped in polymer film, depending on the surrounding medium [24–26] and on their size, shape, and concentration [27–30]. Silver nanoparticles have received considerable attention due to their attractive physical and chemical properties [1] and it has been protected by polymers such as PVA, PVP, and PMMA. PVA could be considered as a good host material for metal due to its excellent thermostability, chemical resistance, high mechanical strength, water solubility, and moderate and dopant dependent electrical conductivity along with its consideration among the best polymers as host matrix for silver nanoparticles [1, 31]. PVA can effectively protect the nanoparticles from aggregation [1, 9].

In this paper, we focus on the structural and optical property variation of the supporting polymer due to silver nanoparticles doping. Silver nanoparticles were produced

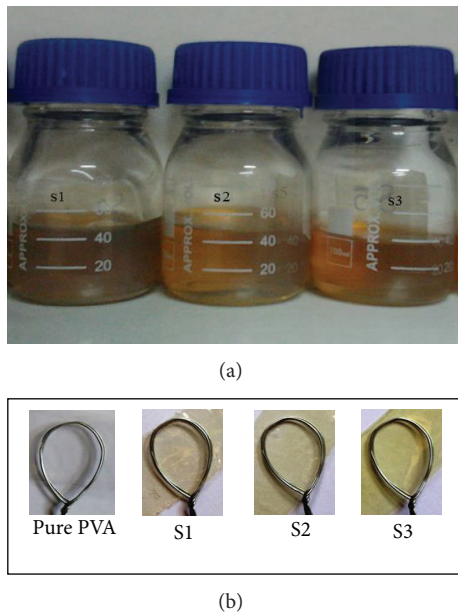


FIGURE 1: (a) Ag nanoparticle samples in distilled water and (b) pure PVA polymer film and Ag doped PVA films.

by laser ablation method. The laser ablation technique in a liquid produces proper metal nanoparticle samples to facilitate investigation of their photophysical and photochemical properties [32]. A remarkable and advantageous feature of nanoparticles prepared using this technique in contrast to those prepared using chemical synthesis is absence of uncontrolled byproducts [32, 33]. Interesting effects were observed on crystal structure and its optical properties. The noticeable main variations of optical properties of the host polymer come from surface plasmon resonance phenomena of nanoparticles dopant. The presence of silver nanoparticles embedded inside the polymer has been confirmed by the surface plasmon resonance response, which occurs at 400–420 nm for silver nanoparticles. The response transmittance, reflection, optical bandgap, dielectric constant, optical conductivity, dispersion refractive index, and dielectric relaxation time behavior of PVA-Ag nanoparticles films at room temperature with varying concentration of silver nanoparticles at the same thickness of silver nanoparticles doped PVA films are also investigated.

This paper is organized as follows: following the introduction in Section 1, experimental details are presented in Section 2. Section 3 is devoted to results and discussion, and Section 4 includes conclusion.

2. Experimental Details

Nanoparticles (NPs) were prepared by ablation of a high purity silver bulk in distilled water, using the fundamental harmonic of a Nd : YAG laser operating at 1064 nm with pulse width of 7 ns and 10 Hz repetition rate. Silver bulk was placed at the bottom of a water container with its surface at the focal point of a 80 mm convex lens. Height of water on the silver target was 12 mm. Laser beam diameter was 2 mm before the

lens and has been calculated to be $30\ \mu\text{m}$ on the surface of the target. The volume of the water in the ablation container was 20 mL and silver target was ablated with 500 laser pulses at different energies. Samples 1–3 were prepared with laser pulse fluencies of 1.5, 2, 3 J/cm^2 , respectively.

By weighting the dried target before and after ablation process the mass of ablated Ag nanoparticles were measured to be 3.7×10^{-4} , 4×10^{-4} , and 6.5×10^{-4} g for S1, S2, and S3, respectively.

PVA films were prepared by dissolving 1 g of PVA powder in 20 mL distilled water at 57°C . Mixture was stirred for two hours continuously to form a viscous solution. The PVA powder was provided by Merck Co., Germany. After completing desolation, 8 mL of silver nanoparticles suspension was added to the 20 mL aqueous PVA solution, and finally, samples was left to dry on a plane surface for 24 h at room temperature in close atmosphere to produce 3 samples of 0.14 mm thickness uniform silver nanoparticles doped PVA films. S1 to S3 are PVA films which are doped with samples 1 to 3 nanoparticles.

TEM micrographs were taken using CM120 system form PHILIPS Co. The X-ray diffraction (XRD) patterns of undoped and doped PVA films was measured employing STOE-XRD diffract meter with $\text{Cu-K}\alpha$ radiation ($\lambda = 1.544060\ \text{\AA}$). The Fourier transform infrared spectroscopy was done with NEXUS 870 FT-IR. The transmission and reflection spectrum of samples was recorded on a UV-Vis-NIR spectrophotometer from Varian Cary-500 Scan.

3. Results and Discussion

Nanoparticle samples and PVA doped Ag nanoparticle films are shown in Figures 1(a) and 1(b). PVA is colorless polymer and with adding Ag nanoparticles its color is changed to yellow. With increasing the concentration and decreasing the size of doped nanoparticles, color of films has become darker.

TEM images of nanoparticles are presented in Figure 2. In this set of images, the interbrain structure can be observed. Produced nanoparticles are spherical without any aggregation. The size distribution of nanoparticles can be observed in Figure 3. These graphs are plotted using the “measurement” software. We have wide range of size distribution of nanoparticles in each sample, but from samples 1 to 3 we can see that the peak of size distribution of samples is tended to smaller values. In this case the size of Ag dopants in S3 is minimum, while their concentration is maximum in comparison with S1 and S2. In contrast the size of Ag dopants in S1 is maximum, but their concentration is minimum. When the spot size and pulse width of the laser pulse are constant, increasing the laser fluence is due to increasing the laser pulse energy. If the fraction of the laser energy which is spent for ablation of nanoparticles assumed to be constant, increasing the pulse energy (photon numbers) leads to increasing the rate of ablation and increasing the pressure of the plasma plume which is formed on the surface of the target during the laser ablation process. The first phenomenon will increase the concentration of produced nanoparticles and the second phenomenon leads to decreasing the size of nanoparticles.

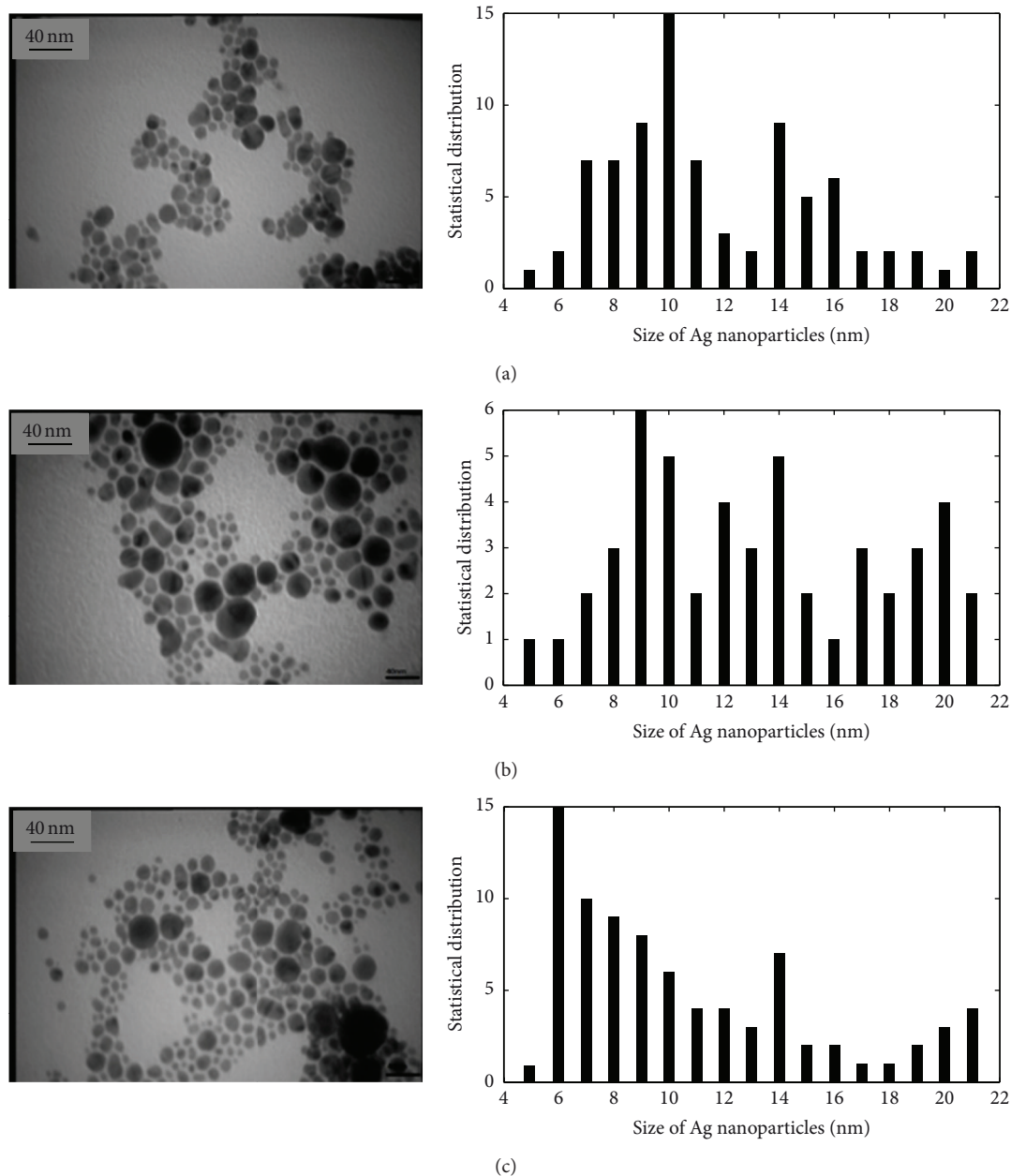


FIGURE 2: TEM image and size distribution of Ag nanoparticle generated in distilled water with laser ablation method. (a) S1, (b) S2, and (c) S3.

XRD spectrum of the Ag nanoparticles and pure PVA polymer films and PVA doped Ag nanoparticles are shown in Figures 3(a)–3(c). The diffraction pattern of undoped PVA indicates a diffraction bands at $2\theta = 13.88^\circ, 16.76^\circ, 25.4^\circ, 42.12^\circ,$ and 48.88° . It is well known that the peaks at $2\theta < 20^\circ$ are due to crystalline nature of PVA polymer molecules, which may be as a result of strong intermolecular and intramolecular hydrogen banding between the PVA chains [7, 34]. The peaks at angles larger than 20° may be due to impurities. The X-ray diffraction peaks of Ag nanoparticles occur at $2\theta = 38.15^\circ, 44.39^\circ, 64.74^\circ, 77.5^\circ,$ and 81.6° corresponding to reflections from the $\langle 111 \rangle, \langle 200 \rangle,$

$\langle 220 \rangle, \langle 311 \rangle$ and $\langle 222 \rangle$ planes of Ag, FCC lattice structure, respectively [35, 36]. All peaks observed in the sample of Ag nanoparticles have also been recreated in polymer films doped with silver nanoparticles. The peaks of polymer X-ray diffraction pattern at $2\theta > 20^\circ$ have been removed after doping. The peak at $2\theta = 42.12^\circ$ in pure PVA is observed to shift up by about 2.5° degree in PVA doped Ag nanoparticles. This shift might be due to changes in the d spacing values of the corresponding planes. The intensity of diffracted X-ray photons from films has been increased noticeably after the doping process. It may be due to two reasons. For $2\theta < 20^\circ$, increasing the peaks intensity is due to increasing the number

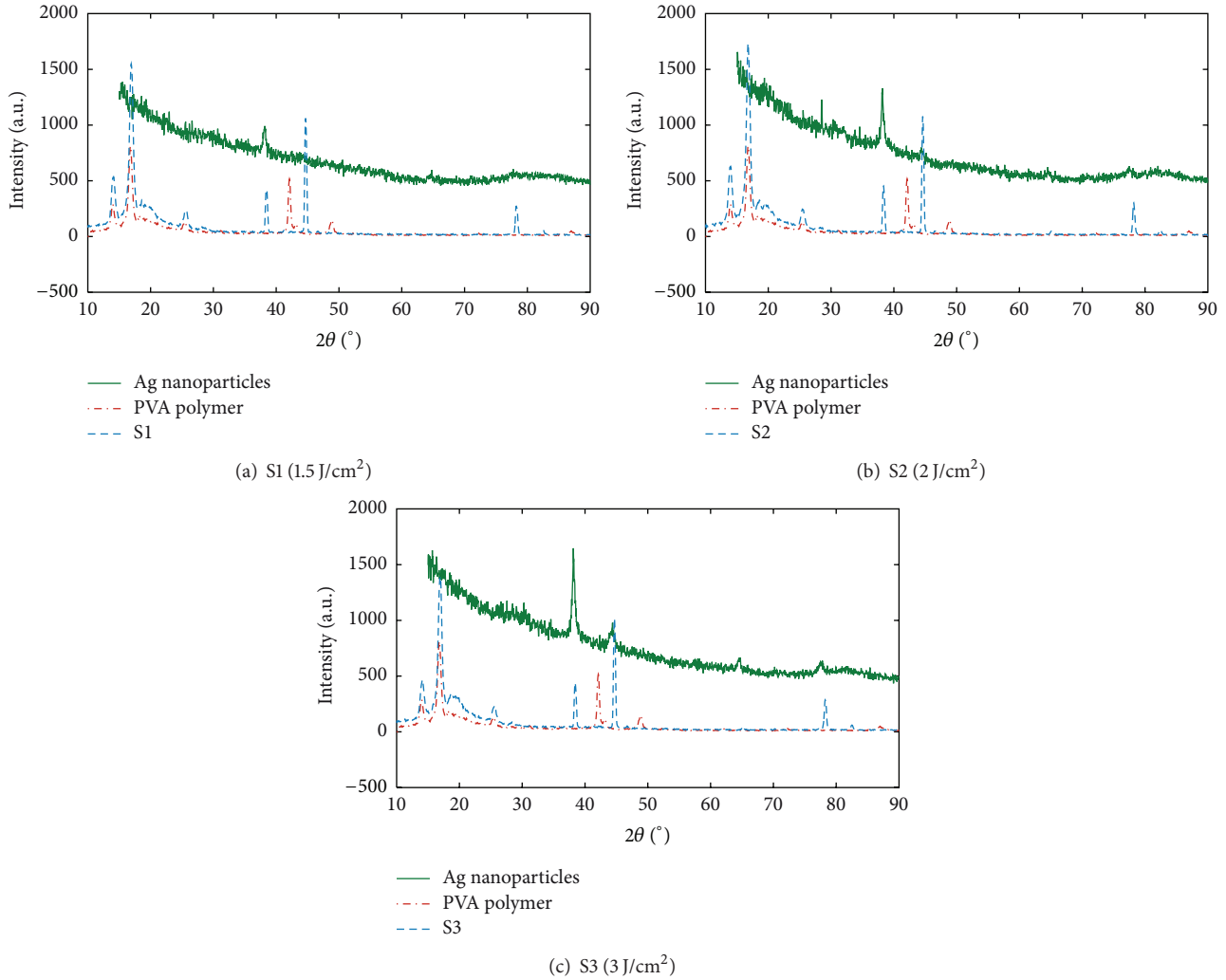


FIGURE 3: X-ray diffraction patterns of Ag nanoparticles, PVA polymer, and Ag nanoparticle doped PVA films; (a) S1, (b) S2, and (c) S3.

of PVA chains after Ag doping. Decreasing the intensity of peaks in FTIR spectrum confirms that after doping, number of PVA chains are increased in the structure of the films. Same results have been observed by Mahendia et al. and Gautam and Ram [7, 34]. For $2\theta > 20^\circ$, increasing the intensity of XRD peaks is due to increasing the number of crystallographic planes at certain angles.

The Fourier transform infrared spectroscopy (FTIR) spectra of pure PVA and doped films are shown in Figure 4. All spectra exhibit the characteristic absorption bands of pure PVA which are 3580 , 2974 , 1740 , 1570 , 1460 , and 845 cm^{-1} [37, 38]. It can be noticed that these treatments cause some observable changes in the spectral features of the samples in the range $1100\text{--}500\text{ cm}^{-1}$ (fingerprint region) apart from new absorption bands and slight changes in the intensities of some absorption bands. The new bands may be correlated likewise with defects induced by the charge transfer reaction between the polymer chain and the dopant. The vibrational peaks at 3580 , 2974 , 1740 , 1460 , and 845 cm^{-1} are assigned to O–H stretching, C–H stretching, C=O stretching, C–H

bend of CH_2 , and CH rocking of PVA, respectively [39, 40]. Further, the vibrational peaks found in the range $1130\text{--}650\text{ cm}^{-1}$ may be attributed to Ag–O, which indicate that silver nanoparticles doped in the PVA polymer matrix [37]. The experimental data given in Figure 4 indicate an increase in the vibrations of O–H, C–H, and C=O groups in the PVA matrix after adding Ag nanoparticles directly in the PVA film. Such changes in O–H, C–H, and C=O vibrations have been observed in other report [40]. After doping Ag, some polymers chains have been broken and some other chains have been formed instead. Increasing the FTIR spectrum in the range of $1400\text{ to }1600\text{ cm}^{-1}$ corresponds to C–H bond of CH_2 and shows the broken chains. Ag nanoparticles have generated new bonds in this range. Decreasing the FTIR spectrum in the range of $2500\text{ to }3700\text{ cm}^{-1}$ shows the produced polymer chains corresponds to O–H stretching and C–H stretching bonds.

The variation of transmittance (T) and reflectance (R) as a function of wavelength for pure PVA polymer film and samples 1 to 3 were recorded at room temperature and

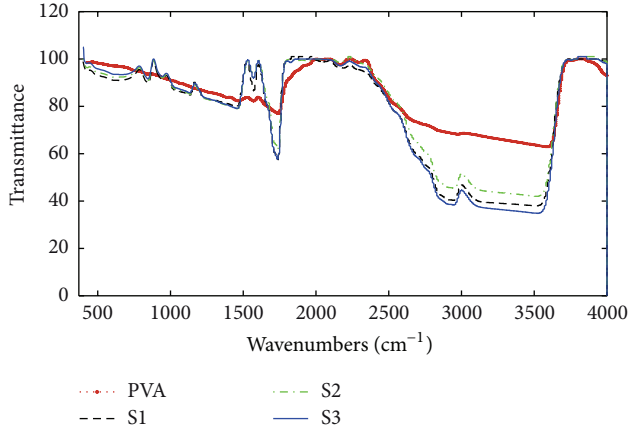


FIGURE 4: FTIR spectrum of PVA pure film and Ag nanoparticle doped in PVA polymer films.

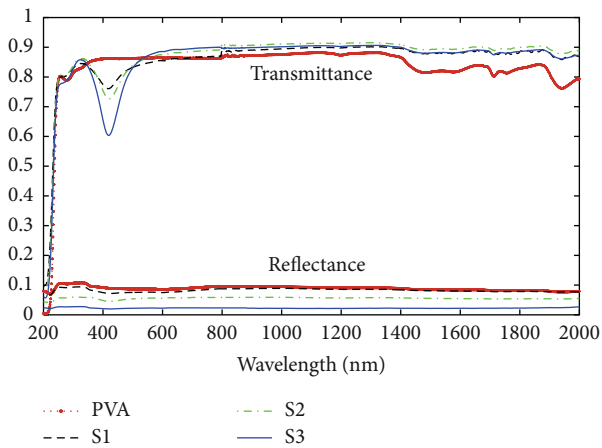


FIGURE 5: Optical transmittance and reflectance spectrum of samples.

are shown in Figure 5. Pure PVA is a colorless polymer without any noticeable absorption in the visible range. The sharp increase observed in transmittance spectrum in the range of 210 to 248 nm is due to the presence of the PVA polymer bandgap [1]. This figure clearly indicates that after adding nano-Ag in PVA polymer, a valley at 419 nm has been created, that its intensity continuously increasing with increasing concentration of the dopant. This new valley is attributed to the formation of charge transfer complexes [41]. The appearance of this valley in the visible region is due to the surface plasmon resonance (SPR) nature of the Ag nanoparticles embedded in PVA polymer dielectric medium.

After doping Ag nanoparticles in PVA polymer, the reflection, with increasing concentration of silver nanoparticles, due to local fluctuations charged particles, declined.

The optical absorption coefficients of samples are evaluated from the transmittance data using [42]

$$\alpha = \frac{1}{d} \ln \left[\frac{(1-R)^2}{2T} + \sqrt{\frac{(1-R)^4}{4T^2} + R^2} \right], \quad (1)$$

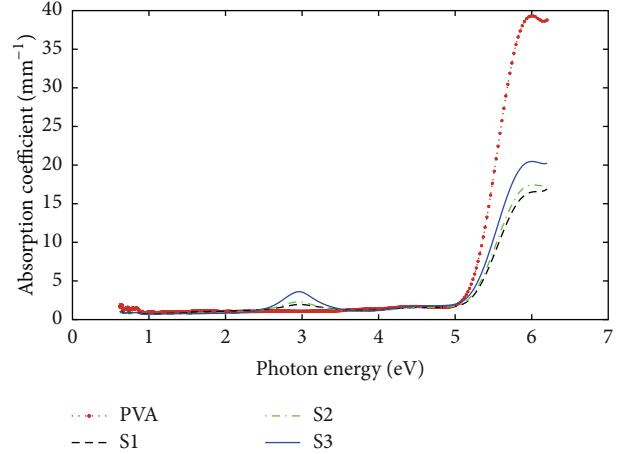


FIGURE 6: Optical absorption coefficient of films.

where T and R are the transmittance and reflection, respectively, α is the absorption coefficient, and d is the thickness of the films. Figure 6 presents the optical absorption coefficients for undoped and nano-Ag doped PVA films versus photon energies. The absorption peak at 2.95 eV for Ag nanoparticles doped in PVA polymer films represents the characteristic surface plasmon resonance dedicated to silver nanoparticles. The presence of nanoparticles in the polymer films could be conveniently followed by monitoring the plasmon absorption peaks in the absorption spectrum. The larger absorption peak appeared in UV range is due to the energy gap of the PVA polymer which decreases owing to increasing the concentration of Ag nanoparticles in the structure of the films. The position of the absorption edge was determined by extrapolating the linear part of α versus $h\nu$ curves to zero absorption value [41]. The band edge showed a decrease with increasing concentration of Ag nanoparticles in PVA matrix. The absorption edge shifts towards higher wavelength, indicating the decrease in the optical bandgap for the doped films. Shift of the absorption edge in the UV region is due to changes in the electron hole in the conduction and valence bands.

The most used method for estimation of the bandgap energy from optical measurement is the one proposed by Tauc and Grigorovici [43]. The optical bandgap energy of samples was deduced from the intercept of the extrapolated linear part of the plot of $(\alpha E)^{1/2}$ versus the photon energy E with abscissa (Figure 7). This follows by the method of Tauc where

$$\alpha E = B(E - E_g)^p. \quad (2)$$

In this equation, $\alpha(\omega)$ is the absorption coefficient, E is the photon energy, B is a factor that depends on transition probability and can be assumed to be constant within the optical frequency range, and the index p that is related to the distribution of the density of states is an index which assumes the values 1/2, 3/2, 2, and 3 depending on the nature of electronic transition. Taking $p = 2$, which corresponds to indirectly allowed transition in pure PVA film and nano-Ag doped PVA films, the bandgap energies of films were

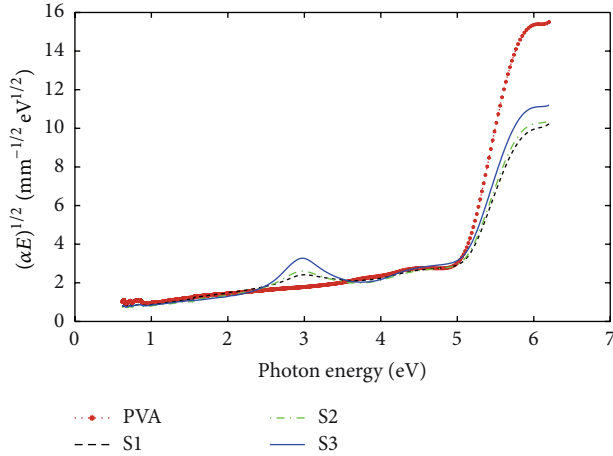


FIGURE 7: $(\alpha E)^{1/2}$ versus photon energy to illustrate Tauc method.

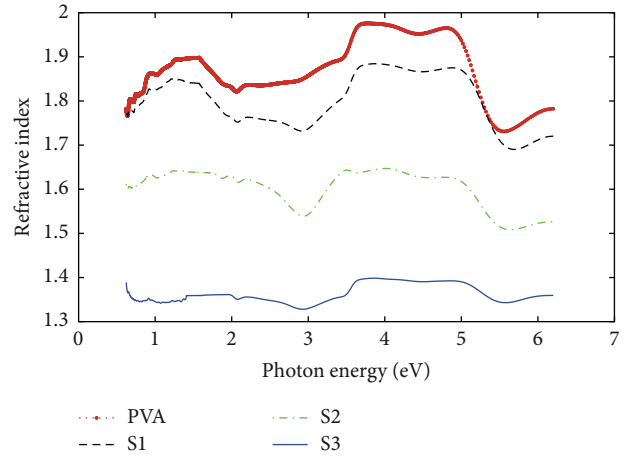


FIGURE 8: The refractive index of films.

calculated. In an indirect gap, a photon cannot be emitted because the electron must pass through an intermediate state and transfer momentum to the crystal lattice. The energy gap of pure PVA sample is equal to 4.96 eV, and with increasing the concentration of the Ag-nanoparticles in the structure of films, bandgap energy is decreased. The extracted bandgap energy of sample are 4.87, 4.84, and 4.78 eV, for sample, 1–3, respectively. The incorporation of the silver nanoparticles, irrespective of their methodology of synthesis, also affects the bandgap of the involved polymer system. This also confirms the presence of the inorganic fillers inside the host [1]. The variation of the calculated values of optical bandgap reflects the role of formation of Ag-nanoparticles in modifying the electronic structure of the PVA matrix [41, 44]. These Ag-nanoparticles may be responsible for the formation of localized electronic states in the Highest Occupied Molecular Orbital-Lowest Unoccupied Molecular Orbital (HOMO-LUMO) gap. These localized electronic states dominate the optical and electrical properties vis-à-vis their role as trapping and recombination centers, thus enhancing the low energy transitions leading to the observed change in optical bandgap. The decrease in the optical bandgap also reflects the increase in the degree of disorder in the films which arises due to the change in polymer structure [44, 45].

Optical properties, such as complex refractive index and dielectric constant for a certain range of wavelength between ultraviolet and near infrared, are important criteria for the selection of fabricated films for various applications. The refractive index is one of the fundamental properties of a material, because it is closely related to the electronic polarizability of ions and the local field inside the material [8, 9]. Thus, to further understand the interaction of Ag nanoparticles with PVA matrix, optical properties such as complex refractive index and dielectric constant have been calculated using the fundamental relations of photon transmittance (T), reflectance (R), and absorbance (A). The complex refractive index is $n = n + ik$, that n is the real part and the extinction

coefficient k is the imaginary part. The refractive index n of the films was calculated using the following equation [46]:

$$n = \left(\frac{1+R}{1-R} \right) + \sqrt{\frac{4R}{(1-R)^2} - k^2}, \quad (3)$$

in which $k = \lambda\alpha/4\pi$. Figures 8 and 9 show the photon energy dependence of refractive index and the extinction coefficient for pure PVA and nano-Ag doped PVA films. It can be discerned from Figure 8 that the refractive index of nano-Ag doped PVA films is lower than the refractive index of pure PVA and it decreases with increasing concentration of Ag nanoparticles in PVA matrix. This property is inherent in all conductors and due to localized fluctuation of charged particles in medium. Also decreasing the value of refractive index may be an indication of low density of films, which leads to increasing the interatomic spacing [45]. This is due to formation of intermolecular hydrogen bonding between Ag-nanoparticles and the adjacent OH groups. The dependence of the refractive index on the film density can be discussed by the well-known Clausius-Mossotti relation [46].

The extinction coefficient k describes the properties of the material with respect to light of a given wavelength and indicates the absorption changes when the electromagnetic wave propagates through the material. In Figure 9, the extinction coefficient k of the doped samples have a peak at $E = 2.95$ eV, which increases with increasing concentration of Ag nanoparticles in PVA dielectric medium. The extinction coefficient k increases due to surface plasmon absorption in doped samples, while the refractive index decreases in this region. There is anomalous dispersion regions when $2.25 < E < 2.95$ eV and $E > 4.85$ eV, as well as normal dispersion when $2.95 < E < 3.45$ eV for doped samples.

The complex dielectric function is $\varepsilon = \varepsilon_r + \varepsilon_i$, where ε_r is the real part and ε_i is the imaginary part of dielectric constant. The real and imaginary parts of dielectric constant are expressed as

$$\begin{aligned} \varepsilon_r &= n^2 - k^2, \\ \varepsilon_i &= 2nk. \end{aligned} \quad (4)$$

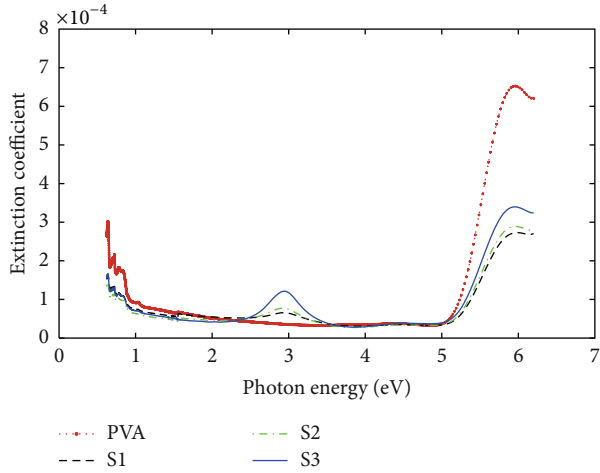


FIGURE 9: The extinction coefficient spectrum of films.

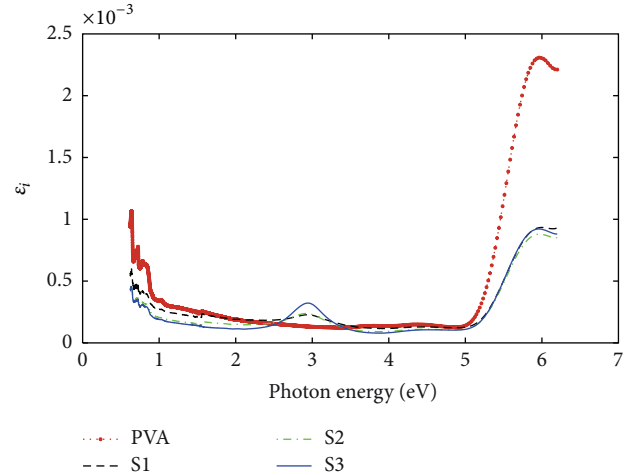


FIGURE 11: Imaginary part of the dielectric function of films.

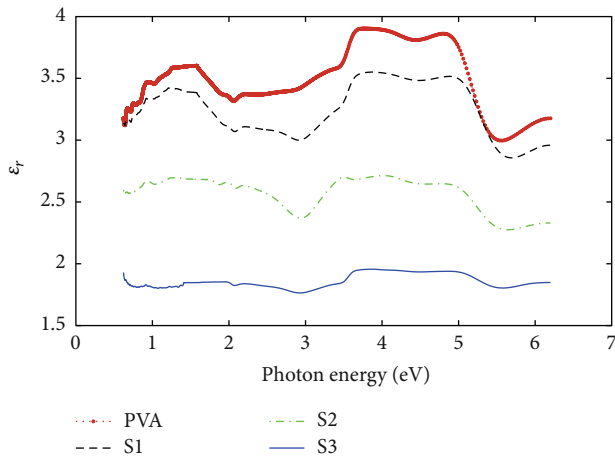


FIGURE 10: Real part of the dielectric constant of pure PVA and Ag nanoparticle doped films.

The real part of dielectric constant is related to the dispersion. In order to explain the dispersion it is necessary to take into account the actual motion of the electrons in the optical medium through which the light is traveling. The imaginary part represents the dissipative rate of electromagnetic wave propagation in the medium. The real and imaginary parts dependences on photon energy of samples are shown in Figures 10 and 11, respectively. It can be concluded that ϵ_r is larger than ϵ_i because it mainly depends on n^2 . With increasing the amount of silver nanoparticles in PVA, the real part of dielectric constant is decreased. It is due to decrease of the dielectric property of films because of Ag nanoparticles metal lattice in the host PVA polymer matrix. The normal dispersion is associated with an increase in $\text{Re}(\epsilon)$ with ω , and anomalous dispersion is associated with the reverse mechanism. Normal dispersion is occurred everywhere expect in the neighborhood of the resonance frequency. In this region the anomalous dispersion is appreciable. Since a positive imaginary part to ϵ_i represents dissipation of energy from the electromagnetic wave into the medium, the regions where ϵ_i

is large are called regions of resonant absorption [47]. The peak that appears in Figure 11 at $E = 2.95$ eV shows the plasmonic absorption.

The complex dielectric function and complex optical conductivity are introduced through Maxwell's equations. The interband transitions have threshold energy at the energy gap. That is, we expect the frequency dependence of the real part of the conductivity $\sigma_r(\omega)$ due to an interband transition to exhibit a threshold for an allowed electronic transition [48]. In interband transition, real σ_r and imaginary σ_i components of optical conductivity are described as [48–50]

$$\begin{aligned}\sigma_r &= \omega \epsilon_i \epsilon_0, \\ \sigma_i &= \omega \epsilon_r \epsilon_0,\end{aligned}\quad (5)$$

where ω is the angular frequency of electromagnetic wave and ϵ_0 is the free space dielectric constant. The real and imaginary parts of the optical conductivity dependence on the photon energy are shown in Figures 12 and 13, respectively.

The real optical conductivity in bandgap energy region after doping the Ag-nanoparticles in PVA polymer decreases. It can be due to the segregation effect [41, 51]. The segregated effect is the dispersion of metallic particles restricted by the presence of much larger polymeric particles. The observed effect of Ag nanoparticles on the optical conductivity and conduction behavior of PVA films can be explained on the basis of charge transfer complex formation involving PVA molecules and the dopant. When PVA polymer is mixed with Ag nanoparticles, as a result, the filler is pushed into interstitial space between the polymer particles and forms a segregated network [51]. At higher dopant concentration, there may be segregation of the dopant in the polymer matrix which decreases the conductivity. Thus motion of charge carriers or localized fluctuations of charged particles in molecular aggregates impedes optical conductivity. Moreover, there is a weak peak at $E = 2.95$ eV that can be seen only in the doped samples. This new peak is attributed to the formation of charge transfer or the surface plasmon

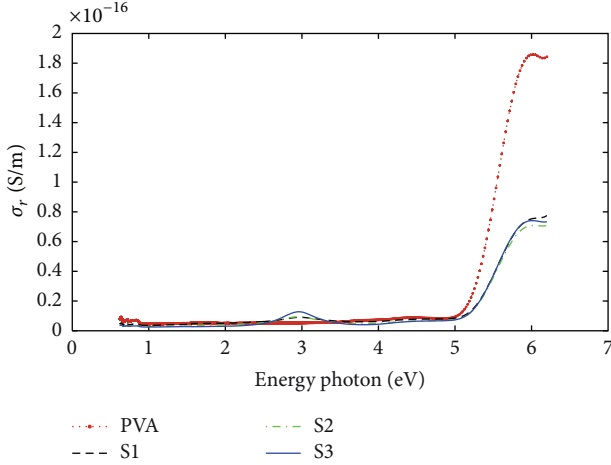


FIGURE 12: Real part of the optical conductivity of pure PVA and doped films.

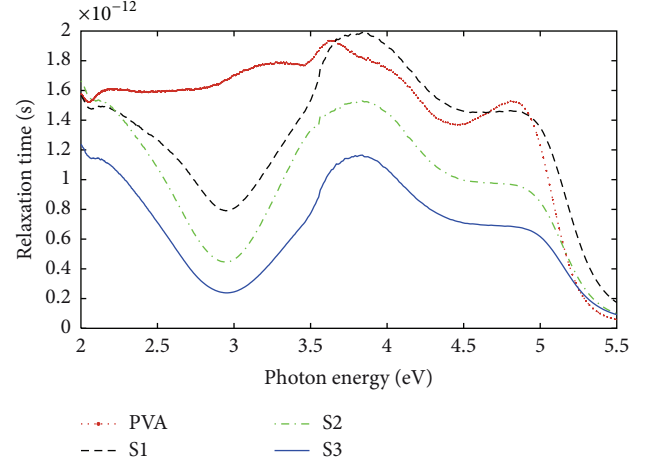


FIGURE 14: Relaxation time versus photon energy of films.

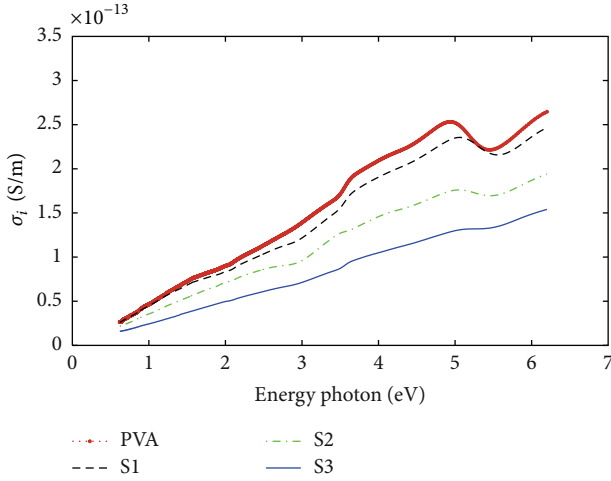


FIGURE 13: Imaginary part of the optical conductivity of pure PVA and doped films.

silver nanoparticles. Another result is that by increasing the concentration of Ag nanoparticles in PVA matrix, the imaginary part of optical conductivity decreases.

A dielectric sample in an external electric field acquires a nonzero macroscopic dipole moment indicating that the dielectric is polarized under the influence of the field. Polarization of dielectric material achieves its equilibrium value, not instantaneously but rather over a period of time τ [52]. The dielectric relaxation time τ can be evaluated using

$$\tau = \frac{\epsilon_{\infty} - \epsilon_r}{\omega \epsilon_i}. \quad (6)$$

Figure 14 shows the dielectric relaxation time as a function of photon energy for pure PVA polymer and Ag nanoparticle doped PVA films. The valley at 2.95 eV for doped samples increases with increasing the concentration of Ag nanoparticles in the structure of the films. In other words the relaxation time of dipole orientation decreases.

This is another reason for decreasing the dielectric function and increasing the conductivity of films with increasing the concentration of nanoparticles in their structure [53].

Refractive index dispersion is a determinant factor in optical materials. It is a significant factor in optical communication and in designing devices for spectral dispersion [35]. In the normal dispersion region, the refractive index dispersion has been analyzed using the single oscillator model developed by theory of Wemple and DiDomenico [54]. They introduced a dispersion-energy parameter E_d , which connects the coordination number and the charge distribution within each unit cell. E_d is closely related to chemical bonding. Also they defined a single oscillator parameter E_0 , which is proportional to the energy of oscillator. In terms of this dispersion energy E_d and single oscillator energy E_0 , the refractive index n at frequency can be written as

$$\frac{1}{n^2 - 1} = \frac{E_0}{E_d} - \frac{1}{E_0 E_d} (h\nu)^2. \quad (7)$$

The values of E_d and E_0 can be obtained from the intercept and slope of the linear part of $(n^2 - 1)^{-1}$ plot versus $(h\nu)^2$ as is shown in Figure 15. Also, dispersion of refractive index is controlled by the combined effects of E_d and E_0 . The calculated values of the dispersion parameters (E_0 and E_d) as well as the corresponding optical constant ($\epsilon = n^2$) for the pure PVA film and samples 1 to 3 are listed in Table 1. The dispersion energy values decreases with increasing the concentration of Ag nanoparticles in PVA films, because the anion strength of the dielectric medium has been declined. Therefore, the PVA polymer host is less willing to keep the electrons in their outer layers. The single oscillator energy is an average energy gap as pointed out in many references [50]. The E_0 value of the films is related empirically to the lowest indirect bandgap by $E_0 \approx 1.03E_g$. This relation is in good agreement with the single oscillator model.

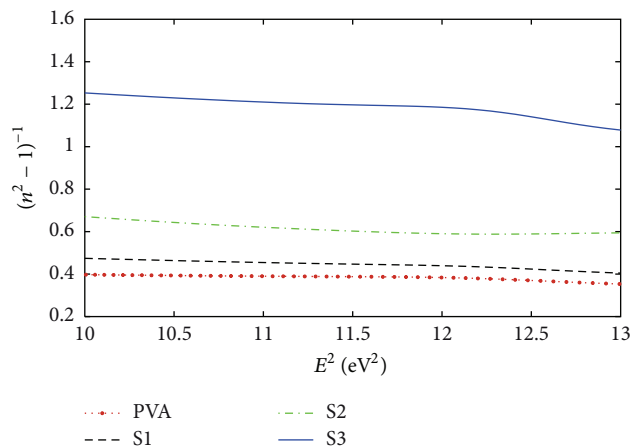


FIGURE 15: Plot of $(n^2 - 1)$ versus squared photon energy of pure PVA and doping samples.

TABLE I: Dispersion parameters of films.

Samples	n	ϵ	E_0	E_d
PVA	1.56	2.44	5.19	7.49
S1	1.48	2.19	5.04	6.03
S2	1.37	1.89	4.97	4.46
S3	1.19	1.42	4.87	2.05

4. Conclusions

Preparation of silver nanoparticles by laser ablation method at different fluencies of laser pulse in pure water is investigated. The TEM analysis revealed that generated nanoparticles in this experimental condition are almost spherical and their average size was 6–12 nm and with increasing the laser pulse fluence, the size of nanoparticles is decreased. The X-ray diffraction spectrum reveals that the number of crystallographic planes at certain angles is increased after doping Ag nanoparticles in the structure of PVA. FTIR spectrum peaks correspond to molecular vibrations and chemical bonds, indicate the presence of silver in the PVA polymer structure. The optical bandgap energy of the samples is decreased with increasing the concentrations of silver nanoparticles. Refractive index and dielectric constant are decreased with increasing the concentration of Ag nanoparticles. Increase of dopant concentration resulted in a decrease in real part of the optical conductivity because of segregation effect. The refractive index and consequently the related dispersion parameters of PVA and doped PVA have been determined and explained using the Wemple-DiDomenico model.

References

- [1] A. Nimrodh Ananth and S. Umapathy, "On the optical and thermal properties of in situ/ex situ reduced Ag NPs/PVA composites and its role as a simple SPR-based protein sensor," *Applied Nanoscience*, vol. 1, no. 2, pp. 87–96, 2011.
- [2] G. Neshet, G. Marom, and D. Avnir, "Metal-polymer composites: synthesis and characterization of polyaniline and other polymer at Silver compositions," *Chemistry of Materials*, vol. 20, no. 13, pp. 4425–4432, 2008.
- [3] P.-H. Wang, Y.-Z. Wu, and Q.-R. Zhu, "Polymer-metal composite particles: polymer core and metal shell," *Journal of Materials Science Letters*, vol. 21, no. 23, pp. 1825–1828, 2002.
- [4] S. Clémenson, P. Alcouffe, L. David, and E. Espuche, "Structure and morphology of membranes prepared from polyvinyl alcohol and silver nitrate: influence of the annealing treatment and of the film thickness," *Desalination*, vol. 200, no. 1-3, pp. 437–439, 2006.
- [5] K. Akamatsu, S. Takei, M. Mizuhata et al., "Preparation and characterization of polymer thin films containing silver and silver sulfide nanoparticles," *Thin Solid Films*, vol. 359, no. 1, pp. 55–60, 2000.
- [6] R. Zeng, M. Z. Rong, M. Q. Zhang, H. C. Liang, and H. M. Zeng, "Laser ablation of polymer-based silver nanocomposites," *Applied Surface Science*, vol. 187, no. 3-4, pp. 239–247, 2002.
- [7] S. Mahendia, A. K. Tomar, and S. Kumar, "Electrical conductivity and dielectric spectroscopic studies of PVA-Ag nanocomposite films," *Journal of Alloys and Compounds*, vol. 508, no. 2, pp. 406–411, 2010.
- [8] N. Singh and P. K. Khanna, "In situ synthesis of silver nanoparticles in polymethylmethacrylate," *Materials Chemistry and Physics*, vol. 104, no. 2-3, pp. 367–372, 2007.
- [9] P. K. Khanna, R. Gokhale, V. V. V. S. Subbarao, A. K. Vishwanath, B. K. Das, and C. V. V. Satyanarayana, "PVA stabilized gold nanoparticles by use of unexplored albeit conventional reducing agent," *Materials Chemistry and Physics*, vol. 92, no. 1, pp. 229–233, 2005.
- [10] K. Akamatsu, S. Takei, M. Mizuhata et al., "Preparation and characterization of polymer thin films containing silver and silver sulfide nanoparticles," *Thin Solid Films*, vol. 359, no. 1, pp. 55–60, 2000.
- [11] I. Hussain, M. Brust, A. J. Papworth, and A. I. Cooper, "Preparation of acrylate-stabilized gold and silver hydrosols and gold-polymer composite films," *Langmuir*, vol. 19, no. 11, pp. 4831–4835, 2003.
- [12] S. A. Zavyalov, A. N. Pivkina, and J. Schoonman, "Formation and characterization of metal-polymer nanostructured composites," *Solid State Ionics*, vol. 147, no. 3-4, pp. 415–419, 2002.
- [13] J. Lee, D. Bhattacharyya, A. J. Easteal, and J. B. Metson, "Properties of nano-ZnO/poly(vinyl alcohol)/poly(ethylene oxide) composite thin films," *Current Applied Physics*, vol. 8, no. 1, pp. 42–47, 2008.
- [14] Z. Zhong, D. Wang, Y. Cui, M. W. Bockrath, and C. H. Lieber, "Nanowire crossbar arrays as address decoders for integrated nanosystems," *Science*, vol. 302, no. 5649, pp. 1377–1379, 2003.
- [15] D. S. Hopkins, D. Pekker, P. M. Goldbart, and A. Bezryadin, "Quantum interference device made by DNA templating of superconducting nanowires," *Science*, vol. 308, no. 5729, pp. 1762–1765, 2005.
- [16] S. Clémenson, D. Léonard, D. Sage, L. David, and E. Espuche, "Metal nanocomposite films prepared in situ from PVA and silver nitrate. Study of the nanostructuring process and morphology as a function of the in situ routes," *Journal of Polymer Science A*, vol. 46, no. 6, pp. 2062–2071, 2008.
- [17] M. K. Temgire and S. S. Joshi, "Optical and structural studies of silver nanoparticles," *Radiation Physics and Chemistry*, vol. 71, no. 5, pp. 1039–1044, 2004.
- [18] M. Zheng, M. Gu, Y. Jin, and G. Jin, "Optical properties of silver-dispersed PVP thin film," *Materials Research Bulletin*, vol. 36, no. 5-6, pp. 853–859, 2001.

- [19] O. L. A. Monti, J. T. Fourkas, and D. J. Nesbitt, "Diffraction-limited photogeneration and characterization of silver nanoparticles," *Journal of Physical Chemistry B*, vol. 108, no. 5, pp. 1604–1612, 2004.
- [20] K. L. Kelly, E. Coronado, L. L. Zhao, and G. C. Schatz, "The optical properties of metal nanoparticles: the influence of size, shape, and dielectric environment," *Journal of Physical Chemistry B*, vol. 107, no. 3, pp. 668–677, 2003.
- [21] H. Weickmann, J. C. Tiller, R. Thomann, and R. Mülhaupt, "Metallized organoclays as new intermediates for aqueous nano-hybrid dispersions, nano-hybrid catalysts and antimicrobial polymer hybrid nanocomposites," *Macromolecular Materials and Engineering*, vol. 290, no. 9, pp. 875–883, 2005.
- [22] U. Keirbeg and M. Vollmer, *Optical Properties of Metal Clusters*, vol. 25 of *Springer Series in Material Science*, 1995.
- [23] S. Chen and J. M. Sommers, "Alkanethiolate-protected copper nanoparticles: spectroscopy, electrochemistry, and solid-state morphological evolution," *Journal of Physical Chemistry B*, vol. 105, no. 37, pp. 8816–8820, 2001.
- [24] A. A. Scalisi, G. Compagnini, L. D'Urso, and O. Puglisi, "Non-linear optical activity in Ag-SiO₂ nanocomposite thin films with different silver concentration," *Applied Surface Science*, vol. 226, no. 1–3, pp. 237–241, 2004.
- [25] G. Yang, W. Wang, Y. Zhou, H. Lu, G. Yang, and Z. Chen, "Linear and nonlinear optical properties of Ag nanocluster/BaTiO₃ composite films," *Applied Physics Letters*, vol. 81, no. 21, pp. 3969–3971, 2002.
- [26] H. B. Liao, R. F. Xiao, H. Wang, K. S. Wong, and G. K. L. Wong, "Large third-order optical nonlinearity in Au:TiO₂ composite films measured on a femtosecond time scale," *Applied Physics Letters*, vol. 72, no. 15, pp. 1817–1819, 1998.
- [27] A. K. Sarychev, D. J. Bergman, and Y. Yagil, "Theory of the optical and microwave properties of metal-dielectric films," *Physical Review B*, vol. 51, no. 8, pp. 5366–5385, 1995.
- [28] G. Mie, "Beiträge zur Optik trüber Medien, speziell kolloidaler Metallösungen," *Annalen der Physik*, vol. 330, pp. 377–445, 1908.
- [29] R. Gans, "Über die Form ultramikroskopischer Silberteilchen," *Annalen der Physik*, vol. 352, no. 10, pp. 270–284, 1915.
- [30] S. Link and M. A. El-Sayed, "Spectral properties and relaxation dynamics of surface plasmon electronic oscillations in gold and silver nanodots and nanorods," *Journal of Physical Chemistry B*, vol. 103, no. 40, pp. 8410–8426, 1999.
- [31] G. Fussell, J. Thomas, J. Scanlon, A. Lowman, and M. Marcolongo, "The effect of protein-free versus protein-containing medium on the mechanical properties and uptake of ions of PVA/PVP hydrogels," *Journal of Biomaterials Science*, vol. 16, no. 4, pp. 489–503, 2005.
- [32] T. Tsuji, T. Mizuki, S. Ozono, and M. Tsuji, "Laser-induced silver nanocrystal formation in polyvinylpyrrolidone solutions," *Journal of Photochemistry and Photobiology A*, vol. 206, no. 2–3, pp. 134–139, 2009.
- [33] J.-P. Sylvestre, S. Poulin, A. V. Kabashin, E. Sacher, M. Meunier, and J. H. T. Luong, "Surface chemistry of gold nanoparticles produced by laser ablation in aqueous media," *Journal of Physical Chemistry B*, vol. 108, no. 43, pp. 16864–16869, 2004.
- [34] A. Gautam and S. Ram, "Preparation and thermomechanical properties of Ag-PVA nanocomposite films," *Materials Chemistry and Physics*, vol. 119, no. 1–2, pp. 266–271, 2010.
- [35] I. Saini, J. Rozra, N. Chandak, S. Aggarwal, P. K. Sharma, and A. Sharma, "Tailoring of electrical, optical and structural properties of PVA by addition of Ag nanoparticles," *Mater. Chem. Phys.*, vol. 139, pp. 802–810, 2013.
- [36] S. Mahendia, A. K. Tomar, and S. Kumar, "Nano-Ag doping induced changes in optical and electrical behaviour of PVA films," *Materials Science and Engineering B*, vol. 176, no. 7, pp. 530–534, 2011.
- [37] M. Abdelaziz and E. M. Abdelrazek, "Effect of dopant mixture on structural, optical and electron spin resonance properties of polyvinyl alcohol," *Physica B*, vol. 390, no. 1–2, pp. 1–9, 2007.
- [38] B. Suo, X. Su, J. Wu, D. Chen, A. Wang, and Z. Guo, "Poly (vinyl alcohol) thin film filled with CdSe-ZnS quantum dots: fabrication, characterization and optical properties," *Materials Chemistry and Physics*, vol. 119, no. 1–2, pp. 237–242, 2010.
- [39] B. Karthikeyan, "Spectroscopic studies on Ag-polyvinyl alcohol nanocomposite films," *Physica B*, vol. 364, no. 1–4, pp. 328–332, 2005.
- [40] A. S. Kutsenko and V. M. Granchak, "Photochemical synthesis of silver nanoparticles in polyvinyl alcohol matrices," *Theoretical and Experimental Chemistry*, vol. 45, no. 5, pp. 313–318, 2009.
- [41] C. U. Devi, A. K. Sharma, and V. V. R. N. Rao, "Electrical and optical properties of pure and silver nitrate-doped polyvinyl alcohol films," *Materials Letters*, vol. 56, no. 3, pp. 167–174, 2002.
- [42] B. G. Streetman, *Solid State Electronic Devices*, Prentice Hall, New Jersey, NJ, USA, 3rd edition, 1990.
- [43] J. Tauc and R. Grigorovici, "Optical properties and electronic structure of amorphous germanium," *Physica Status Solidi (B)*, vol. 15, no. 2, pp. 627–637, 1966.
- [44] J. Rozra, I. Saini, A. Sharma et al., "Cu nanoparticles induced structural, optical and electrical modification in PVA," *Materials Chemistry and Physics*, vol. 134, no. 2–3, pp. 1121–1126, 2012.
- [45] M. Abdelaziz, "Cerium (III) doping effects on optical and thermal properties of PVA films," *Physica B*, vol. 406, no. 6–7, pp. 1300–1307, 2011.
- [46] C. Kittel, *Introduction to Solid State Physics*, vol. 405, John Wiley & Sons, New York, NY, USA, 1971.
- [47] J. D. Jackson, *Classical Electrodynamics*, John Wiley & Sons, 3rd edition, 1999.
- [48] M. S. Dresselhaus, *Solid State Physics Part II Optical Properties of Solids*, vol. 6, 2001.
- [49] J. N. Hodgson, *Optical Absorption and Dispersion in Solids*, Chapman & Hall, London, UK, 1971.
- [50] Y. Caglar, S. Ilican, and M. Caglar, "Single-oscillator model and determination of optical constants of spray pyrolyzed amorphous SnO₂ thin films," *European Physical Journal B*, vol. 58, no. 3, pp. 251–256, 2007.
- [51] Y. Seok Kim, *Electrical Conductivity of Segregated Network Polymer Nanoposites*, vol. 137, 2007.
- [52] Y. Feldman, A. Puzenko, and Y. Ryabov, "Dielectric relaxation phenomena in complex materials," in *Advances in Chemical Physics*, vol. 133, pp. 1–125, Department of Applied Physics, The Hebrew University of Jerusalem, Jerusalem, Israel, 2006.
- [53] S. Mahendia, A. K. Tomar, R. P. Chahal, P. Goyal, and S. Kumar, "Optical and structural properties of poly(vinyl alcohol) films embedded with citrate-stabilized gold nanoparticles," *Journal of Physics D*, vol. 44, no. 20, Article ID 205105, 2011.
- [54] S. H. Wemple and M. DiDomenico, "Behavior of the electronic dielectric constant in covalent and ionic materials," *Physical Review B*, vol. 3, no. 4, pp. 1338–1351, 1971.

Research Article

Preparation and Oxygen Permeability of $\text{BaCo}_{0.7}\text{Fe}_{0.2}\text{Nb}_{0.1}\text{O}_{3-\delta}$ Membrane Modified by $\text{Ce}_{0.8}\text{Y}_{0.2}\text{O}_{2-\delta}$ Porous Layer on the Air Side

Yuan Qiang,¹ Zhen Qiang,^{1,2} and Li Rong²

¹ School of Materials Science and Engineering, Shanghai University, Shanghai 200072, China

² Nano Science and Technology Research Center, Shanghai University, Shanghai 200444, China

Correspondence should be addressed to Zhen Qiang; qzhen@staff.shu.edu.cn

Received 31 August 2013; Accepted 10 October 2013

Academic Editor: Amirkianoosh Kiani

Copyright © 2013 Yuan Qiang et al. This is an open access article distributed under the Creative Commons Attribution License, which permits unrestricted use, distribution, and reproduction in any medium, provided the original work is properly cited.

$\text{BaCo}_{0.7}\text{Fe}_{0.2}\text{Nb}_{0.1}\text{O}_{3-\delta}$ (BCFN) dense ceramic membrane with submicron- $\text{Ce}_{0.8}\text{Y}_{0.2}\text{O}_{2-\delta}$ (YDC) porous layer was investigated by the partial oxidation of coke oven gas (COG) in hydrogen production. XRD analysis showed this composite had good stability and no chemical reaction at high temperature. SEM and TEM characterization further showed BCFN membrane was uniformly modified by YDC porous layer (about 5~6 μm thickness) formed by the accumulation of relative nanoparticles. At the respective COG flux and air flux of 108 mL/min and 173 mL/min, the oxygen permeation flux of BCFN modified by submicron-YDC porous layer reached 16.62 $\text{mL}\cdot\text{min}^{-1}\cdot\text{cm}^{-2}$, which was about 23.5% higher than that of pure BCFN membrane. Therefore, submicron-YDC porous layer obviously improved the oxygen permeation flux of BCFN membrane and its stability at 875°C.

1. Introduction

Partial oxidation of methane (POM) reforming technology is considered as one of the most economic and logical methods to produce syngas. Through further transforming and separating the formed syngas, then hydrogen can be further obtained. Coke oven gas (COG), a by-product which was generated in the process of producing coke from coal at the high temperature of 800°C, contains 30–40% CH_4 and is one of the most promising sources for hydrogen production [1]. Meanwhile, dense ceramic oxygen permeable membranes are widely used to separate oxygen from air at elevated temperatures with infinite permeation selectivity. These membranes are usually made from mixed oxygen ionic and electronic conductor (MIEC) and derived from perovskite-type (ABO_3) materials since ABO_3 materials display oxygen semipermeability due to their MIEC. Considering the two distinct processes which influence the rate of oxygen transport (bulk vacancy diffusion and surface exchange kinetics [2]), $\text{BaCo}_{0.7}\text{Fe}_{0.2}\text{Nb}_{0.1}\text{O}_{3-\delta}$ (BCFN) membranes [3–5] show excellent oxygen permeability among the

large variety of structural ABO_3 materials [6–14]. The rate of oxygen transport through the membrane is regulated by two distinct processes, bulk vacancy diffusion and surface exchange kinetics [2]. Furthermore, it also pushes the oxygen permeation rate limiting step near the side of the surface kinetics by reducing the thickness of membranes.

In order to improve the surface kinetics of oxygen transport, surface modification of the membrane with a higher surface exchange rate layer is a feasible way. This method increases the rate of surface kinetic reactions, which is beneficial for higher oxygen permeation rates under surface exchange or mixed controlled situations [4]. Recently, some researchers have played their great effort on surface modification of the membrane [15–17]. Although it is very important to modify the membrane on the reductive side, the surface modification on the air side is rarely reported. Ceria electrolytes exhibit superior ionic conductivity at lower temperature ranges (773–973 K) [18–21]. The high specific surface area and high ionic conductivity of submicron- $\text{Ce}_{0.8}\text{Y}_{0.2}\text{O}_{2-\delta}$ may obviously improve the surface kinetic reactions and oxygen permeability.

In this paper, BCFN membranes were modified by sub-micron-Ce_{0.8}Y_{0.2}O_{2-δ} (YDC) porous layer on the air side. XRD, SEM, and TEM were used to characterize the BCFN membranes with and without YDC modification. The influences of YDC modification on the surface kinetics and oxygen permeation rates of BCFN membranes were also systematically analyzed.

2. Experimental

2.1. Preparation of BCFN Powders, YDC Nanopowders, and BCFN-YDC Ceramics. BCFN powders were prepared by solid-state reaction method as described in [19]. BCFN membranes ($\Phi = 20$ mm, $d = 1.5$ mm) were prepared by uniaxial pressing BCFN powders at 200–250 MPa and then dried at 110°C for 24 h. The green bodies were further sintered at 1110°C for 8 h in air (a heating rate of 5°C/min) to obtain dense membrane. The membranes were polished to 1 mm thick before they were used.

YDC nanopowders were synthesized by the reverse titration chemical coprecipitation method as described in [22–24]. Nano-YDC porous layer was coated on one side of BCFN membranes by using the dipping method [2, 25–27]. It was then treated at 1000°C for 2 h. The BCFN membrane with thin submicron-YDC porous layer was marked as BCFN-YDC.

2.2. Characterization. Phases of BCFN powders, YDC nanopowders, and BCFN-YDC membrane were characterized by X-ray diffraction (*D*/max-2550 X-ray diffractometer, Rigaku, Japan) using CuK α radiation ($\lambda = 0.154178$ nm). A continuous scan mode was applied to collect data in $10^\circ \leq 2\theta \leq 90^\circ$ with a 0.02° step size and a $4^\circ/\text{min}$ scanning rate. The crystalline size of YDC nanopowders was calculated by the Scherrer equation $D = 0.89\lambda/(B \cdot \cos\theta)$, where B is the full width at half maximum of Bragg peaks.

Micrograph of YDC nanopowders was observed using transmission electron microscopy (TEM, 200CX transmission electronic microscope, Japan). Micrograph of BCFN membrane and BCFN-YDC membrane was observed by scanning electron microscopy (SEM, JSM-6700F high resolution scanning electronic microscope, Japan). The adhesion of BCFN membrane and YDC porous coating was tested by ultrasound machine (B3500S-DTH, 140 W, 42 kHz).

2.3. Oxygen Permeation Measurements. The diagram of membrane reactor is given in Figure 1. BCFN membrane with 17 mm diameter and 1.0 mm thickness was placed in the quartz tube. A silver ring was used as a gastight seal. The effective area of oxygen permeation was 1.3 cm^2 . COG (31.800% CH₄, 57.705% H₂, 7.366% CO, and 3.069% CO₂) and the air passed through the thin quartz tubes. These gases were placed at the location of 2 mm above or below the membrane in order to sweep the upper and lower surfaces of membrane, respectively. The gas flow rates were controlled by mass flow controllers.

Prior to the testing, gas tightness of membrane reactor was examined by detecting nitrogen in the outlet gas. A total of 1.0 g of 20–40 mesh Mg_{0.7}Co_{0.3}O catalyst was directly

placed on the upper surface. A K thermoelement measured the center temperature in the membrane reactor. On the permeation side of the membrane, the water was removed by Mg (ClO₄)₂, and H₂, CO, CO₂ and CH₄ in the outlet gas were analyzed by a Varian CP3800 gas chromatography (GC) with a thermal conductivity detector (TCD). According to the law of mass conservation, the oxygen permeation flux could be obtained as follows [15]:

$$F_{\text{O}_2, \text{inlet}} = \frac{1}{2}F_{\text{CO}, \text{outlet}} + F_{\text{CO}_2, \text{outlet}} + F_{\text{CH}_4, \text{inlet}} - F_{\text{CH}_4, \text{outlet}} - \frac{1}{2}(F_{\text{H}_2, \text{outlet}} - F_{\text{H}_2, \text{inlet}}) - \frac{1}{2}F_{\text{CO}, \text{inlet}} - F_{\text{CO}_2, \text{inlet}}, \quad (1)$$

where $F_{i, \text{inlet}}$ and $F_{i, \text{outlet}}$ are the flow rate (mL·min⁻¹) of the inlet and outlet gas *i*, respectively. $F_{\text{O}_2, \text{inlet}}$ is to be divided by the effective area of oxygen permeable membrane to obtain the actual oxygen permeation flux, J_{O_2} , mL·min⁻¹·cm⁻².

3. Results and Discussion

Figure 2 shows the XRD patterns of YDC nanopowders and BCFN powders. A single phase of cubic fluoride structure is obtained for YDC nanopowders in Figure 2(a). The pattern is indexed perfectly as Ce_{0.8}Y_{0.2}O_{2-δ} (JCPDS no. 75-0175). No other phase can be found which indicates that Y₂O₃ was homogeneously incorporated in the perovskite structure. Through the calculation of Scherrer's equation, the average crystallite size of YDC nanopowders is about 15 nm. In addition, a single perovskite structure of BCFN membrane can be also discovered according to the previous study [28] in Figure 2(b).

Since the oxygen membranes are used in high temperature environment, it is particularly important to study their high temperature stability. The BCFN ceramics modified by YDC layer showed the cubic fluoride structure and cubic perovskite structure (Figure 3(a)). However, the relative ceramics, which were prepared by simply mixing BCFN and YDC powders via ball-milling treatment and sintering at 1000°C for 5 h, displayed two obvious phases (Figure 3(b)). It means that the cubic fluoride structure and cubic perovskite structure are solely separated. The peaks of Figure 3(a) are lower than those of Figure 3(b) due to the YDC porous layer on the BCFN surface.

Obviously, the smaller nanoparticles can improve the oxygen permeability as they could enhance the effective specific surface area in YDC porous layer. Therefore, the microscopic structures of YDC nanopowders are characterized by TEM. Figure 4(a) illustrates that the YDC powders were well dispersed, and the particle size was around 10–25 nm. Additionally, it can be also found that the surfaces of BCFN ceramics are incredibly dense and composed of big particles with the crystal size of 5–20 μm (Figure 4(b)).

Regarding the coating materials, the adhesion between membrane and coated layers is very important for POM application. So the adhesion of BCFN membrane and YDC porous layer is studied by the ultrasonic vibration. Through analyzing the weight balance after calcination at different

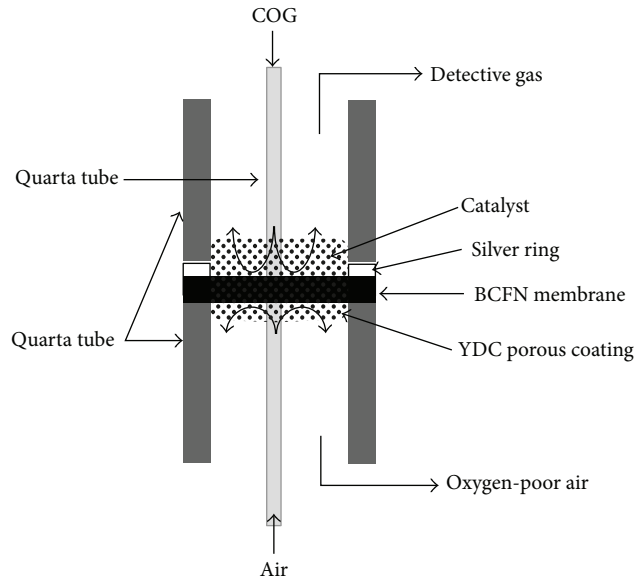


FIGURE 1: Schematic configuration of the membrane reactor at COG atmosphere.

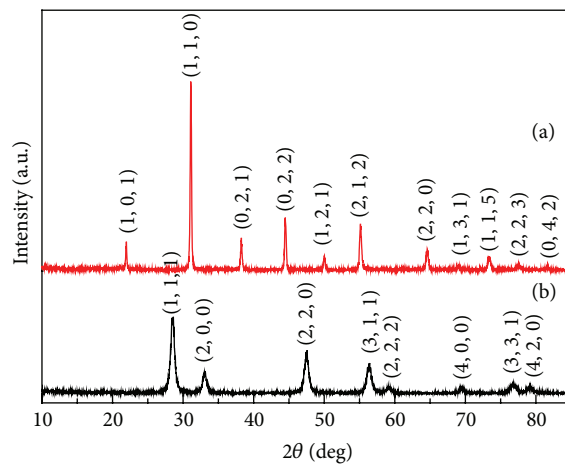


FIGURE 2: XRD patterns of (a) YDC nanopowders and (b) BCFN powders.

temperatures before and after ultrasonic treatments, the change trend of coating can be observed. It gradually reduced with the increment of calcination temperatures and altered smoothly above 950°C (Figure 5). The highest calcination temperature of BCFN-YDC is 1000°C in this paper.

The surface and cross section of BCFN-YDC samples are observed by SEM (Figure 6). The YDC layer exhibits a porous structure (Figures 6(a)–6(c)). These pores are accumulated by $100\sim 200\text{ nm}$ YDC nanoparticle and should be caused by the volatilization of organic solution in the slurry. The boundary between BCFN dense membrane and YDC porous layer could be easily distinguished (Figure 6(d)). But the YDC porous layer was well adhered to the BCFN membrane and its thickness was around $5\sim 6\ \mu\text{m}$.

Figure 7 showed the oxygen permeation flux of the BCFN membranes with and without YDC porous layer when COG flow rate changed at 875°C . It can be seen that the oxygen

permeation flux increases with rising COG flow rate, which can be attributed to the decrease of oxygen partial pressure on the permeation side. Moreover, BCFN-YDC exhibited higher oxygen permeation flux than uncoated BCFN membrane. When the air flow and COG flow were 173 mL/min and 108 mL/min , respectively, the oxygen permeation flux of BCFN-YDC was achieved at $16.62\text{ mL}\cdot\text{min}^{-1}\cdot\text{cm}^{-2}$, and it was about 23.5% higher than pure BCFN.

4. Conclusions

BCFN membrane modified by YDC porous on the air side formed a novel structure. A pure phase perovskite of BCFN membrane and a pure phase fluorite of YDC porous layer were obtained by dipping method. This novel structure exhibits higher stability and no chemical reaction at high temperature environment. In contrast to uncoated BCFN, it

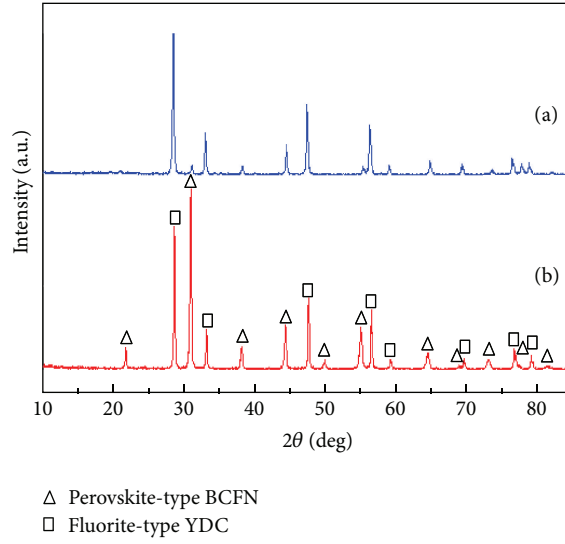


FIGURE 3: XRD patterns of (a) BCFN-YDC membrane and (b) the ceramics prepared by mixing BCFN and YDC powders.

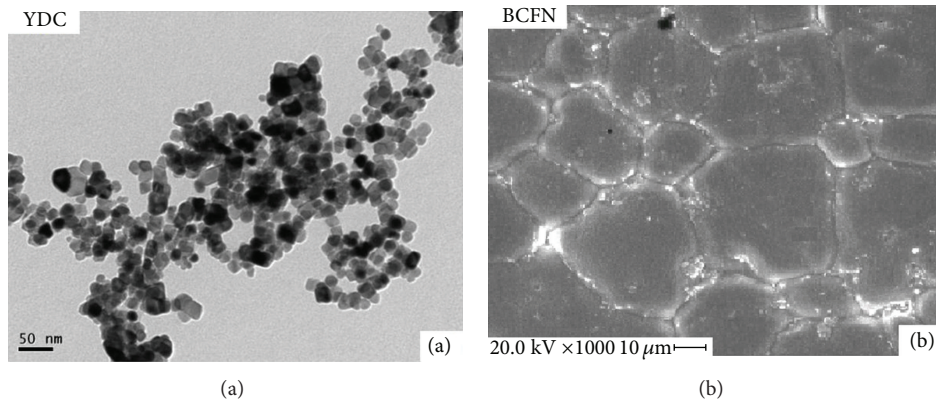


FIGURE 4: Images of (a) YDC nanopowders and (b) BCFN membrane.

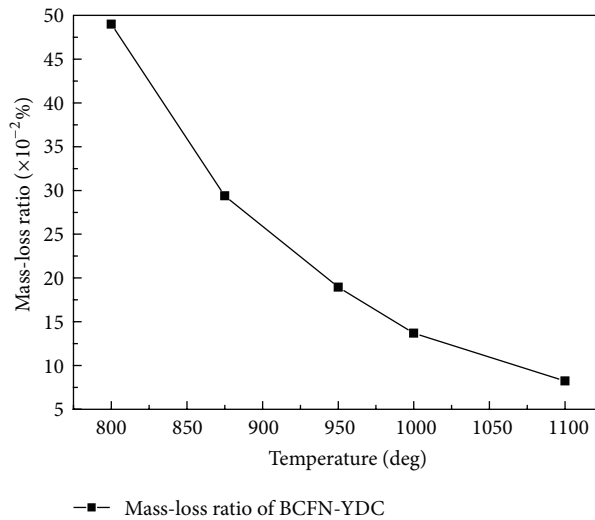


FIGURE 5: The change trend of YDC porous coating after calcination at different temperatures after ultrasonic treatments.

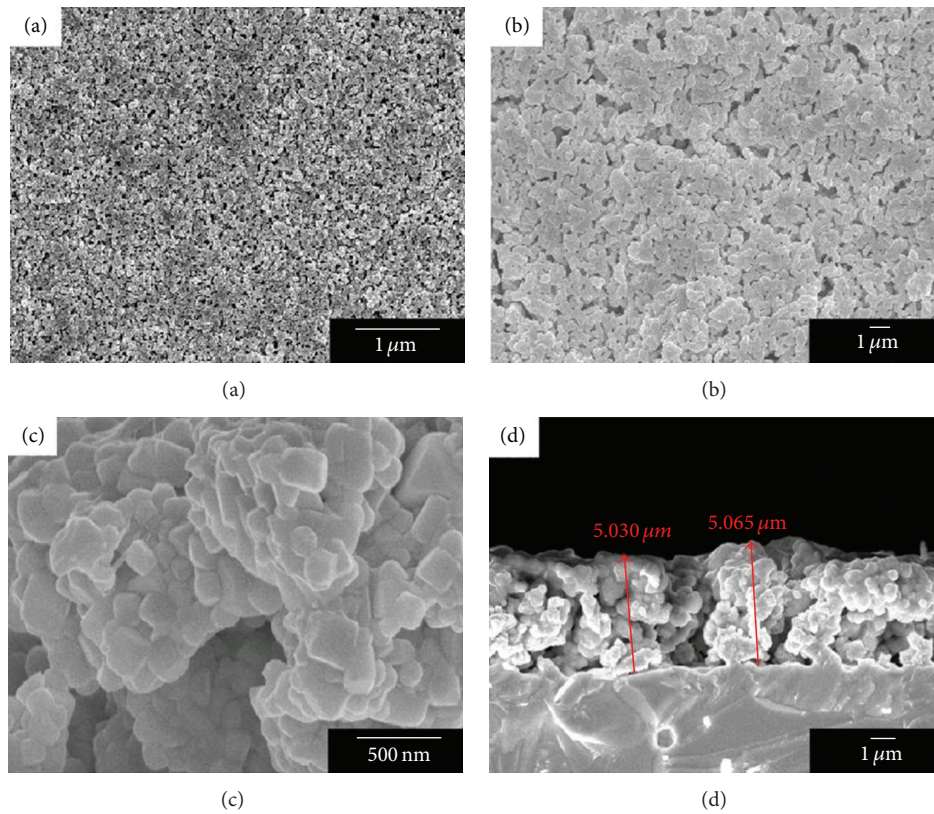


FIGURE 6: SEM images of ((a)–(c)) YDC porous layer at different magnification and (d) the cross-section of BCFN-YDC.

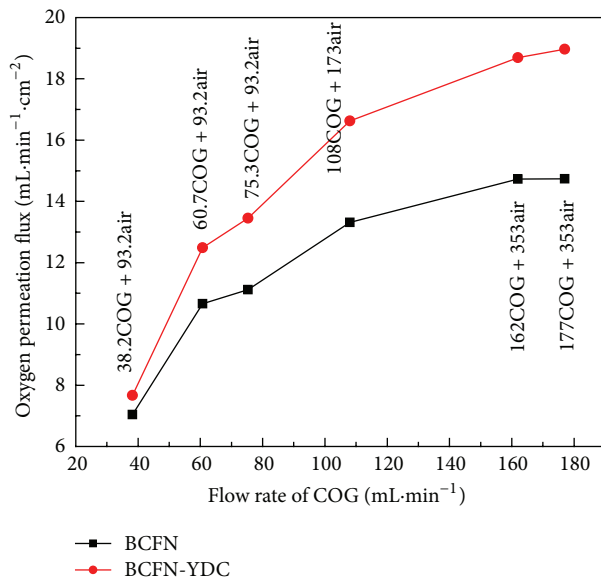


FIGURE 7: Oxygen permeation of BCFN and BCFN-YDC with COG changing at 875°C.

also obviously enhanced the oxygen permeation flux for COG application (23.5%). Our method may provide a new way for further improving oxygen permeation flux of COG.

Acknowledgment

The financial supports received from the National Natural Science Foundation of People's Republic of China (no. 51072112) are greatly appreciated.

References

- [1] J. Shen, Z.-Z. Wang, H.-W. Yang, and R.-S. Yao, "A new technology for producing hydrogen and adjustable ratio syngas from coke oven gas," *Energy and Fuels*, vol. 21, no. 6, pp. 3588–3592, 2007.
- [2] H. J. M. Bouwmeester, H. Kruidhof, and A. J. Burggraaf, "Importance of the surface exchange kinetics as rate limiting step in oxygen permeation through mixed-conducting oxides," *Solid State Ionics*, vol. 72, no. 2, pp. 185–194, 1994.
- [3] M. Harada, K. Domen, M. Hara, and T. Tatsumi, "Ba_{1.0}Co_{0.7}Fe_{0.2}Nb_{0.1}O_{3-δ} dense ceramic as an oxygen permeable membrane for partial oxidation of methane to synthesis gas," *Chemistry Letters*, vol. 35, no. 12, pp. 1326–1327, 2006.
- [4] Y. Cheng, H. Zhao, D. Teng, F. Li, X. Lu, and W. Ding, "Investigation of Ba fully occupied A-site BaCo_{0.7}Fe_{0.3-x}Nb_xO_{3-δ} perovskite stabilized by low concentration of Nb for oxygen permeation membrane," *Journal of Membrane Science*, vol. 322, no. 2, pp. 484–490, 2008.
- [5] H. Cheng, X. Lu, Y. Zhang, and W. Ding, "Hydrogen production by reforming of simulated hot coke oven gas over nickel

- catalysts promoted with lanthanum and cerium in a membrane reactor," *Energy and Fuels*, vol. 23, no. 6, pp. 3119–3125, 2009.
- [6] Y. S. Lin, "Microporous and dense inorganic membranes: current status and prospective," *Separation and Purification Technology*, vol. 25, no. 1–3, pp. 39–55, 2001.
- [7] R. W. Baker, "Future directions of membrane gas separation technology," *Industrial and Engineering Chemistry Research*, vol. 41, no. 6, pp. 1393–1411, 2002.
- [8] J. Sunarso, S. Baumann, J. M. Serra et al., "Mixed ionic-electronic conducting (MIEC) ceramic-based membranes for oxygen separation," *Journal of Membrane Science*, vol. 320, no. 1–2, pp. 13–41, 2008.
- [9] J. W. Stevenson, T. R. Armstrong, R. D. Carneim, L. R. Pederson, and W. J. Weber, "Electrochemical properties of mixed conducting perovskites $\text{La}_{1-x}\text{M}_x\text{Co}_{1-y}\text{Fe}_y\text{O}_{3-\delta}$ ($\text{M} = \text{Sr}, \text{Ba}, \text{Ca}$)," *Journal of the Electrochemical Society*, vol. 143, no. 9, pp. 2722–2729, 1996.
- [10] T. Ishihara, T. Yamada, H. Arikawa, H. Nishiguchi, and Y. Takita, "Mixed electronic-oxide ionic conductivity and oxygen permeating property of Fe-, Co- or Ni-doped LaGaO_3 perovskite oxide," *Solid State Ionics*, vol. 135, no. 1–4, pp. 631–636, 2000.
- [11] Z. P. Shao, G. X. Xiong, J. H. Tong et al., "Ba effect in doped $\text{Sr}(\text{Co}_{0.8}\text{Fe}_{0.2})\text{O}_{3-\delta}$ on the phase structure and oxygen permeation properties of the dense ceramic membranes," *Separation and Purification Technology*, vol. 25, no. 1–3, pp. 419–429, 2001.
- [12] H. Wang, Y. Cong, and W. Yang, "Investigation on the partial oxidation of methane to syngas in a tubular $\text{Ba}_{0.5}\text{Sr}_{0.5}\text{Co}_{0.8}\text{Fe}_{0.2}\text{O}_{3-\delta}$ membrane reactor," *Catalysis Today*, vol. 82, no. 1–4, pp. 157–166, 2003.
- [13] S. Liu and G. R. Gavalas, "Oxygen selective ceramic hollow fiber membranes," *Journal of Membrane Science*, vol. 246, no. 1, pp. 103–108, 2005.
- [14] W. Jin, S. Li, P. Huang, N. Xu, and J. Shi, "Preparation of an asymmetric perovskite-type membrane and its oxygen permeability," *Journal of Membrane Science*, vol. 185, no. 2, pp. 237–243, 2001.
- [15] S. M. Murphy, D. A. Slade, K. J. Nordheden, and S. M. Stagg-Williams, "Increasing oxygen flux through a dense oxygen permeable membrane by photolithographic patterning of platinum," *Journal of Membrane Science*, vol. 277, no. 1–2, pp. 94–98, 2006.
- [16] A. Thursfield and I. S. Metcalfe, "Air separation using a catalytically modified mixed conducting ceramic hollow fibre membrane module," *Journal of Membrane Science*, vol. 288, no. 1–2, pp. 175–187, 2007.
- [17] A. Leo, S. Liu, J. C. Diniz da Costa, and Z. Shao, "Oxygen permeation through perovskite membranes and the improvement of oxygen flux by surface modification," *Science and Technology of Advanced Materials*, vol. 7, no. 8, pp. 819–825, 2006.
- [18] S. Li, L. Ge, H. Gu, Y. Zheng, H. Chen, and L. Guo, "Sinterability and electrical properties of ZnO-doped $\text{Ce}_{0.8}\text{Y}_{0.2}\text{O}_{1.9}$ electrolytes prepared by an EDTA-citrate complexing method," *Journal of Alloys and Compounds*, vol. 509, no. 1, pp. 94–98, 2011.
- [19] Q. Zhen, Q. Yuan, H. Wang, C. Ding, W. Ding, and X. Lu, "Investigation of chemical stability and oxygen permeability of perovskite-type $\text{Ba}_{0.5}\text{Sr}_{0.5}\text{Co}_{0.8}\text{Fe}_{0.2}\text{O}_{3-\delta}$ and $\text{BaCo}_{0.7}\text{Fe}_{0.2}\text{Nb}_{0.1}\text{O}_{3-\delta}$ ceramic membranes," *Solid State Ionics*, vol. 198, no. 6, pp. 50–55, 2011.
- [20] B. C. H. Steele, "Appraisal of $\text{Ce}_{1-y}\text{Gd}_y\text{O}_{2-y/2}$ electrolytes for IT-SOFC operation at 500°C," *Solid State Ionics*, vol. 129, no. 1, pp. 95–110, 2000.
- [21] M. Mogensen, N. M. Sammes, and G. A. Tompsett, "Physical, chemical and electrochemical properties of pure and doped ceria," *Solid State Ionics*, vol. 129, no. 1, pp. 63–94, 2000.
- [22] Q. Yuan, Q. Zhen, R. Li, L. Gao, and L. Ni, "Reaction mechanism of preparing $\text{Bi}_{0.75}\text{Dy}_{0.25}\text{O}_{1.5}$ nanopowder by the reverse titration chemical coprecipitation method," *Journal of University of Science and Technology Beijing*, vol. 32, no. 2, pp. 245–249, 2010.
- [23] Q. Zhen, G. M. Kale, G. Shi et al., "Processing of dense nanocrystalline $\text{Bi}_2\text{O}_3\text{-Y}_2\text{O}_3$ solid electrolyte," *Solid State Ionics*, vol. 176, no. 30, pp. 2727–2733, 2005.
- [24] Q. Zhen, R. N. Vannier, and G. M. Kale, "Preparation of dense nanocrystalline $\text{Bi}_2\text{O}_3\text{-HfO}_2\text{-Y}_2\text{O}_3$ ceramic by microwave plasma sintering," *Materials Science and Engineering A*, vol. 444, no. 1–2, pp. 130–137, 2007.
- [25] N. N. Dinh, N. T. T. Oanh, P. D. Long et al., "Electrochromic properties of TiO_2 anatase thin films prepared by a dipping sol-gel method," *Thin Solid Films*, vol. 423, no. 1, pp. 70–76, 2003.
- [26] E. Barrera, T. Viveros, A. Avila et al., "Cobalt oxide films grown by a dipping sol-gel process," *Thin Solid Films*, vol. 346, no. 1–2, pp. 138–144, 1999.
- [27] H. Hayashi, H. Inaba, M. Matsuyama, N. G. Lan, M. Dokiya, and H. Tagawa, "Structural consideration on the ionic conductivity of perovskite-type oxides," *Solid State Ionics*, vol. 122, no. 1–4, pp. 1–15, 1999.
- [28] Y. Eraoka, M. Yoshimatsu, N. Yamazoe, and T. Seiyama, "Oxygen-sorptive properties and defect structure of perovskite-type oxides," *Chemistry Letters*, vol. 6, pp. 893–896, 1984.